



Title	Role of Lattice Distortion in Multi-Band Ferromagnets
Author(s)	Kawamoto, Tohru
Citation	
Issue Date	
Text Version	ETD
URL	http://hdl.handle.net/11094/429
DOI	
Rights	

Osaka University Knowledge Archive : OUKA

<http://ir.library.osaka-u.ac.jp/dspace/>

Role of Lattice Distortion
in Multi-Band Ferromagnets

Tohru KAWAMOTO

OSAKA UNIVERSITY
GRADUATE SCHOOL OF ENGINEERING SCIENCE
DEPARTMENT OF MATERIAL PHYSICS
TOYONAKA OSAKA

①

Thesis

**Role of Lattice Distortion
in Multi-Band Ferromagnets**

Tohru KAWAMOTO

OSAKA UNIVERSITY
Graduate School of Engineering Science
Department of Material Physics
Toyonaka Osaka

January 1997

Abstract

The role of lattice distortion in two kinds of multi-band ferromagnets is studied in detail. One is TDAE-C₆₀ and the other is the layered perovskite-type orbital ordering compound K₂CuF₄.

We propose that the origin of ferromagnetism of TDAE-C₆₀ is the orbital ordering due to combined effects of intramolecular charge transfer induced Jahn-Teller (CTJT) distortion and intermolecular cooperative Jahn-Teller (CJT) distortion. First, semi-empirical MO calculation and structure optimization are carried out for a single C₆₀⁻ ion and it is found that C₆₀⁻ is distorted from spherical shape into rugby ball-like structure, namely CTJT is realized actually. Next we found that C₆₀⁻ crystals can order ferromagnetically if distorted C₆₀⁻ anions are arranged so that appropriate orbital ordering is realized, which is called CJT distortion. In order to examine the actual possibility of the ferromagnetic order the magnetic phase diagram for one-dimensional multi-band Hubbard model relevant to a C₆₀⁻ chain is constructed with exact diagonalization procedure. It is found that the high spin state (ferromagnetic state) can be certainly the ground state for the parameters derived by semi-empirical MO calculation and CI interaction calculation for C₆₀⁻. We propose possible three-dimensional arrangements of distorted C₆₀⁻ ions which can give rise to three-dimensional ferromagnetic order. We also propose several experimental approaches which might be able to confirm our suggestion.

We have studied also the pressure effects on Perovskite-type orbital ordering ferromagnet K₂CuF₄, particularly the pressure-induced transition from ferromagnetic (F) to antiferromagnetic (AF) state. First the magnetic phase diagram of simple one-dimensional multi-band Hubbard Hamiltonian with antiferrodistortive order is constructed with exact diagonalization procedure. It is found that AF and helical (HI) states can be stable in a region of large transfer energy even with keeping antiferrodistortive order. For more realistic two-dimensional models relevant to CuF₂ plane in K₂CuF₄ the magnetic phase diagram is derived by perturbational procedure. Judging from the parameter values estimated by FLAPW band calculations for K₂CuF₄ under high pressure as well as at am-

bient pressure, it is concluded that the pressure-induced F-AF transition may be realized in K_2CuF_4 without structural transition from antiferrodistortive to ferrodistortive phase. Further the observed pressure dependence of T_c of K_2CuF_4 can be explained qualitatively by our theory.

Ackowlegements

The author would like to express his sincere gratitude to Prof. N. Suzuki, under whose guidance this work have been done, for valuable suggestions, enlightening discussions through the course of the work and critical reading of this thesis. He thanks Dr. M. Shirai for lending his insight about the physics to the author.

Thanks are also due to Dr. M. Ishizuka giving his unpublished experimental data of the properties of K_2CuF_4 . He also thanks gratefully Professor A. Yanase and Dr. H. Harima for providing him with their FORTRAN source codes for FLAPW band calculation. And he would like to give his gratitude to H. Shimizu, Y. Tokioka, R. Kuroiwa and all the member of Suzuki lab. for providing him with the useful discussions.

This work is supported by Grant-in-Aid for JSPS Fellows from the Ministry of Education, Science, Sports and Culture, Japan. And a part of computation work in this thesis has been done using the facilities of the Supercomputer Center, Institute for Solid State Physics, University of Tokyo.

Contents

1	Introduction	6
2	Theoretical Methods	9
2.1	Semi-empirical Molecular Orbital Calculations	9
2.2	Exact Diagonalization of Hubbard Model	11
2.2.1	Multi-Band Hubbard Hamiltonian	11
2.2.2	Exact diagonalization procedure	12
2.2.3	Physical quantities of the ground state	14
2.3	FLAPW Band Calculations	15
2.3.1	LDA(Local Density Approximation)	15
2.3.2	FLAPW method	16
3	A Model of the Ferromagnetism of TDAE-C₆₀	19
3.1	Backgrounds	19
3.1.1	Main results of experiments	19
3.1.2	Basic properties of C ₆₀ molecule	21
3.1.3	Crystal structure of TDAE-C ₆₀ and its peculiarity	23
3.2	Role of Jahn-Teller Distortions	26
3.2.1	Charge transfer induced Jahn-Teller distortion	26
3.2.2	Role of CTJT interaction for inter-molecular magnetic interaction	30
3.2.3	Cooperative Jahn-Teller effect and the origin of ferromagnetism	31
3.3	Suggestion of Superstructures and Methods to Survey	34
3.4	Discussion	38
4	Pressure Effect in Magnetism of Orbital Ordering Ferromagnet	46
4.1	Experimental and Theoretical Backgrounds	46
4.1.1	Physical properties under ambient pressure	47

4.1.2	Properties under high pressure	50
4.1.3	Basic theoretical approach and its problem	52
4.2	Exact diagonalization approach for 1D model	53
4.3	Band calculations with FLAPW method	56
4.3.1	Crystal structure of K_2CuF_4	56
4.3.2	Results of FLAPW calculations	59
4.3.3	Estimation of transfer and orbital energies	67
4.4	Perturbational approach for CuX_2 plane	72
4.4.1	Construction of multi-band Hubbard model Hamiltonian	72
4.4.2	Transformation to Heisenberg Model	74
4.4.3	Phase diagram	79
4.5	Discussion	82
4.5.1	Physical view of pressure effect in our study	82
4.5.2	Problems	84
5	Summary	86

Chapter 1

Introduction

Recently many physicists and chemists have been studying about the so-called multi-band materials, in which existence of two or more orbitals on an atom or a molecule plays a essential role for various physical properties. Typical examples are organic ferromagnets. Since *p*-NPNN was discovered first as a purely organic ferromagnet in 1991 [1], various organic ferromagnets have been synthesized. Most of them are understood to be ferromagnetic if intermolecular transfers between many orbitals satisfy special relations. One of the most interesting and puzzled systems is TDAE-C₆₀ [2, 3, 4], which shows a ferromagnetic behavior with a Curie temperature $T_C=16$ K [5]. This transition temperature is quite high among the purely organic ferromagnets discovered thus far.

Another example of the multi-band materials is cubic perovskite-type compounds, La_{1-x}Sr_xMnO₃ and its family, which have been regarded as double exchange systems [6, 7, 8]. These systems have been revisited by both experimentalists and theoreticians, and it has been clarified that doubly degenerate $d\gamma$ orbital of Mn ions plays a crucial role in orbital, charge and spin ordering which govern the physical properties of these systems [9, 10]. The $d\gamma$ orbital plays an important role also in causing ferromagnetism of the layered perovskite-type compounds such as K₂CuF₄ and (RNH₃)₂CuCl₄(R=Alkil chain or aromatic group). Quite interestingly ferromagnetic (F) to antiferromagnetic (AF) transition has been observed in these systems under high pressure [11, 12].

The purpose of this thesis is first to propose a mechanism for the ferromagnetism of TDAE-C₆₀, and secondly to clarify the nature of pressure-induced F-AF transition of K₂CuF₄ and related materials.

In chapter 2 we outline the three calculational methods used in this thesis. They are (1) PM3 method for semi-empirical molecular orbital (MO) calculations and its configu-

ration interaction (CI) calculation, (2) exact diagonalization (ED) method for multi-band Hubbard Hamiltonians, and (3) FLAPW (full-potential linearized augmented-plane-wave) method for first-principles band calculations.

The mechanism of ferromagnetism of TDAE-C₆₀ is discussed in chapter 3. We suggest a possible origin of the intermolecular ferromagnetic interaction between C₆₀⁻'s. The charge-transfer induced intramolecular Jahn-Teller (CTJT) distortion of C₆₀⁻ is first studied by calculating the molecular orbitals with use of the PM3 method in MOPAC library, and then the relation between the orientation of two C₆₀⁻'s and their magnetic interaction is discussed. Furthermore, the role of intermolecular cooperative Jahn-Teller (CJT) distortion in ferromagnetic ordering is investigated with exact diagonalization procedure of finite-size multi-band Hubbard chains. And a possible JT-distorted crystal structure which is likely to exhibit three dimensional ferromagnetic ordering is proposed. Finally we also suggest several experimental approaches which may confirm the model proposed in this report.

In chapter 4 we investigate pressure effects on magnetism of the layered perovskite-type compounds such as K₂CuF₄ and (RNH₃)₂CuCl₄ (R=Alkil chain or aromatic group). K₂CuF₄ is a ferromagnet whose Curie temperature is 6.25K, and it is believed that its ferromagnetic origin is ascribed to cooperative Jahn-Teller effect due to degenerate $d\gamma$ -orbitals of Cu ions. In CuX₂ plane (X=Halogen), ferromagnetic state become stable due to antiferrodistortion. Recently Ishizuka *et al.* carried out magnetization measurements for K₂CuF₄ under high pressures up to 13 GPa over the temperature range from 1.5 to 18 K [11]. Their results show that the value of T_C is almost constant for pressures $P < 4$ GPa. They have reported also that the magnetic susceptibility at low temperatures is suppressed rapidly above $P_c = 8 \sim 9$ GPa, which indicates the disappearance of the ferromagnetic state. They speculated that at P_c a transition from the F to the AF state is induced by a structural transition from the AFD to the ferrodistortive (FD) ordering of F⁻ ions. On the other hand, from Raman scattering measurements Kitazawa *et al.* have observed that a structural phase transition occurs at a pressure higher than P_c [63]. This result may suggest that structural transition can not be the origin of disappearance of the ferromagnetic state.

As a first step to discuss magnetic properties of K₂CuF₄ and related materials we use one dimensional multi-band Hubbard model which takes account only $d\gamma$ -orbitals of Cu ions. Magnetic phase diagram in the space of some parameters are constructed with exact

diagonalization procedure. Next, perturbational approach is applied to two dimensional multi-band Hubbard model and the original model Hamiltonian is transformed into a Heisenberg Hamiltonian. Then, phase diagram in the space of exchange couplings in this Heisenberg Hamiltonian is produced with classical spin approximation, and it is projected into the space of parameters of the original multi-band Hubbard Hamiltonian. The transfer energies in the model Hamiltonian, which are relevant to K_2CuF_4 are estimated by using the results of FLAPW band calculations for K_2CuF_4 . On the basis of the obtained results we discuss the pressure-induced F-AF transition observed in K_2CuF_4 and related materials.

Chapter 2

Theoretical Methods

In this thesis theoretical investigations are done by using three methods: PM3 method for molecular orbital calculations, exact diagonalization method for multi-band Hubbard Hamiltonian, and FLAPW (full-potential linearized augmented-plane-wave) method for band calculations. In this chapter we outline the essence of these three theoretical methods.

2.1 Semi-empirical Molecular Orbital Calculations

HF approximation and MECI calculation

Most of molecular orbital (MO) calculations are based on the Hartree-Fock (HF) approximation. In chapter 3, in addition to MO calculations with the HF approximation, MECI (Multi-Electron Configuration Interaction) calculations are carried out also. In this section we outline these procedures briefly.

Atomic orbitals (AO) are considered as one-particle basis functions. Consequently MO's are derived as linear combinations of AO's, which is called LCAO(Linear Combination of Atomic Orbital) approximation:

$$\chi_n(\mathbf{r}) = \sum_i c_{ni} \phi_i(\mathbf{r}), \quad (2.1)$$

where ϕ_i represents an AO specified by the label i . We solve the variational problem with using Slater determinant consisting of χ_n 's as trial function with HF approximation. By this approximation, however, correlation effect is neglected. In order to improve this problem, MECI calculation has been developed. In the HF approximation, $N/2$ lower state of one-particle wave functions are occupied (2 represents degeneracy of spin). In

CI calculations, on the other hand, we consider the many-body states in which electrons are transferred from lower state to higher state. Many-body eigenstates are obtained by diagonalizing the Hamiltonian matrix in this space. It is a defect of CI calculation that it cannot be applied to large systems due to restriction of memory on computers. For larger system, we often apply MECI method with limited one-particle states. In this procedure, limited occupied states and unoccupied states are specified as active space. Electronic transfer in active space are only considered in producing many-body bases. For instance we consider a system with three orbitals and three electrons (see Fig. 2.1). We must take account of twenty states as many-body bases if we carry out full-CI calculations. If we have two higher orbitals included in active space, on the other hand, only four states which are shown in Fig. 2.1 may be considered as many-body bases. Generally speaking, orbitals near the Fermi energy mainly contribute to material properties, and consequently MECI calculations yield good results in many cases.

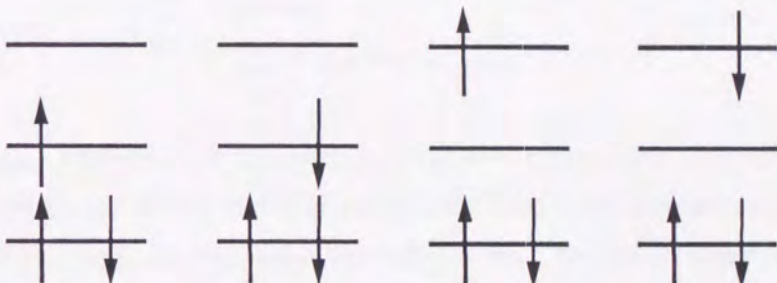


Figure 2.1: Many-body bases used in MECI calculation whose active space consist of upper two orbitals

PM3 method and MOPAC library

Major difficulty of MO calculations lies in integral calculi. Matrix elements of Hamiltonian is given as integral of the product of an operator and 2~4 AO's through the whole space, which give limitation to the system size to be calculated. In semi-empirical MO calculations, integral calculi are replaced with parameters estimated from experiments. PM3 method, which is used in chapter 3, is one of such semi-empirical MO calculation methods. The parameters used in the PM3 method are given in ref. [21]. Furthermore the

PM3 method is included in MOPAC, which is a package of semi-empirical MO calculations [22] distributed by QCPE or JCPE.

2.2 Exact Diagonalization of Hubbard Model

2.2.1 Multi-Band Hubbard Hamiltonian

Hubbard models have been studied by many scientists for discussing electronic states in crystals with strong electron correlation [23, 24, 25]. In chapters 3 and 4 we use multi-band Hubbard Hamiltonian [26, 27] to discuss the so-called orbital ordering ferromagnetism. Our model Hamiltonian is expressed as follows:

$$\begin{aligned} H = & \sum_{i\mu\sigma} V_\mu n_{i\mu\sigma} + \sum_{i\mu\nu\sigma} t_{\delta\mu\nu}(c_{i\mu\sigma}^\dagger c_{i+\delta\nu\sigma} + h.c.) \\ & + \sum_{i\mu} U n_{i\mu\uparrow} n_{i\mu\downarrow} \\ & + \sum_{i\mu \neq \nu \sigma \sigma'} (U - J\delta_{\sigma\sigma'}) n_{i\mu\sigma} n_{i\nu\sigma'} \\ & + \sum_{i\mu\nu\sigma} J c_{i\mu\sigma}^\dagger c_{i\nu\bar{\sigma}}^\dagger c_{i\mu\bar{\sigma}} c_{i\nu\sigma} \end{aligned} \quad (2.2)$$

where $c_{i\mu\sigma}^\dagger (c_{i\mu\sigma})$ represents a creation (annihilation) operator of μ -orbital with σ -spin at the i th site and $n_{i\mu\sigma}$ is the number operator. The first, the second, the third and the fourth lines represent, respectively, the orbital and the intermolecular transfer energies, the intra-orbital Coulomb energy, the inter-orbital Coulomb energy and the $S_z S_z$ part of exchange interaction, and the $S_+ S_-$ part of exchange interaction.

This Hamiltonian is derived with assumptions as follows:

- The intra-orbital and the inter-orbital Coulomb energies are assumed to be the same.
- Among non-diagonal part of Coulomb interaction, only exchange interaction is considered

Furthermore, assuming that the system is one-dimensional and that transfer interaction exist only between nearest neighbors, we can obtain

$$\begin{aligned} H = & \sum_{k\mu\sigma} V_\mu n_{k\mu\sigma} + \sum_{k\mu\nu\sigma} t_{k\mu\nu}(c_{k\mu\sigma}^\dagger c_{k\nu\sigma} + h.c.) \\ & + \sum_{kq\mu} U c_{k+q\mu\sigma}^\dagger c_{k\mu\sigma'}^\dagger c_{k+q\mu\sigma'} c_{k\mu\sigma} \end{aligned} \quad (2.3)$$

$$\begin{aligned}
& + \sum_{kq\mu \neq \nu\sigma\sigma'} (U - J\delta_{\sigma\sigma'}) c_{k+q\mu\sigma}^\dagger c_{k\nu\sigma'}^\dagger c_{k+q\nu\sigma'} c_{k\mu\sigma} \\
& + \sum_{kq\mu \neq \nu\sigma} J c_{k+q\mu\sigma}^\dagger c_{k\nu\sigma'}^\dagger c_{k+q\mu\sigma'} c_{k\nu\sigma}, \\
t_{k\mu\nu} & = 2l_{\mu\nu} \cos k.
\end{aligned} \tag{2.4}$$

with Fourier transformation:

$$c_{i\mu\sigma} = \frac{1}{\sqrt{N}} \sum_k c_{k\mu\sigma} e^{-ikR_i}, \tag{2.5}$$

$$c_{k\mu\sigma}^\dagger = \frac{1}{\sqrt{N}} \sum_i c_{k\mu\sigma}^\dagger e^{ikR_i}. \tag{2.6}$$

2.2.2 Exact diagonalization procedure

Hubbard models have been treated with various approximations since it is difficult to solve exactly the eigenvalue problem for Hubbard systems with infinite size [23, 24, 25, 26, 27]. Below we explain practical procedures of exact diagonalization method for one-dimensional finite systems.

Number of basis functions

The most difficult problem is rapid increase of the number of bases as extending the system size. For single-band Hubbard systems the number of bases is ${}_{2N}C_{N_e}$ if the number of sites, N , and the number of electrons, N_e , are the same. For example, for $N=N_e=14$, the number of bases is ${}_{28}C_{14}=4.0 \times 10^7$! It is more serious for multi-band Hubbard systems. The number of bases is ${}_{4N}C_{N_e}$ for two-orbitals system with quarter filling. Therefore, even for $N=N_e=8$ we need ${}_{32}C_8=1.0 \times 10^7$ bases. It is impossible practically to diagonalize such a large matrix. This situation is improved a little bit if we carry out block diagonalization of Hamiltonian matrices by making use of the symmetry properties or the conservative quantities whose operators are commutable with the Hamiltonian. Such operators commutable with the Hamiltonian are listed in Table 2.1.

Of course, all block diagonalization procedure cannot be carried out always at the same time, since these operators cannot be always commutable with each other. But we can reduce the dimension of matrices from order of 10^7 to 10^5 .

Table 2.1: Operators commutable with Hamiltonian and the number of blocks after block diagonalization

operator	meanings	Number of block
S_z^{total}	Total z components of spin	Num. of electron+1
T	Translation	Num. of Sites
I	Mirror in real space	2
Is	Mirror in spin space	2

One-electron bases

Site-localized bases are often used as one-electron bases. In this thesis, however, we use Bloch functions as the one-electron basis functions because Bloch functions are eigenfunctions of T . It has the advantage of disuse of block diagonalization for T , but has disadvantage in calculating off-diagonal elements of Hamiltonian. With using localized orbital as one-particle basis function, off-diagonal part is produced in calculating transfer part, which is one-particle operator. On the other hand, it is produced from two-particle operator in this procedure, which makes the scale of calculation bigger. We must select the shape of bases for each system.

Diagonalization of matrices

For practical diagonalization we must carry out the following three procedures: 1) triple diagonalization, 2) calculating eigenvalues, and 3) calculating eigenfunctions. For triple diagonalization we usually use Lanczos or Householder transformation. Lanczos transformation is useful for obtaining information of the minimum or the maximum eigenvalues of a large matrix, which is necessary to get information for the ground state. On the other hand, Householder transformation is favorable to get thermal expectation value because we can know all the eigenvalues and eigenvectors by this method. Eigenvalues can be obtained with the bisection method, which has advantages in computational speed and amount of memory. The eigenfunction of only the ground state is calculated with conjugate gradient method.

2.2.3 Physical quantities of the ground state

We have to calculate the physical quantities to clarify the ground state properties. The definition and meaning of the physical quantities we use in this thesis are as follows:

1. Total spin: $\langle S^{\text{tot}} \rangle$

From $\langle S^{\text{tot}} \rangle$ where $\langle \dots \rangle$ means the expectation value in the ground state we can get important information for magnetic properties. If $\langle S^{\text{tot}} \rangle \neq 0$, this system is in ferromagnetic or ferrimagnetic state. The definition of $\langle S^{\text{tot}} \rangle$ is given as follows:

$$\begin{aligned} (S^{\text{tot}})^2 &= (S_x^{\text{tot}})^2 + (S_y^{\text{tot}})^2 + (S_z^{\text{tot}})^2 \\ &= \frac{1}{2}(S_+^{\text{tot}}S_-^{\text{tot}} + S_-^{\text{tot}}S_+^{\text{tot}}) + (S_z^{\text{tot}})^2, \\ S_{\alpha}^{\text{tot}} &= \sum_{k\mu} s_{k\mu}^{\alpha}, \\ s_{k\mu}^{+} &= c_{k\mu\uparrow}^{\dagger}c_{k\mu\downarrow}, \\ s_{k\mu}^{-} &= c_{k\mu\downarrow}^{\dagger}c_{k\mu\uparrow}, \\ s_{k\mu}^{z} &= \sum_{\sigma} \sigma n_{k\mu\sigma}. \end{aligned} \quad (2.7)$$

However, we only calculate eigenvalues for each S_z^{tot} instead of calculating the expectation value of this operator because we can know it with counting the degeneracy of each state.

2. Particle density for each orbital: $\langle n_{\mu} \rangle$

$$\langle n_{\mu} \rangle = \frac{1}{2N} \sum_k \langle n_{k\mu} \rangle \quad (2.8)$$

Information for difference of orbital is brought out from this value.

3. Fluctuation of density: $\langle (\delta n_{\mu}) \rangle$

$$\langle (\delta n_{\mu}) \rangle = \frac{1}{2N} \left\langle \sum_i \left(\sum_{\sigma} n_{i\mu\sigma} - \sum_{\sigma} \langle n_{i\mu\sigma} \rangle \right)^2 \right\rangle \quad (2.9)$$

We can know from this whether electrons has localized character or itinerant character. It becomes 0 in localized limit. In itinerant limit, on the other hand, it becomes positive constant, which depends on the electron number and etc.

4. Spin-spin correlation function $\langle \mathbf{S}_{i\mu} \cdot \mathbf{S}_{i+\delta\nu} \rangle$

$$\langle \mathbf{S}_{i\mu} \cdot \mathbf{S}_{i+\delta\nu} \rangle = \frac{1}{2N} \sum_i \{ \langle \mathbf{S}_{i\mu} \cdot \mathbf{S}_{i+\delta\nu} + \mathbf{S}_{i\nu} \cdot \mathbf{S}_{i+\delta\mu} \rangle \}. \quad (2.10)$$

This represents correlation of a pair of spins separated by δ . When they have no interaction, triplet character and singlet(antiferromagnetic) character, its value approaches 0, 1/4 and -3/4, respectively.

2.3 FLAPW Band Calculations

2.3.1 LDA(Local Density Approximation)

Hamiltonians of realistic many-electron systems are generally described as

$$\mathcal{H} = \mathcal{H}_t + \mathcal{H}_v + \mathcal{H}_u, \quad (2.11)$$

$$\left\{ \begin{array}{l} \mathcal{H}_t = \sum_i \frac{1}{2m} \mathbf{p}_i^2 \\ \mathcal{H}_v = \sum_i v(\mathbf{x}) \\ \mathcal{H}_u = \frac{1}{2} \sum_{i \neq j} \frac{e^2}{|\mathbf{x}_i - \mathbf{x}_j|}. \end{array} \right. \quad (2.12)$$

Here \mathcal{H}_t and \mathcal{H}_v respectively represent kinetic energy and potential energy due to the Coulomb interaction with cations, which are one-particle Hamiltonians. On the other hand, \mathcal{H}_u represents the Coulomb interaction between electrons. For N -particle systems with large N , it is difficult to solve exactly the eigenvalue equation for the above Hamiltonian. Usually the interaction term \mathcal{H}_u is approximately treated by a self-consistent procedure on the basis of a one-particle picture. A typical and the most popular example of such approximations is the local density functional approximation (LDA), in which exchange and correlation energy part are represented by a functional of electron density [13, 14]. In this LDA, one-particle Schrödinger equation is expressed as

$$\left\{ \frac{1}{2m} \mathbf{p}_i^2 + v(\mathbf{x}) + \int \frac{n(\mathbf{x}')}{|\mathbf{x} - \mathbf{x}'|} d\mathbf{x}' + \varepsilon_{xc}[n(\mathbf{x})] \right\} \varphi_i(\mathbf{x}) = E_i \varphi_i(\mathbf{x}). \quad (2.13)$$

Number of functional forms are proposed for exchange and correlation potential $\varepsilon_{xc}[n(\mathbf{x})]$ [15].

2.3.2 FLAPW method

There are many methods to solve eq. (2.13). Here we explain the APW, LAPW and FLAPW methods.

APW method

First we explain the APW (augmented plane wave) method [16]. In this method we devide the space into two parts, which are the inside (region I) and the outside (region II) of the so-called muffin tin (MT) spheres (see Fig. 2.2). The MT spheres are defined as follows: (1) the center of each MT sphere is on the nuclear positions and (2) their radii are determined so that they do not overlap with each other. As basis functions, we use plane waves augmented with spherical harmonics inside the MT spheres (augmented plane wave: APW). Each APW, $\chi_{\mathbf{k}}^i$, is expressed explicitly as follows:

$$\chi_{\mathbf{k}}^i = \begin{cases} e^{i\mathbf{k}_i \cdot \mathbf{x}} & \text{outsideMT,} \\ 4\pi \sum_{\ell=0}^{\ell_{\max}} \sum_{m=-\ell}^{\ell} i^{\ell} j_{\ell}(\hat{k}_i R_s) Y_{\ell m}^*(\hat{k}_i) Y_{\ell m}(\hat{\rho}) \frac{R_{\ell}(\rho)}{R_{\ell}(R_s)} & \text{insideMT,} \end{cases} \quad (2.14)$$

where $\mathbf{k}_i = \mathbf{k} + \mathbf{G}_i$ with \mathbf{k} being a wave vector in the first Brillouin zone and \mathbf{G}_i being a reciprocal lattice vector, ρ is the position vector from the center of each MT sphere, \hat{k}_i and $\hat{\rho}$ denote respectively angular part of \mathbf{k}_i and ρ , and j_{ℓ} and $Y_{\ell m}$ represent spherical Bessel function and spherical harmonics, respectively. Radial functions R_{ℓ} satisfy

$$-\frac{1}{\rho^2} \frac{d}{d\rho} (\rho^2 \frac{dR_{\ell}}{d\rho}) + [\frac{\ell(\ell+1)}{\rho^2} + v(\rho)] R_{\ell} = E' R_{\ell}. \quad (2.15)$$

Here we notice that E' is set usually to be the same as the true eigenenergy E_i to be determined. Now eigenfunctions of eq. (2.13), $\varphi_{n,\mathbf{k}}$'s (n represents the band sufix), are expanded in terms of finite number of APW's $\{\chi_{\mathbf{k}}^i | i = 1, \dots, M\}$ as

$$\varphi_{n,\mathbf{k}} = \sum_{i=1}^M c_i^n \chi_{\mathbf{k}}^i, \quad (2.16)$$

and the expansion coefficients c_i are determined variationally.

In performing actual calculations by the APW method the crystal potential is treated by the MT approximation, that is, the potential is approximated to be constant in region II, while in region I it is treated by spherical approximation. This approximation seems to yield good results for high symmetric closed-packed structures.

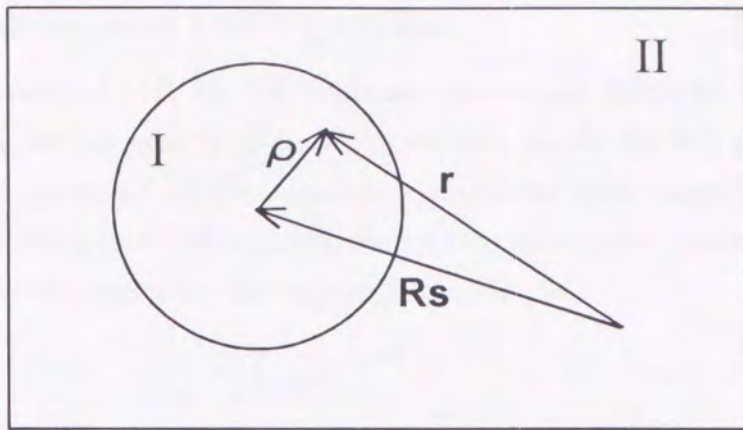


Figure 2.2: Muffin Tin (MT) sphere in a unit cell and definition of some vectors.

The APW method has been applied successfully to calculate electronic properties, particularly total energies and electron densities of various crystals. But it has two serious problems as follows:

1. Usual diagonalization procedures cannot be applied since radial functions inside the MT spheres depends on the eigenvalue E_i to be determined. Consequently calculations take too much time for large systems.
2. The MT approximation cannot be applied to low symmetric materials such as molecular crystals.

LAPW (Linearized APW) method

In order to improve the first difficulty, the LAPW method was developed [17]. In this method $R_\ell(E')$ in (2.15) is expanded with given $\{R_\ell(E_j)\}$:

$$R_\ell(E') = \sum_j c_j R_\ell(E_j), \quad (2.17)$$

where E_j 's represent given constant energies chosen appropriately. A set of c_j 's are determined from the continuous condition on the surface of MT spheres. With this approximation the eigenvalue and the eigenfunction of one-particle Schrödinger equation eq. (2.13) are calculated by usual diagonalization procedure, which can reduce considerably computational time. Here we note that reasonable results cannot be derived if given E_j 's are not suitable. In this thesis we use two energies, E_1 and E_2 .

FLAPW (Full-potential LAPW) method

The FLAPW method [18, 19, 20] improves the second difficulty. In this method the potential is treated as exactly as possible, namely, inside the MT spheres the potential is expanded in terms of spherical harmonic functions up to large ℓ and in the outside region it is expanded into Fourier components reciprocal lattice vectors \mathbf{G} . This FLAPW method gives good results for low symmetric materials.

Chapter 3

A Model of the Ferromagnetism of TDAE-C₆₀

An organic crystal tetrakis(dimethylamino)ethylene (TDAE)-C₆₀ has a very high magnetic transition temperature ($T_C=16$ K) for purely organic magnets. Existing experimental results suggest that the magnetic properties of TDAE-C₆₀ come mainly from C₆₀ anions and that ferromagnetic interaction exists between nearest neighboring (n.n.) C₆₀'s in clusters of nano-scale. However, the true nature of the magnetic state of TDAE-C₆₀ is still an open question. In this chapter we try to clarify the origin of peculiar magnetic properties of TDAE-C₆₀ by proposing a mechanism for ferromagnetic interaction between n.n. C₆₀'s.

3.1 Backgrounds

3.1.1 Main results of experiments

In 1991, Allemand *et al* first reported a ferromagnetic behavior of TDAE-C₆₀ as shown in Fig. 3.1 [5]. They insisted on TDAE-C₆₀ being a 'soft ferromagnet' because they observed no hysteresis of magnetization (see Fig. 3.2). They also suggested the possibility that it is an 'itinerant ferromagnet', which is fascinating for many scientists. Now, however, their suggestions are denied. First Suzuki *et al* discovered small hysteresis for magnetization [29]), and secondly the observed conductivity shows a semiconducting behavior [38]. Judging from the shape of the observed magnetization curve [30], Tanaka *et al* proposed a model of 'superparamagnetism' for TDAE-C₆₀. In this model ferromagnetic clusters consisting of hundreds spins fall into a paramagnetic state. The same mechanism is suggested

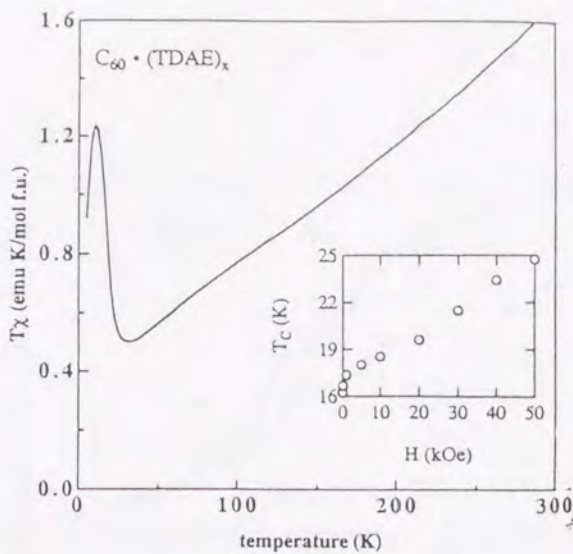


Figure 3.1: First reported magnetic susceptibility of TDAE- C_{60} [5].

by Blinc *et al* from proton NMR measurements [31]. Venturini *et al* proposed a 'spin glass model' on the basis of analyses of ESR lineshape and time decay of magnetization [34, 33]. It was reported that the magnetism have much to do with the orientation of C_{60} 's. These models, except for the spin glass model, are based on intermolecular ferromagnetic interaction between n. n. C_{60} 's. A report of muon spin relaxation also shows the existence of long range ferromagnetic order [35]. Recently Mihailovic *et al* suggested a "spin glassy nanocluster model" [36], where superparamagnetic clusters suggested by Tanaka *et al* are frozen. Then, the experiments supporting the spin glass model do not deny that the interaction between n. n. C_{60} 's is ferromagnetic, Thus it can be considered that TDAE- C_{60} is basically ferromagnetic, and their various peculiar properties are caused by molecular orientation.

Electronic properties of TDAE- C_{60} are also reported. One electron charge transfer from TDAE to C_{60} was reported by the energy shift of A_g mode of C_{60} in Raman scattering spectra. It is not metallic but semiconductor-like, which is confirmed by the measurements of microwave conductivity and optical conductivity [38, 39]. Furthermore, it is considered that an unpaired spin is mainly on C_{60} [40], but it is still not clear [41].

In summary, TDAE- C_{60} is not a metal but a Mott insulator with strong electron correlation or a Heisenberg material with further strong electron correlation. Further it may be considered as a spin glass of ferromagnetic nanoclusters where magnetic spins are localized on C_{60} ions. In this chapter we try to clarify the origin of ferromagnetic interaction between n.n. C_{60} 's and ferromagnetic ordering in nano-scale.

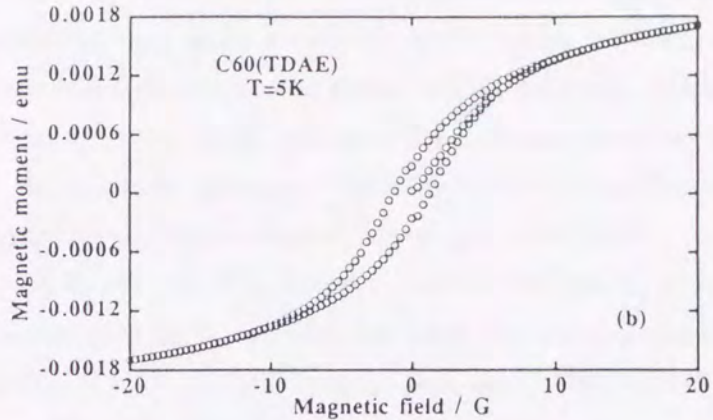


Figure 3.2: Magnetization curve of TDAE-C₆₀ [29].

3.1.2 Basic properties of C₆₀ molecule

It seems necessary for discussing the magnetism of TDAE-C₆₀ to understand first the properties of a single C₆₀ molecule.

Each C₆₀ molecule consists of sixty carbon atoms, which is a simple substance of carbon following graphite and diamond. Fullerene, often used in calling this kind of materials, is named after Buckminster Fuller, an architect, who have built many similar structures. Its existence was predicted by Osawa [44], and first discovered by Kroto *et al* in 1985 [45]. In particular, many studies have been reported since Kratschmer *et al* first produced the crystal of C₆₀ in 1990 [46]. Besides, many similar materials, higher fullerene, nanotube and so on, have been discovered. However, we do not refer to these materials furthermore.

A single C₆₀ molecule is characterized by twelve regular pentagons and twenty hexagons. (see Fig. 3.3(a)) There are two distinct types of bonds, one that separates two hexagons (b_{hh}) and the other that separates a pentagon and a hexagon (b_{ph}). Only for equal bond length are the hexagons regular. A number of spectroscopies have shown that they are equal to 1.40 ± 0.01 Å and 1.45 ± 0.01 Å, respectively, and the diameter of a molecule is about 7.1 Å.

In one molecular state, it has I_h symmetry, The symmetry of the molecule is independent of these two lengths. In consequence all carbon atoms are equivalent.

We can understand qualitatively the electronic states near the Fermi energy with the Hückel approximation, that is to say, we can find the degeneracy of the energy states as LUMO (Lowest Unoccupied Molecular Orbital) and HOMO (Highest Occupied Molecular Orbital) by considering only sixty π -orbitals and transfer between n.n. atoms. Furthermore, we can understand the electronic states more intuitively. Namely, as a first step we can regard C_{60} as a spherical shell, and then Schrödinger equation is the same as that of the angular part for a single hydrogen. Consequently the eigenfunctions are represented by spherical harmonics and their degeneracy is given as 1,3,5, ···. In the next step we must pay attention to the fact C_{60} is not spherical but has I_h symmetry. As the result the degenerate states split by I_h -type crystal field. We show the energy diagram near the Fermi energy in Fig. 3.3(b). HOMO is quintuply and LUMO is triply degenerate. Especially, LUMO is a part of splitted $\ell = 5$ states and has t_{1u} symmetry. This symmetric property is very important in discussing properties of C_{60} , since C_{60} molecules become anions in many famous compounds, in which LUMO is partly occupied.

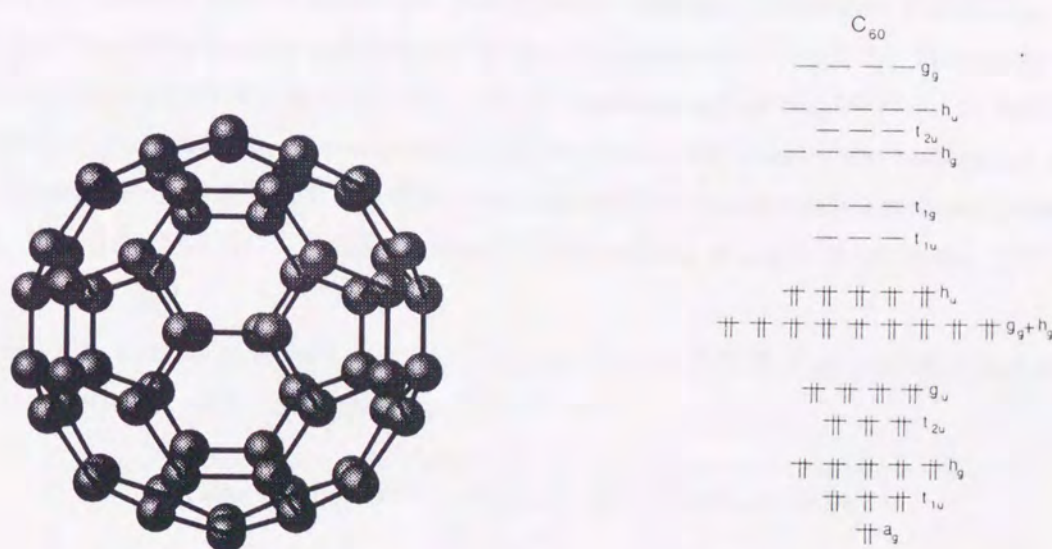


Figure 3.3: (a) C_{60} molecule (b)Simplified energy diagram of single C_{60} molecule. [43]

3.1.3 Crystal structure of TDAE-C₆₀ and its peculiarity

TDAE-C₆₀ has a very high 'Curie temperature' $T_C=16$ K as organic compounds and the unique ferromagnet in Fullerene materials (it was reported that C₆₀-IBr shows ferromagnetic behavior, but it is unclear [51] at present). This interesting magnetic behavior of TDAE-C₆₀ seems to be related with the peculiarity of its crystal structure.

The crystal structure of TDAE-C₆₀ was first reported by Stephens *et al* for a powder sample. It is shown in Fig. 3.4 [49]. Figure 3.5(a) represents a schematic structure of C₆₀'s only. Here we must remark that C₆₀'s do not constitute a FCC structure like other C₆₀-based materials but an orthorhombic-like structure, which may be caused by larger size of TDAE molecules compared with alkali metals and so on. According to later reports for a single crystal, the unit cell consists of two subcells that were deduced from powder diffraction data and they are stacked along the *c*-axis with TDAE atoms being shifted along the *b*-axis alternately [50]. Suzuki *et al* also succeeded in synthesizing a TDAE-C₆₀ single crystal. But it may be different phase because it does not behave ferromagnetically and its lattice constant is quite different from the Blinc's sample [52].

Now, we discuss the reason for peculiar physical properties of TDAE-C₆₀ in connection with its peculiar crystal structure. The greatest difference between TDAE-C₆₀ and other organic magnets can be pointed out to be the symmetric property. Generally speaking, organic molecule has low symmetry, which is advantage of singlet state in both itinerant and localized systems. Consequently the low symmetry makes the realization of organic ferromagnet more difficult. On the other hand, higher degeneracy is realized in monovalent C₆₀ (which is true in TDAE-C₆₀) since LUMO of C₆₀ is triply degenerate, which may be

Table 3.1: Lattice constant and inner parameters of TDAE-C₆₀ crystal. Only coordinate of the center of molecules are shown. [50]

lattice constant	$a=15.858\text{\AA}, b=12.998\text{\AA}, c=19.987\text{\AA}$ $\beta=93.37^\circ$
space group	$C2/c$
C ₆₀	(0,0.5,0),(0,0.5,0.5),(0.5,0,0),(0.5,0,0.5)
TDAE	(0.5,0.502,0.75),(0.5,0.498,0.25) (0,0.002,0.75),(0,-0.002,0.25)

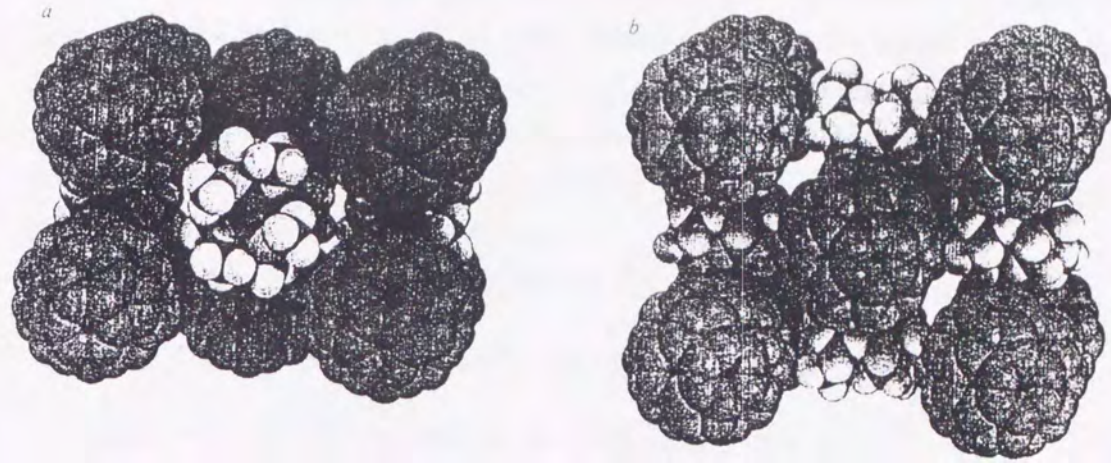


Figure 3.4: First reported crystal structure of TDAE- C_{60} . [49]

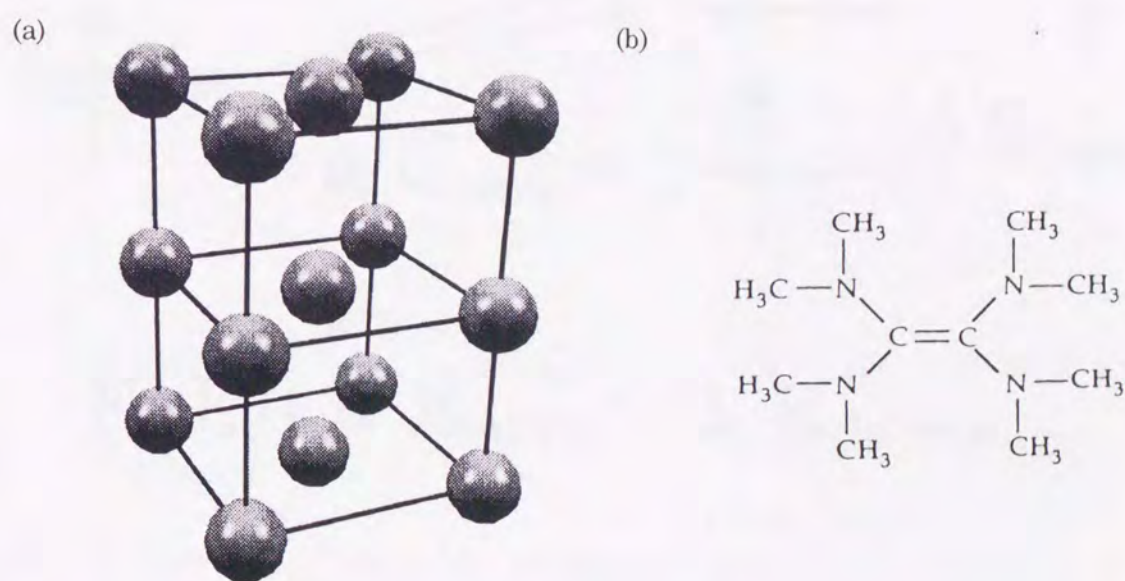


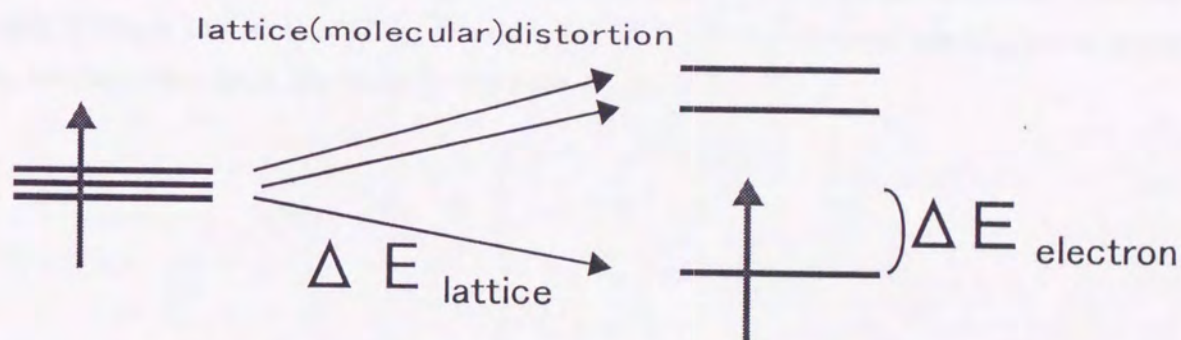
Figure 3.5: (a)Simplified crystal structure of TDAE- C_{60} , where spheres represent C_{60} molecule and TDAE molecules are omitted. (b)TDAE molecule

advantageous for ferromagnetic states.

Furthermore monovalent C₆₀ compounds show peculiar properties among fullerene compounds. For example, RbC₆₀ has the structure like one-dimensional polymer [53]. It may be caused by the Jahn-Teller effect, which occurs when degenerate state is occupied partly (see Fig. 3.6). Koga *et al* performed molecular orbital (MO) calculations for C₆₀⁻ with some distortion and found that C₆₀⁻ is the most stable for distortion with D_{2h} or D_{3h} symmetry. Furthermore, RbC₆₀ has a SDW phase and this suggests that magnetic states may be stable generally in C₆₀⁻ compounds.

As the result, characteristics of TDAE-C₆₀⁻ are summarized as follows:

1. high degeneracy near the Fermi energy
2. splitting of LUMO caused by the Jahn-Teller effect
3. strong electron correlation, which is distinction of organic molecules
4. orthorhombic-like network of C₆₀⁻'s



$$E = E_0 + \Delta E_{\text{lattice}} - \Delta E_{\text{electron}}$$

Figure 3.6: Jahn-Teller distortion.

3.2 Role of Jahn-Teller Distortions

3.2.1 Charge transfer induced Jahn-Teller distortion

First we discuss a role of charge-transfer induced intramolecular Jahn-Teller (CTJT) distortion for the electronic states of a single C_{60} molecule. We have carried out the semi-empirical MO calculations for C_{60} , C_{60}^- , and C_{60}^{2-} by the PM3 method. The molecular structure has been optimized by the restricted Hartree Fock (RHF) calculation, and furthermore the electronic states were calculated by taking account of configuration interaction.

Structure optimization

We must give the initial structure since structure optimization is done with self-consistent procedure. In this paper, the structure of a nondistorted C_{60} (I_h symmetry) is used as an initial state [42]. This structure has two parameters, r_{hh} and r_{ph} , which respectively represents the length of b_{hh} and b_{ph} . If the cartesian axes are chosen to extend from the origin through the centers of b_{hh} bonds lying on the two-fold axes, the C_{60} point group can be generated from the three group operations,

$$\begin{aligned} R_5 &= \begin{pmatrix} \tau^{-1} & 1 & \tau \\ -1 & \tau & \tau^{-1} \\ \tau & \tau^{-1} & 1 \end{pmatrix}, \\ P &= \begin{pmatrix} 0 & 1 & 0 \\ 0 & 0 & 1 \\ 1 & 0 & 0 \end{pmatrix}, \\ I &= \begin{pmatrix} -1 & 0 & 0 \\ 0 & -1 & 0 \\ 0 & 0 & -1 \end{pmatrix} \end{aligned} \quad (3.1)$$

where $\tau = (\sqrt{5}+1)/2$. The operation R_5 is a rotation by $2\pi/5$ about a fivefold axis, P is a cyclic permutation of the axes, and I is the inversion operation. For C_{60} , the structure optimization has been carried out with regarding only r_{hh} and r_{ph} as optimizing parameters. This procedure is based on the idea that Jahn-Teller distortion cannot occur in a closed shell molecule C_{60} . Figure 3.7 shows an isopath diagram for the total energy. r_{hh} and r_{ph} of the stable state are obtained as 1.385\AA and 1.4575\AA , respectively, which

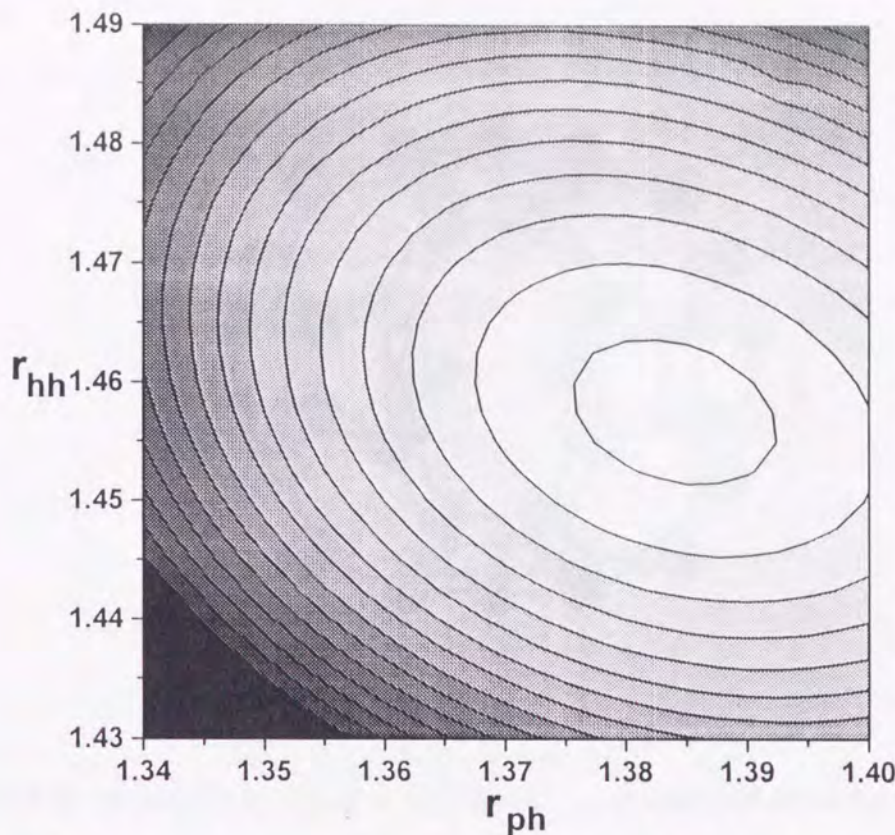


Figure 3.7: An isopath diagram for total energy of single C_{60} molecule shown for the space of r_{ph} and r_{hh} .

agree with the experimental values, 1.391 Å and 1.455 Å. In similar calculations with the MNDO method by Saito *et al*, r_{hh} and r_{ph} were determined to be 1.40 Å and 1.474 Å [47]. We find that these values are improved by using the PM3 method.

Next we carried out the calculations for C_{60}^- . As stated before, Koga *et al* reported that one C_{60}^- is most stable with D_{2h} or D_{3d} symmetry distortion. In TDAE- C_{60} , it may be expected that the molecular structure with D_{2h} distortion is more stable than that with D_{3d} distortion in TDAE- C_{60} crystal since orthorhombic-type crystal field acts at the C_{60} site. Therefore, in this paper we consider only D_{2h} structure for C_{60}^- anion. The molecular structure of C_{60}^- has been optimized starting from ideal icosahedral structure (I_h symmetry). The optimized structure looks like a rugby ball elongated along one of the three-fold symmetry axes in D_{2h} structure, which is shown in Fig. 3.8. The atomic displacement from the ideal icosahedron is rather small, *i.e.* 0.01 Å at most.

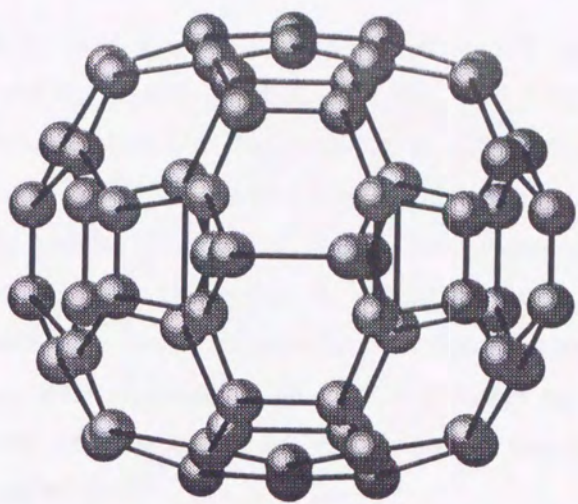


Figure 3.8: molecular struture of C₆₀⁻ anion. magnitude of distortion is overstated 40 times.

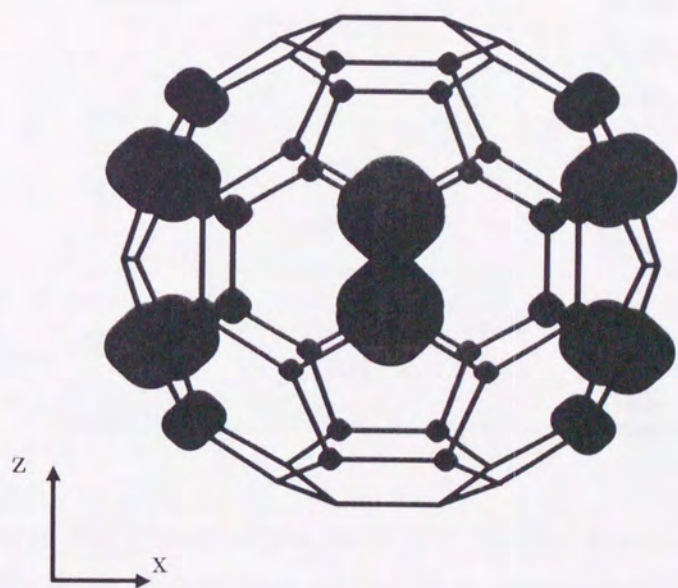


Figure 3.9: Charge density of LUMO_z

One-electron states

One-particle HF energy diagram of C_{60} and C_{60}^- with each optimized structure is given in Table 3.2. The three t_{1u} states, $LUMO_x$, $LUMO_y$, and $LUMO_z$, which are degenerate in C_{60} with I_h symmetry before the charge-transfer, split into three states in C_{60}^- . If the elongated axis is z -axis, $LUMO_z$ has the lowest energy, and the energies of the other two orbitals, $LUMO_x$ and $LUMO_y$ states, are almost degenerate. Charge density of the lowest LUMO orbital is shown in Fig.3.9. It should be noted that the charge density is not spherical but takes large values along the belt around the elongated axis. We must remark that three t_{1u} state is generated from $\ell = 5$ states by crystal field splitting and that the charge density of these states are not spherical but take large values along the belt around the elongated axis.

Table 3.2: One-particle HF energy diagram of C_{60} and C_{60}^- with each optimized structure

	$C_{60}(I_h)$		$C_{60}^-(D_{2h})$
HOMO	-9.48 (quintuple)	split →	-6.45 -6.41 -6.30 -6.19 -6.16
LUMO	-2.89 (triple)	split →	-1.50 0.20 0.20
NLUMO	-2.20 (triple)	split →	0.58 0.61 0.95

Since energies of the excited states cannot be derived exactly with the HF approximation, it is difficult to discuss inter-molecular magnetic interaction caused by charge transfer within the HF approximation. Therefore we have calculated many-body eigenstates with multi-electron configuration interaction (MECI). The calculations were carried out for C_{60} , C_{60}^- and C_{60}^{2-} with the optimized structure for C_{60}^- because C_{60} seems to be monovalent on the average in TDAE- C_{60} . Six orbitals, LUMO and second LUMO, are

used for active space. Calculated energy diagram and main part of eigenfunction for C_{60} and C_{60}^- are shown in Table. 3.3.

Table 3.3: Energy diagram and main part of eigenfunction for C_{60} , C_{60}^- and C_{60}^{2-} calculated by the PM3-MECI method. $|n\rangle$ represents the state where the n -the lower orbitals of splitted LUMO of C_{60} are occupied.

	C_{60}	3.109
	0.000	$ 1\rangle$
C_{60}^-	0.220	$ 2\rangle$
	0.225	$ 3\rangle$
C_{60}^{2-}	-0.305	$ 1, 1\rangle$
	0.017	$ 1, 2\rangle$ (triplet)
	0.024	$ 1, 3\rangle$ (triplet)
	0.152	hybridizing many orbital
	0.155	$ 1, 3\rangle$ (singlet)
	0.156	$ 1, 2\rangle$ (singlet)

3.2.2 Role of CTJT interaction for inter-molecular magnetic interaction

We have discussed the effects of CTJT distortion on electronic states of a single C_{60} . Now we try to elucidate its role for magnetic interaction between two C_{60}^- 's. Since intermolecular transfer interaction between two orthogonal LUMO's is vanishing, the magnetic interaction depends sensitively on the relative orientation of the molecular axis of the two C_{60}^- anions. In Figs. 3.10 (1) and (2), the elongated axes of two C_{60}^- 's are parallel to each other. In these alignment, intermolecular transfer interaction between the ground state and the excited state orbitals are vanishing. Then we can neglect reasonably the excited state orbitals, because the energy difference between the ground state and the excited state orbitals is typically a few tenth eV and the number of unpaired electrons is one per C_{60}^- ion. In this alignment, intermolecular transfer only exists between same orbitals. Furthermore, unpaired electrons are located on lower states due to orbital energy difference. Thus intermolecular magnetic interaction can be discussed only with single state

and one unpaired electron per molecule. As the result, and also because of one electron per C_6^- ion, the system can be described effectively by a single-band Hubbard model with half-filled electrons. In this case it is well known that intersite magnetic interaction is antiferromagnetic. On the other hand, if the elongated axes of two C_6^- 's are perpendicular or twisted to each other (examples are shown in Figs. 3.10 (3)and (4)), it is regarded as orbital ordering system, and the magnetic interaction between the two C_6^- ions will be ferromagnetic, which can be understood by the second-order perturbational calculation with respect to the transfer energy for the two-site multi-band Hubbard model. Thus, it is expected that the C_6^- crystal will be ferromagnetic if C_6 anions are aligned so that their elongated axes appear perpendicular or twisted to each other in an alternating way as the result of the cooperative Jahn-Teller (CJT) distortion.

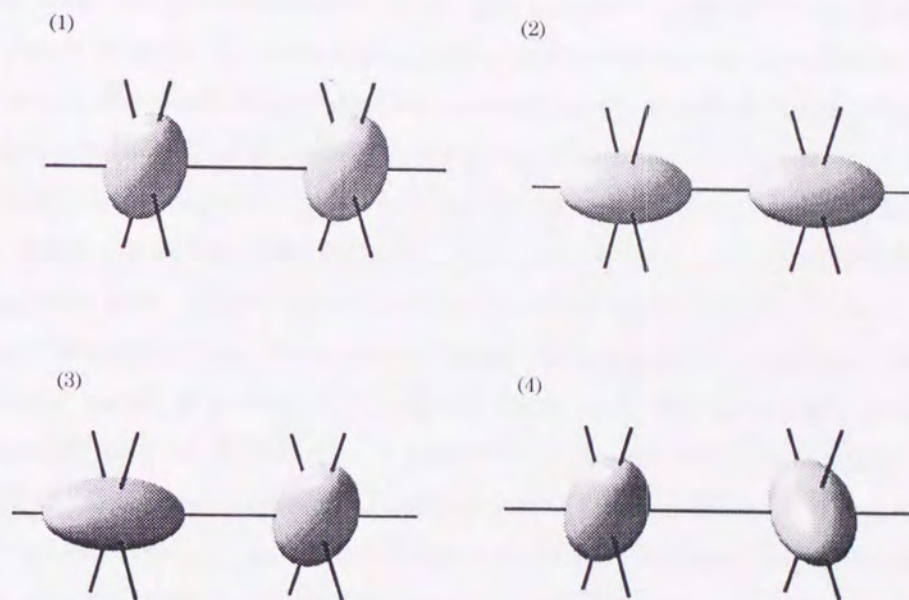


Figure 3.10: Four examples of alignment of pair of nearest C_6^- 's.

3.2.3 Cooperative Jahn-Teller effect and the origin of ferromagnetism

Now we investigate more explicitly a possibility of ferromagnetic ordering in C_6^- systems on the basis of one-dimensional multi-band Hubbard Hamiltonian described by eq. (2.3).

For simplicity we consider only two orbitals for each molecule, *i.e.* the nearly degenerate LUMO's in real C_{60}^- anions are replaced with single orbital. The electron number is fixed as one per molecule, *i.e.* quarter-filling is assumed. We have assumed the one-dimensional molecular arrangements as shown in Fig. 3.11. Strictly speaking, the transfer energy between adjacent $LUMO_z$'s and that between adjacent $LUMO_x$'s are different, but for simplicity they are assumed to be the same and represented by t . The orbital energy difference is denoted by V , and the value of V and the other intramolecular parameters (U and J) are roughly estimated from RHF-CI calculations with use of six molecular orbitals for C_{60}^{x-} ($x = 0, 1, 2$). The results are $V \sim 0.2$ eV, $U \sim 3.0$ eV and $J \sim 0.1$ eV ($U/J \sim 30$ and $V/J \sim 2$). It is noted that these values should be taken not seriously but only as typical values. As for the transfer energy t we have no reliable information. However, we expect the value of t is less than 0.1 eV, referring to the results of band calculations for the FCC C_{60} crystal [54].

If we want to give discussion for a wide range of t and U including the insulating region (Mott insulator), mean-field type approximations are insufficient. Therefore we have adopted the exact diagonalization procedure of finite size chains with use of periodic boundary condition. As an example of our calculational results we show in Fig. 3(b) the phase diagram of the ground state in the plane of $\tau \equiv t/J$ vs. $v \equiv V/J$, which is obtained for the chain size $N=6$. The value of U is fixed as $U/J=30$. It is clearly seen that the ferromagnetic state ($S_{\text{tot}}=3$) is the ground state for a wide range in the $\tau - v$ plane. If we increase τ from zero, the ferromagnetic state becomes unstable against the $S_{\text{tot}} = 0$ state (spin singlet state) at a critical τ_c , and the value of τ_c increases with increasing v .

The value of τ of TDAE- C_{60} is expected to be smaller than τ_c and thus we point out that the ferromagnetism of TDAE- C_{60} can be caused by the orbital ordering. A realistic arrangement of C_{60}^- anions which is favorable for three dimensional ferromagnetic ordering will be pointed out in the next section. We also calculated a set of correlation functions, which are shown in Table 3.4. We can see that $\langle n_\mu \rangle$ does not change for each state, which is understood as electrons are localized in lower states even if occupancy of upper state becomes larger gradually by transfer increasing. Small value of $\langle (\delta n)^2 \rangle$ also keeps across a boundary of the magnetic state. These results indicate that the system is insulating. Thus the transition at τ_c is expected to be a transition from a ferromagnetic to a spin-singlet insulator.

However, $\langle S_i \cdot S_{i+\delta} \rangle$ change its value dramatically on magnetic transition. In the high spin state, it keeps $\frac{1}{4}$ independent of δ . In low spin state, on the other hand, δ

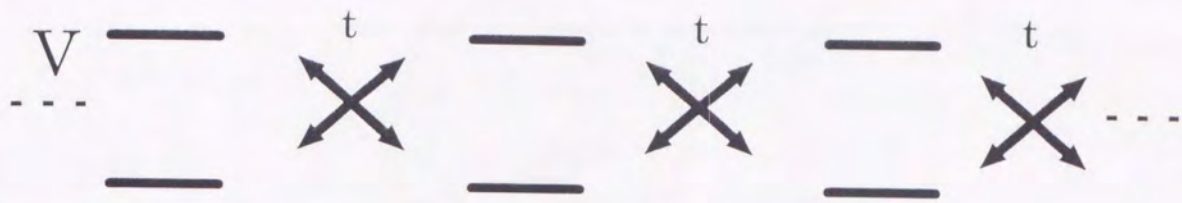


Figure 3.11: Transfer structure of one-dimensional multi-band Hubbard model applied ED calculation. t and V respectively represent intermolecular transfer and orbital energy difference.

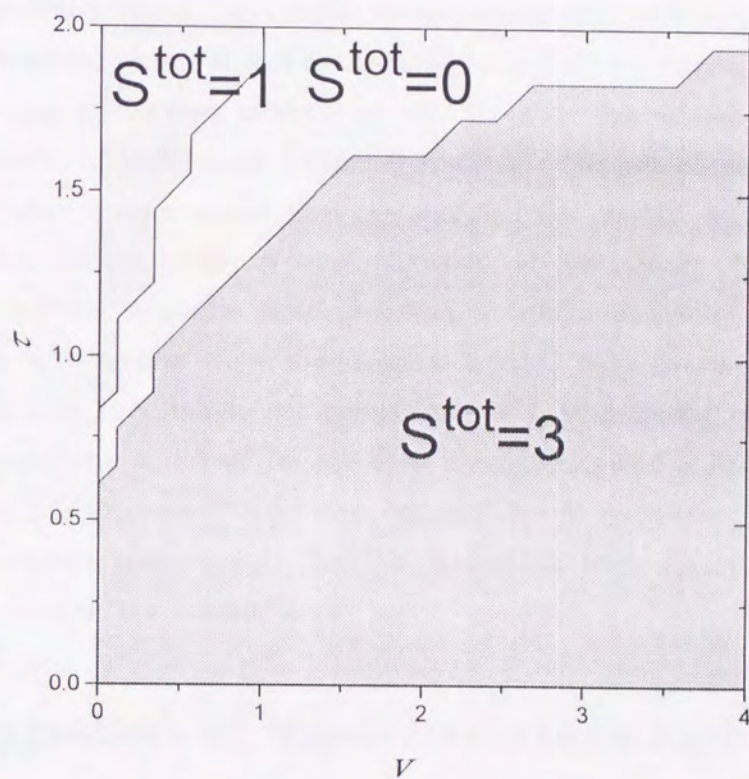


Figure 3.12: Magnetic phase diagram for one-dimensional multi-band Hubbard model with $U/J=30$ and $N=6$, where U , J , and N represent intra-molecular Coulomb energy , intra-molecular exchange energy and the number of molecule in the system. τ, v represent $t/J, V/J$ respectively, where t and V represent intermolecular transfer and orbital energy difference.

Table 3.4: A set of correlation functions for each τ with $N=6, U/J=30, v=2$

τ	1.20	1.40	1.60
S^{tot}	6	6	0
$\langle n_1 \rangle$	0.498	0.497	0.495
$\langle n_2 \rangle$	0.002	0.003	0.005
$\langle (\delta n_1) \rangle$	0.004	0.006	0.009
$\langle (\delta n_2) \rangle$	0.004	0.006	0.009
$\langle \mathbf{S}_i \cdot \mathbf{S}_{i+1} \rangle$	0.248	0.247	0.130
$\langle \mathbf{S}_i \cdot \mathbf{S}_{i+2} \rangle$	0.248	0.247	-0.217
$\langle \mathbf{S}_i \cdot \mathbf{S}_{i+3} \rangle$	0.248	0.247	-0.563

dependency is clearly found, from which we can speculate that this singlet state may have a helical-like spin structure. It will be discussed minutely in chapter 4.

Before moving to the next section, we refer to other theoretical works on magnetism or ferromagnetism of multi-band Hubbard systems. The model system investigated by Roth[26] is similar to ours except that she assumed the doubly degenerate orbitals. She first pointed out the possibility of ferromagnetism of this system. Inagaki and Kubo[27] have constructed the magnetic phase diagram of Roth's model on the basis of the HF calculation for a particular three dimensional lattice. It is noted that the existence of orbital energy difference makes an appearance of ferromagnetic state easier. On the other hand, Kusakabe and Aoki[28] reported a rigorous proof of the ferromagnetism for arbitrary band filling in case of $J=U'=\infty$, where J and U' represent inter-orbital exchange and Coulomb energy, respectively. Their discussion has been done for a parameter space different from that in the present work.

3.3 Suggestion of Superstructures and Methods to Survey

In the previous section it is suggested that ferromagnetic ordering can be possible in C_{60}^- crystals if, as the result of CJT distortion, C_{60}^- anions are arranged so that appropriate orbital ordering is realized. For simplicity, we consider only C_{60} molecules are aligned

orthorombically as shown in Fig. 3.5. For bulk ferromagnetic behavior being realized, all pairs of n.n. C_{60}^- 's should be connected as shown in Fig. 3.10 (3) or (4). As examples of molecular arrangements which are likely to cause three dimensional ferromagnetic order, we propose C_{60}^- crystal structures as shown in Fig. 3.13. These structures consist of C_{60}^- linear chains with the same molecular arrangement as shown in Fig. 3.10 (3) or (4). Thus intrachain interaction is naturally ferromagnetic. Furthermore, in structures shown in Figs. 3.13 (a), (b) and (c), the interchain interaction is expected also ferromagnetic because the elongated axes of the nearest neighboring interchain C_{60}^- anions are perpendicular or twisted each other. The other structure have antiferromagnetic connection, but there is a possibility of showing ferromagnetic behavior.

We must discuss which structure is most stable. However, it seems to be impossible to prospect the most stable structure by calculating cohesive energy of each structure. Therefore we try to suggest a couple of experimental approaches which make the crystal structure clear and can confirm our mechanism to cause the ferromagnetism in TDAE- C_{60} based on the CTJT and the CJT distortions.

1. Change of crystal structure at low temperature

The first one is the X-ray diffraction measurement. If we can observe the JT-distortion of each C_{60} anion in TDAE- C_{60} by determining the atomic positions with quite accurate X-ray diffraction, it becomes a direct evidence of our model. Furthermore, new Bragg peaks may be observed since the structure shown in (a) has $P\bar{1}$ symmetry instead of $C2/c$ which is the symmetry group of non-distorted TDAE- C_{60} . Change of symmetry in other structures are shown in Table 3.5. It is noted that these experiments should be carried out at least below 10 K because C_{60} in TDAE- C_{60} is rotating at high speed above about 30K and spin-glass transition at 10 K has been reported.

Table 3.5: symmetry group of structures shown in Fig. 3.13

(a)	(b)	(c)	(d)
$P\bar{1}$	$P\bar{1}$	$C2/c$	$P\bar{1}$

2. Polarization of spin density.

It should be noted that the above measurement to determine the crystal structure

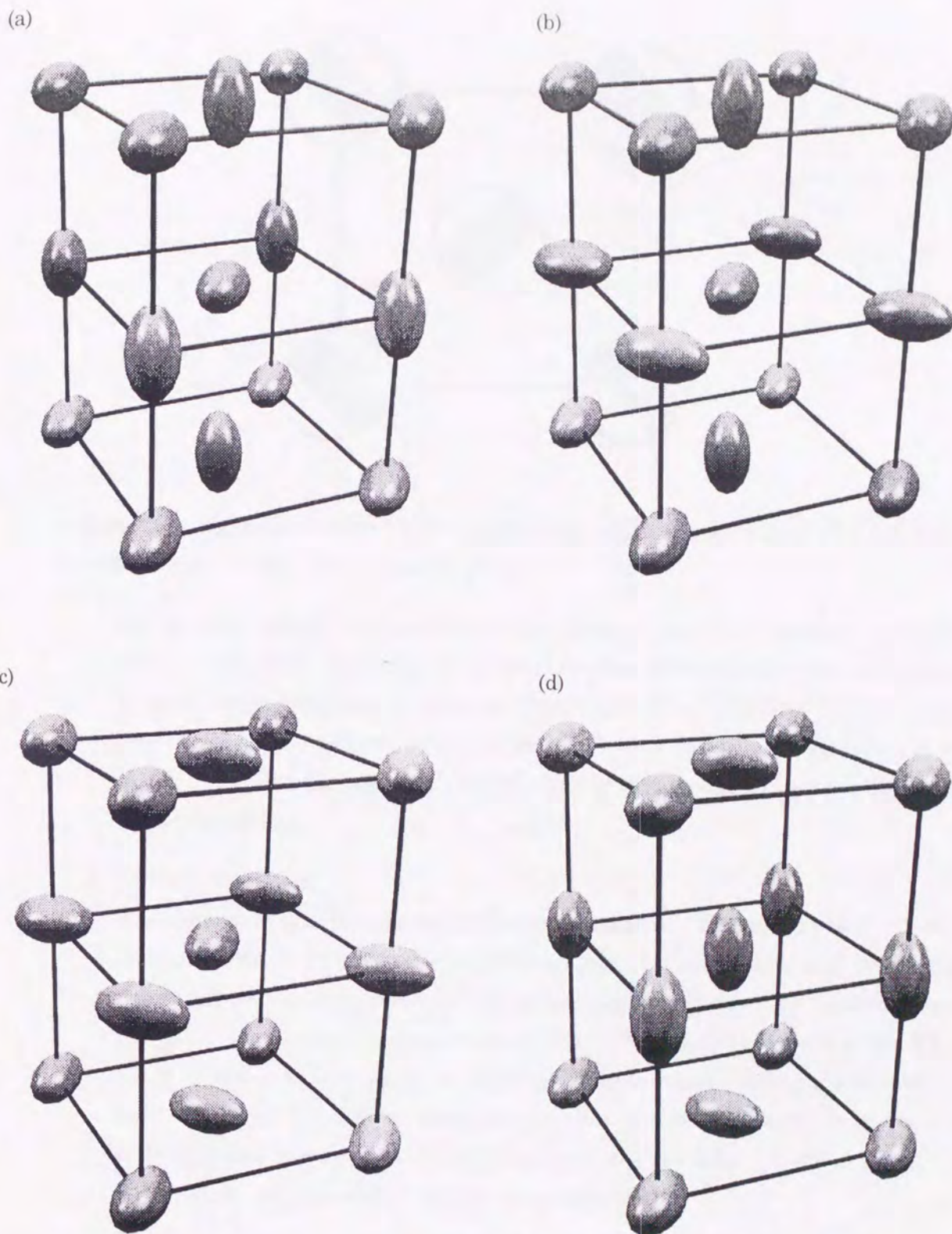


Figure 3.13: Examples of structures of CJT distortion considered as showing the balky ferromagnetic behavior.

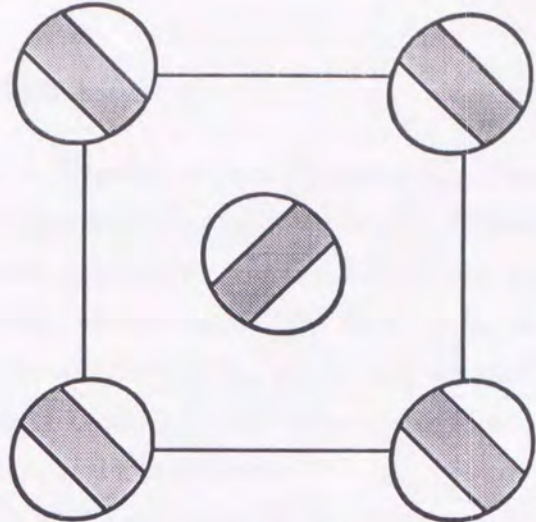


Figure 3.14: Schematic view of spin density map which can be detect with neutron defraction measurement if our model is realized.

will be quite difficult because the atomic displacements from the ideal icosahedron is rather small as mentioned in the previous section. However distortion of spin density is quite larger than that of structure because most of unpaired electrons may fall into one of LUMO orbitals, which make spin density into belt like structure as shown in Fig. 3.14. This distortion can be detected by spin polarized neutron diffraction at low temperature.

3. Optical properties

The second is the Raman scattering measurement in single crystals. Since the Raman tensor in $P\bar{1}$ structure is different from that in $C2/c$, it may be possible to determine the crystal symmetry from polarization analyses of the Raman scattering. For example, in case of the structure shown in Figs. 3.13 (a) (space group $P\bar{1}$), A_{1g} mode is observable in such an off-diagonal polarization configuration where the scattering light is polarized along y -axis while the incident light along the x or z -direction, but in case of the structure shown in Figs. 3.13 (c) (space group $C2/c$), A_{1g} mode is not observable in such a configuration.

In other approaches, we precede the discussion only considered CTJT distortion. In measurement for simple C_{60} , only A_{1g} and H_{1g} modes are detected, if C_{60} is distorted into D_{2h} symmetry, off-diagonal polarization of B_{1g}, B_{2g} and B_{3g} modes become detectable.

3.4 Discussion

The most important consequence of this chapter is that the magnetic interaction between two CTJT-distorted C_{60}^- 's depends sensitively on the relative orientation of their molecular axes and ferromagnetic interaction is realized when the elongated axes of two C_{60}^- 's are perpendicular or twisted to each other. We have suggested that bulk three-dimensional ferromagnetism can be realized if C_{60} anions are aligned so that their elongated axes appear perpendicular or twisted to each other in an alternating way as the result of the cooperative Jahn-Teller (CJT) distortion.

Here we point out that our model for the magnetic interaction between two CTJT-distorted C_{60}^- 's may explain qualitatively the spin-glass like behaviors observed in TDAE- C_{60} . In fact we can consider two types of mechanism for spin-glass like behaviors within our model. The first one is the formation of ferromagnetic nanoclusters which may be realized through stacking fault which is shown in Fig. 3.15. The aggregation of these ferromagnetic nanoclusters may give also spin-glass like behaviors (spin glassy nanocluster model[36]). The second one is the random distribution of exchange coupling, which may be realized by random orientation of C_{60} molecules (see Fig. 3.16). It is noted here that ferromagnetic interaction between C_{60} can be converted even into antiferromagnetic one by changing the relative orientations of C_{60} . Such a random distribution of the exchange coupling can give a usual type of spin-glass behaviors.

Finally we give discussion about the validity of our assumptions used in this chapter and the problems unresolved.

1. Assumptions for simplicity

- Ignorance of unpaired electrons on TDAE

In this paper we have discussed only the magnetism of C_{60} anions in TDAE- C_{60} . Since TDAE $^+$ ions have unpaired electrons, we naturally expect that TDAE $^+$ ions also contribute to the magnetism of TDAE- C_{60} . Experimentally, however, the spins on TDAE $^+$ ions seem to be quenched, but it was reported that spin moment seems to exist on protons of TDAE by proton NMR. [55] This problem is a puzzle at present. As a possible origin of the disappearance of magnetic moments on TDAE $^+$ ions we may consider the occurrence of the spin Peierls transition on TDAE $^+$ chains along the c -axis and moment of C_{60} is spread out to protons of TDAE. But such a shift has never been reported yet. On the other hand, there is a report that ESR spectra can be explained even if unpaired electrons exist on TDAE and a strong

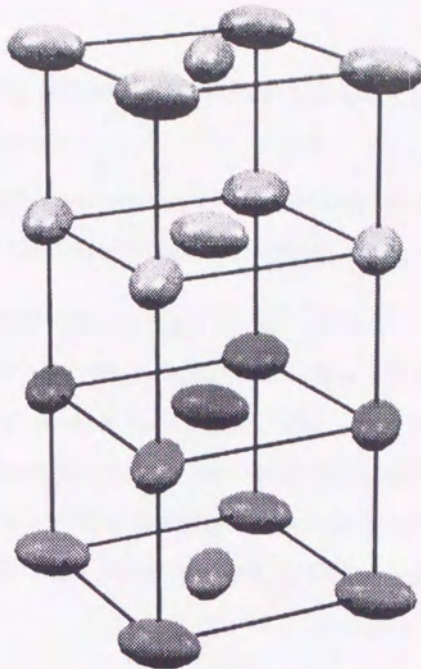


Figure 3.15: Schematic view of stacking fault which can be the origin of spin-glass behavior. Dark cluster and light cluster connect with stacking fault.

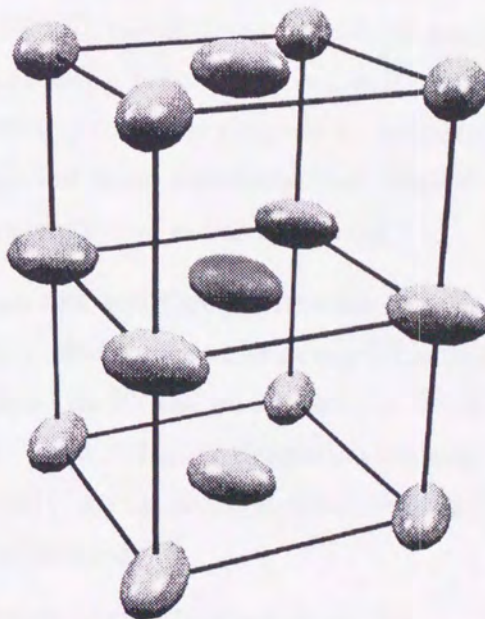


Figure 3.16: Schematic view of local randomness which can be the origin of spin-glass behavior. Dark molecule has antiferromagnetic interaction between nearest molecules due to rotating from CJT alignment.

exchange coupling between C_{60} and TDAE prevails [41] We need more discussion about this problem.

However, the length between C_{60} 's is shorter than that of FCC C_{60} crystal. It seems to be reasonable that the origin of ferromagnetism is the interaction between C_{60} 's.

- Orthorhombic structure of C_{60}

In this thesis, we have an assumption that TDAE- C_{60} has orthorhombic structure. However, actually it has monoclinic one. structural parameters are shown in Table 3.1. In ab -plane, the angle between lines along nearest neighbors are not right-angle but 78.3° since the length of a -axis and b -axis are different. Consequently, all orbitals on different sites are not orthogonalized. We may have to survey these effects.

- Neglection of some terms in Hubbard model

The most important term neglected in our Hubbard Hamiltonian is

$$-\sum_{i\mu\nu\sigma} J' c_{i\mu\sigma}^\dagger c_{i\mu\bar{\sigma}}^\dagger c_{i\nu\sigma} c_{i\nu\bar{\sigma}} \quad (3.2)$$

which has the same value as that of exchange energy J . However, this term is included in the MO-CI calculations. Hubbard parameters are determined so that low energy parts of many body states are well reproduced. Differences of the result caused by neglecting of this term may not be important. On the other hand, the term must not be neglected when intermolecular transfer energy is larger than Coulomb energy. The other neglected terms are trivial.

- Difference between one and three dimension

Generally speaking, electronic states in one dimension are quite different from those in higher dimension. As for the intermolecular ferromagnetic coupling, however, we expect it is rather large in higher dimension because of increasing of the interaction paths. Consequently, it can be considered that ferromagnetic state becomes more stable in higher dimension.

2. Problems in calculational procedure

- Size dependency in ED procedure

As shown in chapter 2, the most terrible disadvantage of ED procedure is that the system size is limited by computational speed and amount of memory of computers. In this chapter, ED calculations were carried out for $N \leq 8$ systems. We must

survey the size-dependency of magnetic phase diagram. Figure 3.19 shows the size-dependency of τ_c which is defined as the value of transfer where high spin - low spin transition occurs. We found τ_c is converged quite rapidly to a finite value (~ 1.6), which indicate that calculation error due to the system size is negligible.

- Estimation of parameters in Hubbard Hamiltonian

Only six one-particle basis functions, which are LUMO and next LUMO of C_{60} , are used in semi-empirical MO calculations to estimate the parameters in our Hubbard Hamiltonian. Small number of bases may make the intramolecular Coulomb energy overestimated because screening effects cannot be calculated correctly. To improve of this problem, number of one electron bases must be increased. As a first step, five orbitals of HOMO need to be included in CI calculations. In this case, number of many-particle bases is about 6000, for which calculations can be carried out with Lanczos method. To improve this problem completely, however, full-CI calculation is needed, which is impossible. Instead of carrying out such CI calculations we have investigated the U -dependency of the phase diagram. The phase diagrams for different U values are shown in Figs. 3.17, 3.18 and Fig. 3.20. It is found that τ_c is decreased as reducing U but that the shape of the phase diagram does not change basically. Therefore the calculations in this chapter may have a significance sufficiently.

3. Necessity of further discussion for some experimental results

- Semiconductor-like conductivity

At first TDAE- C_{60} was considered as an itinerant ferromagnet. Now it is clear that conductivity of TDAE- C_{60} shows a semiconductor-like behavior. However, the reason is open to question. A valence electron exists on a molecule, which excludes the possibility of band insulator. Meanwhile it may not be a normal Mott insulator because the length between C_{60} 's along the c -axis is shorter than alkali-doped C_{60} which is a metallic compound.

Here we suggest some mechanisms for semiconducting behaviors:

1. Reduction of transfer energy by CJT distortion

Charge density of frontier electron on C_{60} takes the form of a belt due to CTJT distortion. Therefore intermolecular transfer energy will become small if an appropriate CJT distortion occurs. For example, in case of the crystal

structure shown in Fig. 3.10(4), intermolecular transfer becomes quite small. This reduction may make the material semiconducting.

2. Existence of an energy gap induced by CJT distortion or displacement of TDAE
The unit cell of TDAE-C₆₀ in the above CJT distorted structure include two TDAE molecules and two C₆₀'s, which can make an energy gap at the Fermi surface.

3. Scattering at the interface between nanoclusters

TDAE-C₆₀ is said to form spin-glassy nanoclusters at low temperatures. Scattering by structural or magnetic disorder at the interface between nanoclusters can be the reason of semiconducting. In this case, optical conductivity like metallic granular nanoparticle may be detected below the temperature of transition to spin glass.

4. Rotational disorder of C₆₀

TDAE-C₆₀ is quite anisotropic compared with other C₆₀ compounds. Therefore, electronic conductivity may be sensitive to molecular rotation. At high temperature, this material can fall to semiconducting state due to this reason. In this case, this material may be metallic below T_{SG} .

In 1 and 2, CJT distortion is the origin, while in 3 and 4, disorder is important. For further discussion, measurements of conductivity to very low temperatures are required.

- Weak ferromagnetic behavior in ESR measurement

Blinc *et al* have reported the magnetic anisotropy in ESR measurement of single crystal[50], that is, ferromagnetic behavior has been observed along the *a*-axis, but along the *c*-axis the peak shift indicates antiferromagnetic behavior. They concluded a Dzyaloshinsky-Moriya (DM) type mechanism is responsible for the ferromagnetic ordering of TDAE-C₆₀. However, anisotropy of the g-value is quite small. Furthermore the magnitude of weak ferromagnetism in other organic magnets is about 10⁻³, which is much smaller than the magnetization of TDAE-C₆₀. It is hard to consider that only this interaction is the origin of the ferromagnetic behavior of TDAE-C₆₀. The following mechanisms can be suggested.

- Weak antiferromagnetism caused by DM interaction

The DM interaction can exist certainly due to low symmetry. Then the ESR

spectra reported by Blinc may be understood if TDAE-C₆₀ has such a ferromagnetic spin arrangement in which alternating cant of spins is caused by the DM interaction.

– Coexistence of ferromagnetic domain and antiferromagnetic one

If CJT interaction may be small, there is a possibility that most stable structure is changed by surrounding environment for each nanocluster. Then, coexistence of ferromagnetic cluster and antiferromagnetic one may be realized, which can be the origin of anisotropy in ESR.

We must examine whether $0.1\mu_B$ moment is located on each molecule or the value represents the average of various moments. For this problem, it is important to clear the magnetic structure by neutron diffraction measurement. Furthermore, magnetic anisotropic energy caused by the DM interaction or the dipole-dipole interaction must be estimated by calculation.

Many problems remain unclear even if our suggestion is confirmed. It is hoped that experimental and theoretical approach is carried out for further discussion.

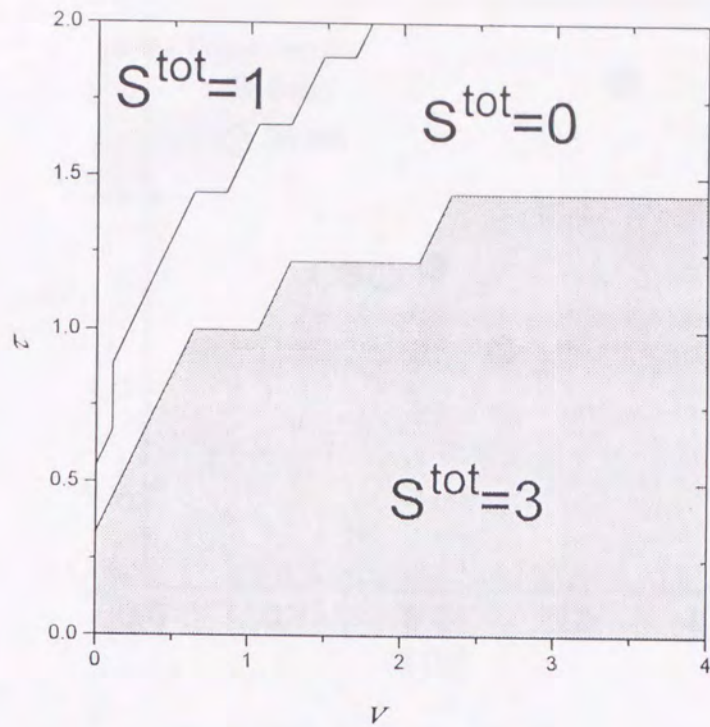


Figure 3.17: Magnetic phase diagram for one-dimensional multi-band Hubbard model with $U/J=20$ and $N=6$. τ, v represents $t/J, V/J$ respectively.

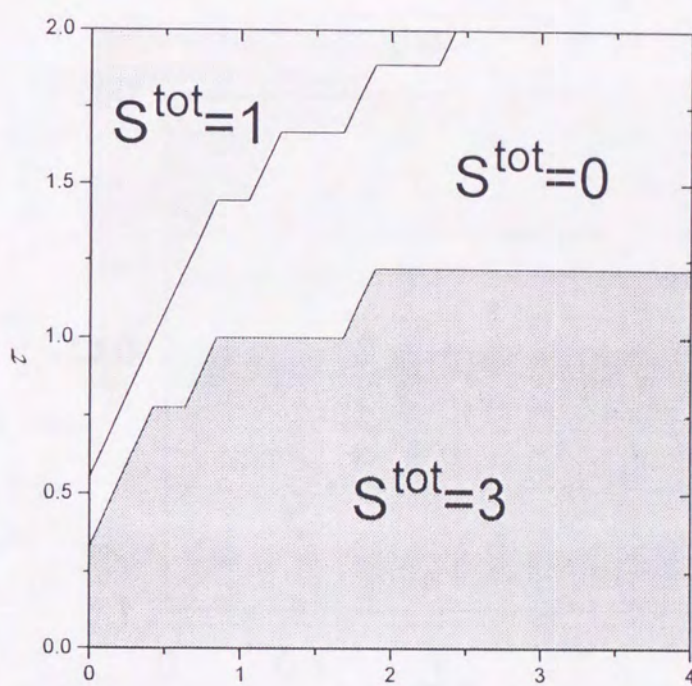


Figure 3.18: Magnetic phase diagram for one-dimensional multi-band Hubbard model with $U/J=10$ and $N=6$. τ, v represents $t/J, V/J$ respectively.

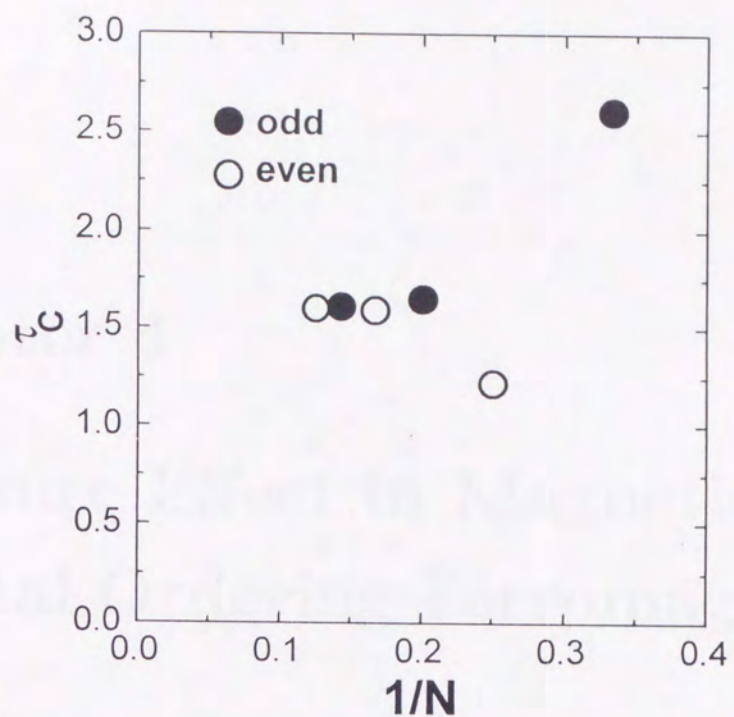


Figure 3.19: Size-dependency of τ_c which is defined as the value of transfer in occurring high spin - low spin transition with $U/J = 30$ and $V/J = 2$.

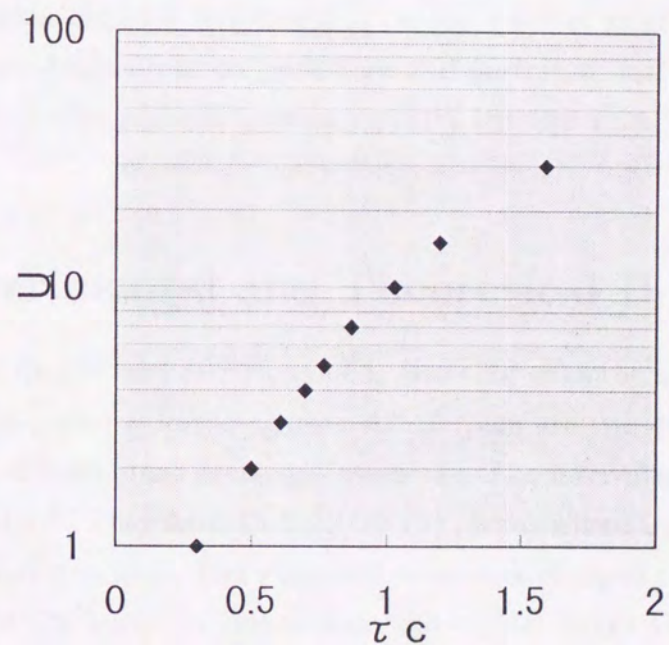


Figure 3.20: U -dependency of τ_c which is defined as the value of transfer in occurring high spin - low spin transition with $N=6$ and $V/J = 2$.

Chapter 4

Pressure Effect in Magnetism of Orbital Ordering Ferromagnet

Jahn-Teller distortion and orbital ordering play important roles in our suggestion for ferromagnetism of TDAE-C₆₀ in chapter 3. Orbital ordering plays a vital role also as the origin of intra-planer ferromagnetic interaction in layered perovskite-type magnets such as K₂CuF₄. Interesting properties of these two-dimensional materials under high pressure have been reported recently, and they seem not to be understood within the framework of simple Heisenberg models. In this chapter, we discuss the pressure effects on two-dimensional orbital ordering ferromagnets on the basis of multi-band Hubbard models with use of exact diagonalization procedure and perturbational treatment. To estimate the transfer energies for realistic systems we carry out also FLAPW band calculations for K₂CuF₄.

4.1 Experimental and Theoretical Backgrounds

M₂CuF₄ (M=K,Rb,Cs) and (RNH₃)₂CuCl₄ (R=alkil chain or aromatic group) are well known as orbital ordering ferromagnets. All of them are two-dimensional materials, in which the ratio of intra-plane exchange interaction J to inter-plane interaction J' , $|J/J'|$, is about $10^{-3} \sim 10^{-5}$. They have CuX₄(X=F,Cl) planes where Cu cation is octahedorally surrounded by halogen ions. The magnetic properties of these compounds are governed primarily by the Cu ions. In this section the crystal structure and the experimental results under ambient pressure are reviewed first, and then the role of orbital ordering is discussed briefly. Finally, properties experimentally obtained thus far under high pressure

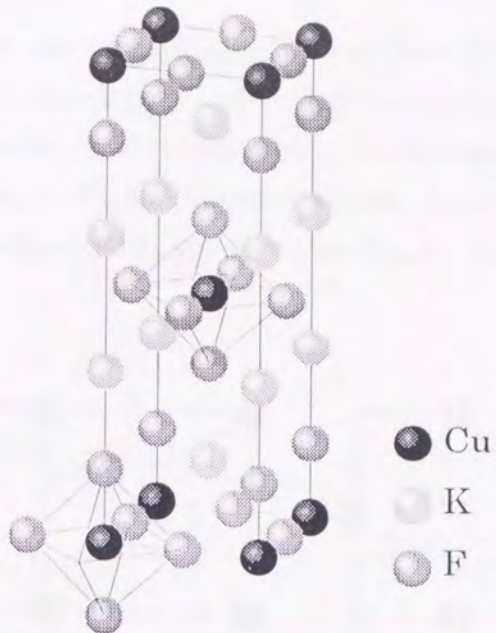


Figure 4.1: K_2NiF_4 -type crystal structure (the structure of K_2CuF_4 without Jahn-Teller distortion).

are summarized.

4.1.1 Physical properties under ambient pressure

K_2CuF_4

In 1970's much attention was paid to a layered ferromagnet K_2CuF_4 . The crystal structure of K_2CuF_4 is K_2NiF_4 -type and it consists of CuF_2 -layers and KF -layers as shown in Fig. 4.1(a). Superexchange interaction between Cu cations through F anions play the most important role in causing ferromagnetic ordering. Each Cu cation has one d -hole, which is considered to occupy the $d_{3z^2-r^2}$ orbital. Since superexchange interaction via anions through 180° path is antiferromagnetic in general, the ferromagnetic behavior of this material is quite peculiar.

For this problem, Kugel *et al* suggested a model, in which antiferrodistortive orbital ordering give rise to ferromagnetic interaction between nearest neighboring (n.n.) Cu spins [56]. Antiferrodistortive orbital ordering means the situation that $d_{z^2-x^2}$ and $d_{z^2-y^2}$ orbitals are aligned alternately for the wave function of the ground state of Cu ions in CuF_2 planes. When a Cu ion is surrounded by six halogens octahedrally, $d\gamma$ -orbitals of Cu is doubly degenerate, and then the halogen octahedron is often distorted due to Jahn-Teller effect.

Now we consider two types of alignment of the distorted octahedra in CuX₂ plane as shown in Fig. 4.3. In structure (a) which is called antiferrodistortion (AFD), distortion of the octahedra occurs in an alternating way. On the other hand, in structure (b) which is called ferrodistortion (FD), all the octahedra are distorted in the same way. The energy diagrams of the $d\gamma$ state of Cu are shown in Fig. 4.4 for both the FD and AFD cases.

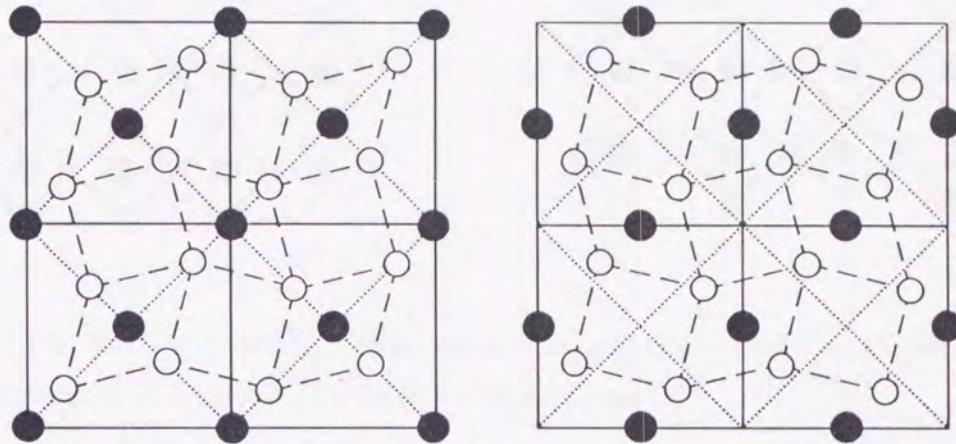


Figure 4.2: Crystal structure of K₂CuF₄(a) along ab -plane with $z=0$ (b) with $z=\frac{1}{2}c$.

Stability of the ferromagnetic state in AFD orbital ordering systems can be basically understood by perturbational treatment of charge transfer between n.n. atoms in the multi-band Hubbard model. The ferromagnetic exchange coupling J_S^{Pert} is given by

$$J_S^{\text{Pert}} = 2t^2 \left[\frac{1}{U + V - J} - \frac{1}{U + V + J} \right], \quad (4.1)$$

where t is the inter-atomic transfer energy, V the energy difference between the two orbitals on the same ion, U the intra-atomic Coulomb energy, and J the intra-atomic exchange energy.

It is noted here that the antiferromagnetic state is stabilized if the orbital ordering is FD type. Ito *et al* confirmed the orbital ordering by polarized neutron scattering measurements [58]. Furthermore, Hidaka *et al* [59] determined its crystal structure completely as shown in Fig. 4.2. According to their results F⁻ ions shift from the center between n.n. Cu²⁺ ions in CuF₂ planes so as to stabilize an orbital ordering state, i.e. an AFD order. Results of Raman scattering and NMR measurements also support the exsistence of an AFD order. Thus it is clear that the most important origin of ferromagnetic order is the orbital ordering with AFD order [61, 62].

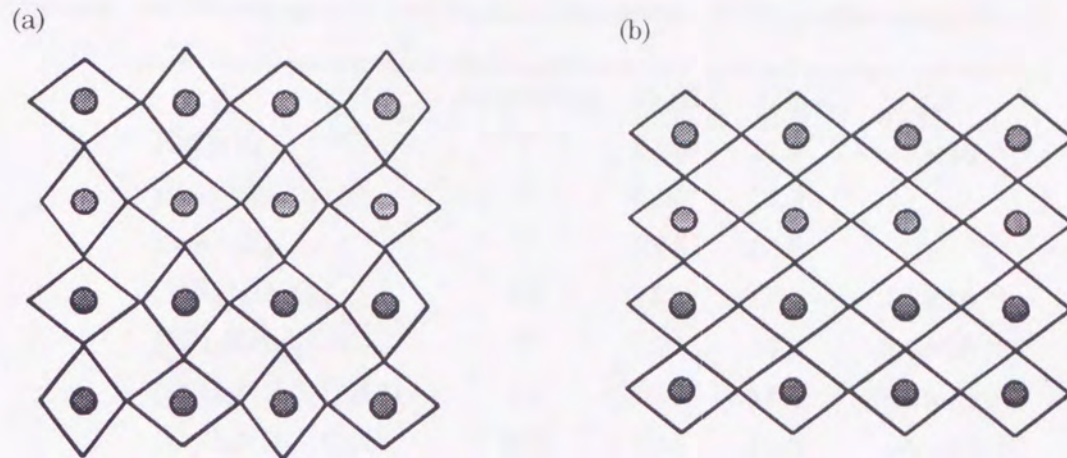


Figure 4.3: Two kinds of Jahn-Teller distortion in CuX_2 plane ($\text{X}=\text{halogen ion}$) (a) anti-ferrodistortive structure (b) ferrodistortive structure.

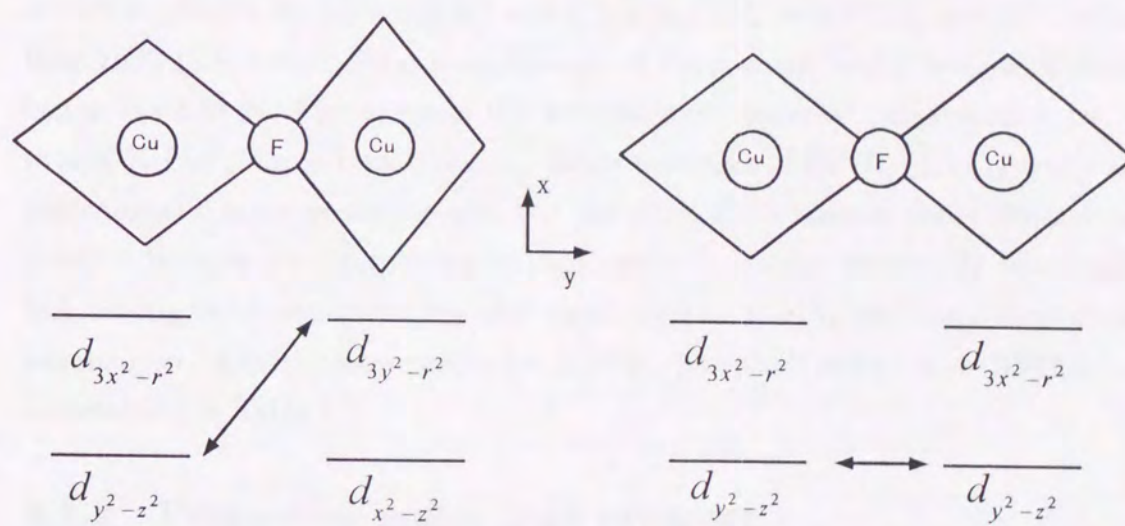


Figure 4.4: Energy diagrams and structures of interatomic transfer between a pair of nearest coppers. The transfer with the largest value is only shown for each alignment.

Table 4.1: Orbital ordering magnets with K_2NiF_4 -type crystal structure. J, J' respectively represent intraplaner and interplaner exchange interaction. F, AF, WF represent ferromagnetic, antiferromagnetic and weakferromagnetic order, respectively.[60, 68, 69, 70]

	magnetism	$T_C(K)$	$J/k(K)$	$ J'/J $
K_2CuF_4	F	6.25	11.9	$\sim 3 \times 10^{-3}$
Rb_2CuF_4	F	6.05	12.3	
Cs_2CuF_4	F	6.05	12.6	
$(NH_4)_2CuCl_4$	AF	11.2	17	3.2×10^{-3}
$(CH_3NH_3)_2CuCl_4$	F	8.91	19.2	5.5×10^{-4}
$(C_2H_5NH_3)_2CuCl_4$	AF	10.20	18.6	8.5×10^{-4}
$(C_3H_7NH_3)_2CuCl_4$	WF	7.65	16.0	$\sim 5 \times 10^{-5}$
$(C_4H_9NH_3)_2CuCl_4$	WF	7.33	15.4	$\sim 1 \times 10^{-4}$
$(C_5H_{11}NH_3)_2CuCl_4$	WF	7.30	15.9	$10^{-5} \sim 10^{-4}$
$(C_6H_{13}NH_3)_2CuCl_4$	WF	7.750	17.1	$10^{-5} \sim 10^{-4}$

$(RNH_3)_2CuCl_4$ (R = alkil chain or aromatic group)

These compounds has the crystal structure similar to K_2CuF_4 , i.e. we obtain the structure of $(RNH_3)_2CuCl_4$ by replacing K^+ and F^- of K_2CuF_4 with RNH_3 and Cl^- , respectively. EA_2CuCl_4 ($EA = C_2H_5NH_3$) is an example of these series, and it becomes a ferromagnet below $T_C=8.91$ K. The origin of the ferromagnetic order of this system is the same as that of K_2CuF_4 , i.e. orbital ordering. Other materials of $(RNH_3)_2CuCl_4$ group also show ferromagnetic order in the c -plane, but not all of them become three-dimensional ferromagnets because the interplane exchange interaction is not necessarily ferromagnetic. In fact, among the systems with R =alkyl chain, only EA_2CuCl_4 becomes a three dimensional ferromagnet. Experimental results for A_2CuF_4 (A =alkali metal) and $(RNH_3)_2CuCl_4$ are summarized in Table 4.1.

4.1.2 Properties under high pressure

Recently many experimental results of the orbital ordering ferromagnets under high pressure have been reported. Here we briefly review the experimental results for K_2CuF_4 and $(RNH_3)_2CuCl_4$.

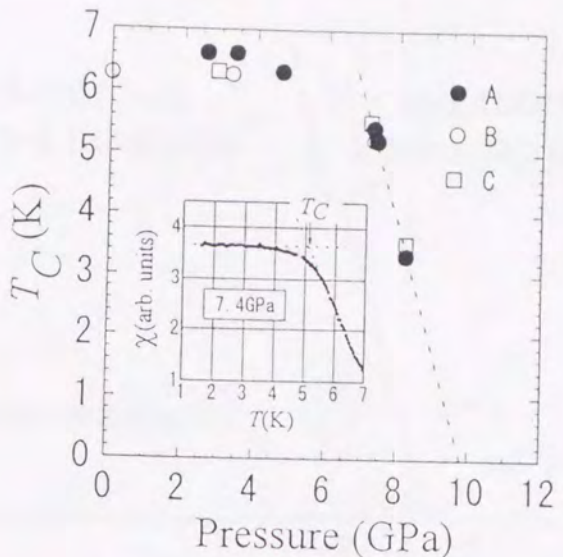


Figure 4.5: the pressure dependence of Curie temperature in K_2CuF_4 . [11]

K_2CuF_4

In 1996, Ishizuka *et al* reported a drastic change of magnetism of K_2CuF_4 under high pressures.[11] Fig. 4.5 shows the pressure dependence of Curie temperature in K_2CuF_4 . The Curie temperature is almost constant for low pressures below 4 GPa, but the magnetic susceptibility at low temperatures is suppressed rapidly above 10 Gpa. They speculated that this suppression indicates a transition from ferromagnetic to antiferromagnetic phase.

Kitazawa *et al* carried out the Raman scattering measurement at low temperatures and under high pressures, and discussed the correlation between the magnetic transition and the structural transition. They concluded that the structural transition is not the origin of disappearance of ferromagnetic state.[63] On the other hand, Terai *et al* reported that a structural transition from AFD to FD in CuX_2 planes occurs above 9 GPa at room temperature.[64] The phase diagram of the magnetic state and the crystal structure proposed tentatively is shown in Fig. 4.6. A remarkable point to be noted is that disappearance of ferromagnetic state seems to occur without any structural transitions, the reason of which is not clear at present.

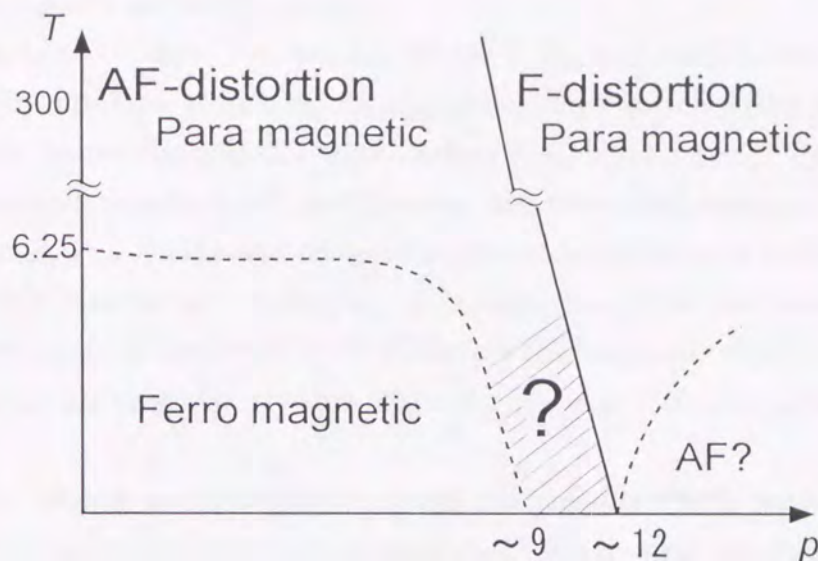
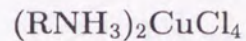


Figure 4.6: Susceptive phase diagram of temperature versus pressure for chemical and magnetic structures of K_2CuF_4



Raman scattering measurements of EA_2CuCl_4 under high pressure were carried out by Moritomo *et al* [12]. They observed disappearance of some Raman peaks above 4 GPa. Since these peaks are Raman active when Cl^- ions shift from the center between n.n. Cu^{2+} ions in CuF_2 planes (i.e. AFD order), this result suggests an extinction of AFD order above 4 GPa. The magnetic susceptibility of (*p*-cyanoanilinium) $_2\text{CuCl}_4$ was measured by Sekine *et al* below the transition pressure. They observed an enhancement of intraplane ferromagnetic interaction with increasing pressure. This behavior is quite different from that of K_2CuF_4 . Sekine *et al* pointed out the enhancement of intraplane ferromagnetic interaction may be caused by decreasing of the length between Cu and Cl with increasing pressure.

4.1.3 Basic theoretical approach and its problem

There are two possibilities for a magnetic transition from F to AF phase without accompanying a structural transition. One is the change of spin arrangement, i.e. from F to AF, in the *ab*-plane, and the other is the change of sign of interplaner exchange interaction. As shown already, the magnitude of interplane exchange interaction is very small, and hence it is quite difficult to discuss it. In this thesis we confine ourselves to discussion

about intraplaner exchange coupling.

As explained before, the stability of the F state in AFD order can be understood basically by a picture of treating the charge transfer between atoms as perturbation. We first try to discuss the pressure effects within this simple picture. By applying pressure, the interatomic transfer t will be enhanced, and the orbital energy difference V between $d_{z^2-y^2}$ and $d_{3y^2-r^2}$ is expected to decrease due to suppression of AFD. Judging from the expression of F exchange coupling eq. (4.1), enhancement of t and decrease of V not make the F state unstable but stabilize it. Therefore the results obtained in this simple picture may explain the observed pressure effects for $(p\text{-cyanoanilinium})_2\text{CuCl}_4$, but cannot for K_2CuF_4 .

In this chapter we investigate in detail the pressure effects on magnetism of orbital ordering magnets with K_2NiF_4 -type structure, first to pursue the possibility of disappearance of ferromagnetism without structural transition and secondly to clarify the origin of different pressure effects observed for each material.

4.2 Exact diagonalization approach for 1D model

At first, we apply exact diagonalization procedure to simple one-dimensional multi-band Hubbard Hamiltonian in order to survey the possibility of disappearance of ferromagnetic state without structural transition. Hamiltonian eq. (2.3) is used also here. We take into account only $d\gamma$ -orbitals of Cu, and halogen ions are considered simply as transfer path. We consider the case of AFD and the transfer energies are assumed as shown in Fig. 4.7. The transfer energy t_l between the upper and the lower orbitals is the largest, but owing to AFD the transfer energy between the lower orbitals or between the upper orbitals do not vanish and should be taken account of. For simplicity we neglect the transfer energy between the upper orbitals, and the transfer energy between the lower orbitals is denoted by t_g .

The calculation was carried out with site number $N \leq 8$ and electron number $N_e = N$, which means a quarter filled system. We performed actual calculations for various sets of t_l and t_g by fixing the values of U and V as $U/J=10$ and $V/J=2$, and determined the ground state for each set of parameters. The purpose of this calculation is to look into the change of the ground state due to pressure, i.e. due to increase of the transfer energies. As examples of our calculational results we show in Table 4.2 physical quantities such as correlation functions in the ground states determined for three sets of t_l and t_g .

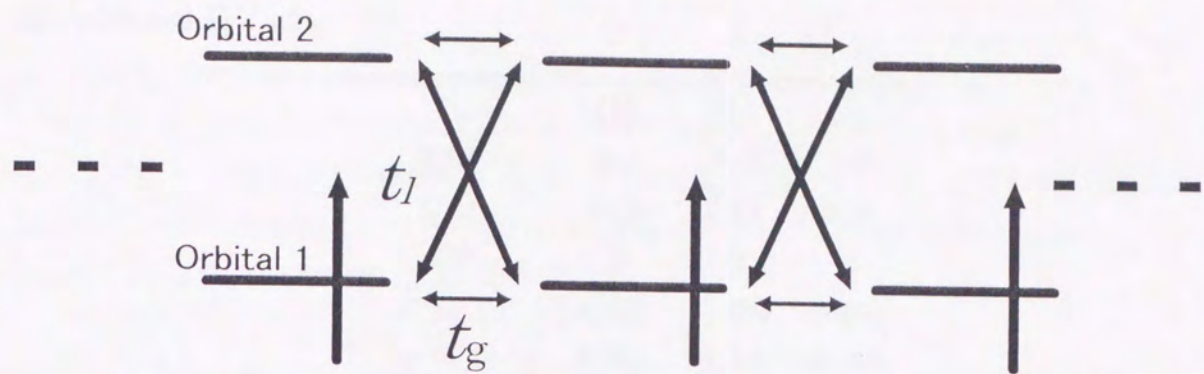


Figure 4.7: Transfer structure of calculated one-dimensional multi-band Hubbard model.

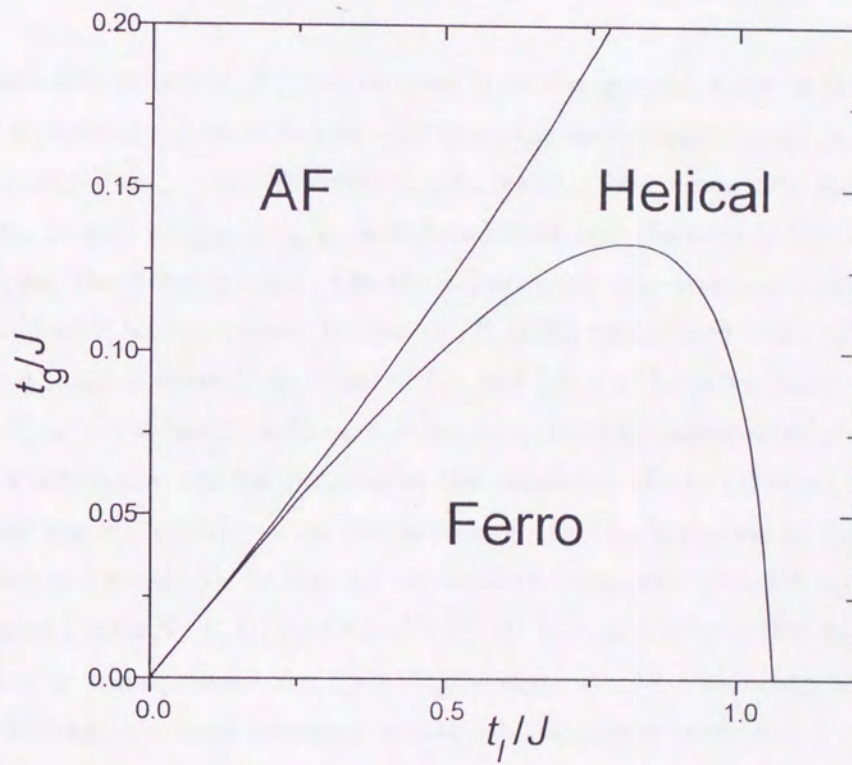


Figure 4.8: Magnetic phase diagram calculated for one-dimensional multi-band Hubbard model with $U/J=10$, $V/J=2$ and $N=6$

Table 4.2: Ground state physical properties obtained for three sets of t_l and t_g with $N=6$, $U/J=10$ and $V/J=2$

	(1)	(2)	(3)
t_l/J	0.4	0.4	1.2
t_g/J	0.04	0.12	0.04
S^{tot}	3	0	0
$\langle n_1 \rangle$	0.499	0.499	0.484
$\langle n_2 \rangle$	0.001	0.001	0.016
$\langle \delta n_1 \rangle$	0.0028	0.0024	0.031
$\langle \delta n_2 \rangle$	0.0028	0.0033	0.032
$\langle \mathbf{S}_i \cdot \mathbf{S}_{i+1} \rangle$	0.249	-0.464	0.122
$\langle \mathbf{S}_i \cdot \mathbf{S}_{i+2} \rangle$	0.249	0.204	-0.209
$\langle \mathbf{S}_i \cdot \mathbf{S}_{i+3} \rangle$	0.249	-0.226	-0.526

From the values of S^{tot} we can see that the ground state is the high spin state (F state) in case of (1) and the low spin state (or spin singlet state) in cases of (2) and (3). $\langle n_\mu \rangle$ and $\langle \delta n_\mu \rangle$ are almost the same for the three cases, and judging from the values of $\langle n_\mu \rangle$ and $\langle \delta n_\mu \rangle$ it is considered that one electron is localized on each site by occupying the lower orbital. On the other hand, the spin correlation $\langle \mathbf{S}_i \cdot \mathbf{S}_{i+\delta} \rangle$ is quite different for each case. In case of (1) (high spin state) $\langle \mathbf{S}_i \cdot \mathbf{S}_{i+\delta} \rangle$ is independent of δ and takes a value $\frac{1}{4}$. In cases of (2) and (3), on the other hand, the δ -dependence of $\langle \mathbf{S}_i \cdot \mathbf{S}_{i+\delta} \rangle$ is different with each other in spite of the same value of S^{tot} . It is difficult to make a conclusive remark because of the smallness of site number, but we may say that the spin correlation shows an antiferromagnetic-like behavior in case of (2) and helical behavior in case of (3). In Fig. 4.8 we show the magnetic phase diagram in the t_l - t_g plane determined with $N=6$, $U/J=10$ and $V/J=2$. It is clearly seen that increase of the transfer energies, t_l and t_g , make the spin singlet state stable, which suggests a possibility that the ferromagnetic state becomes unstable by applying pressure.

4.3 Band calculations with FLAPW method

In the previous section we have made discussion only for one-dimensional systems by assuming a simplified model for transfer energies. Discussion should be extended to two-dimensional systems with more realistic transfer energies to apply our theory to the real CuX₂ planes. Hence, FLAPW band calculations for K₂CuF₄ are put into practice in order to estimate the transfer energies between each pair of orbitals on neighboring Cu atoms under high pressure as well as at ambient pressure.

4.3.1 Crystal structure of K₂CuF₄

We carried out calculations for three kinds of structures of K₂CuF₄, fictitious structure without AFD order, realistic structure at ambient pressure, and possible structure under high pressure. Calculations for the fictitious structure are done in order to make clear the role of Jahn-Teller distortion for interatomic transfer and orbital energy. Band calculations for the realistic structure at ambient pressure and the fictitious one have been carried out also by Eyert *et al* with the augmented-spherical-wave (ASW) method [67]. Their results will be discussed later in comparison with our results.

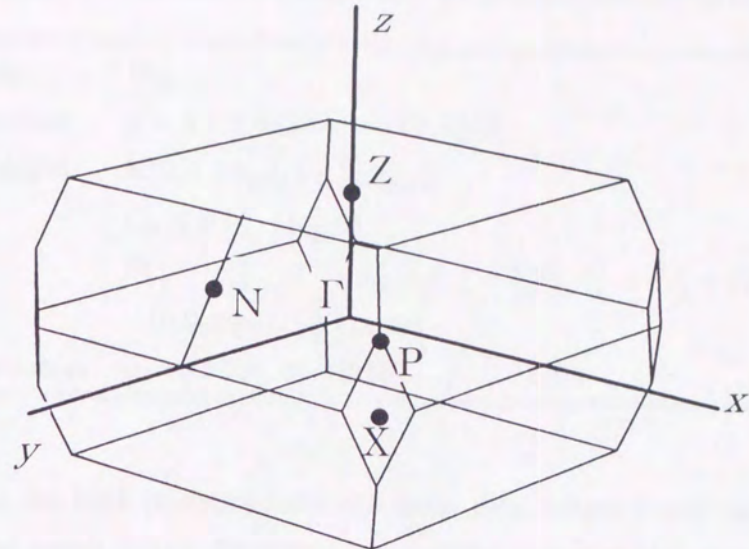
The fictitious structure and the realistic one at ambient pressure are respectively shown in Fig. 4.1 and Fig. 4.2, and their structure parameters are shown in Table 4.3 and Table 4.4. The fictitious structure is BCT (body centered tetragonal) and the realistic structure is SCO (side centered orthorhombic). The first Brillouin zone (BZ) for each structure is shown in Fig. 4.9.

In order to estimate the transfer energies under high pressure, we have performed calculations for the realistic structures with lattice constants at $p=4.2\text{GPa}$. Since the inner

Table 4.3: Structure parameters for fictitious structure of K₂CuF₄

space group	D_{4h}^{17}
lattice constant	$a = b = 4.1475\text{\AA}, c = 12.734\text{\AA}$
atomic position	K(0,0,z _K), (0,0,-z _K) Cu(0,0,0) F($\frac{1}{2}, 0, 0$), ($0, \frac{1}{2}, 0$), ($0, 0, z_F$), ($0, 0, -z_F$)
inner parameters	$z_K = 0.3568, z_F = 0.1523$

(a)



(b)

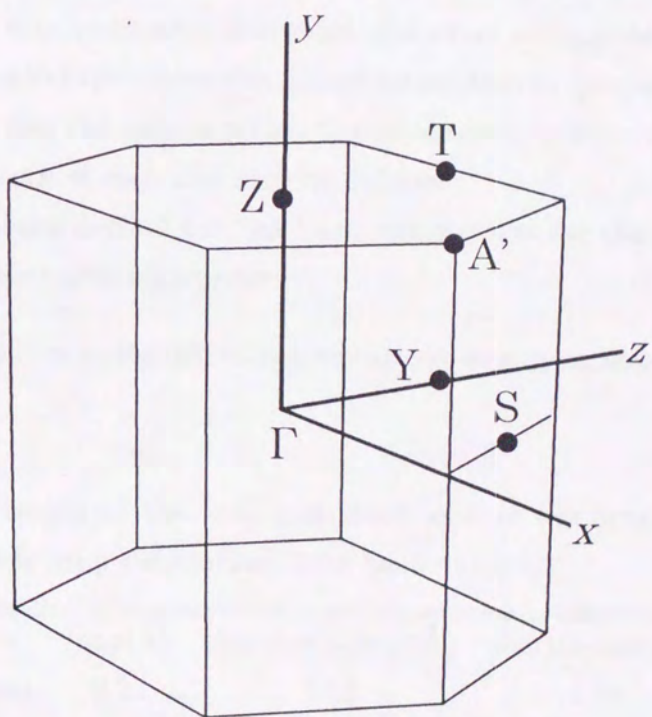


Figure 4.9: (a)First Brillouin zone of fictitious structure(BCT). (b)First Brillouin zone of realistic structure(SCO).

Table 4.4: Structure parameters for realistic structure of K_2CuF_4

space group	D_{2h}^{18}
lattice constant	$a = b = 5.8655\text{\AA}, c = 12.734\text{\AA}$
atomic position	$K(0,0,\pm z_K), (\frac{1}{2}, \frac{1}{2}, \pm z_K)$ $Cu(0,0,0), (\frac{1}{2}, \frac{1}{2}, 0)$ $F(\frac{1}{4} - \delta, \frac{1}{4} - \delta, 0), (\frac{1}{4} + \delta, \frac{3}{4} - \delta, 0), (\frac{3}{4} - \delta, \frac{1}{4} + \delta, 0), (\frac{3}{4} + \delta, \frac{3}{4} + \delta, 0)$ $(0,0,\pm z_F), (\frac{1}{2}, \frac{1}{2}, \pm z_F)$
inner parameters	$z_K = 0.3568, z_F = 0.1523, \delta = 0.01758$

parameters under high pressure have not been determined experimentally, we have considered several possibilities. First we consider the case in which the octahedral structure of F atoms is shrunk with keeping its shape. In fact, the ratio between the length of the longest axis of a octahedron and that of the other axes after structural transition into the FD structure is almost equal to that under ambient pressure. Another possibility is that the longest axis is the most shortened. Sekine *et al* suggested such a shortening may cause enhancement of interatomic exchange interaction in $(p\text{-cyanoanilinium})_2CuCl_4$. We have considered also the case in which the octahedron is distorted orthorhombically since pressure dependence of each axis may be different.

Actually we have carried out the band calculations for the following three types of possible structures under high pressure:

1. The octahedron is shrunk with keeping one-axis type anisotropy and ratio of axis length.

Table 4.5: The length of the long and short axes of the octahedron in each realistic structure for which band calculations have been done.

	long(\text{\AA})	short(<i>ab</i> -plane)(\text{\AA})	short(<i>c</i> -axis)(\text{\AA})	ratio
ambient	2.22	1.93	1.94	0.87,0.87
4.2GPa(1)	2.15	1.86	1.86	0.87
4.2GPa(2)	2.10	1.90	1.90	0.90
4.2GPa(3)	2.15	1.86	1.91	0.87,0.89

2. The long axis is more shortened with one-axis type anisotropy being kept.
3. The inner parameters are the same as those at ambient pressure, but the octahedron is distorted orthorhombically.

Table 4.5 shows the length of the long and short axes in each structure.

Table 4.6: Calculational parameters for FLAPW method. 'a' appearing in MT radius represents the length of a -axis in the realistic structure.

	fictitious	realistic
MT radius	$r_K=0.220 \times a$, $r_{Cu}=0.152 \times a$, $r_F=0.167 \times a$	
APW bases	~ 420	~ 830
$Y_{\ell m}$ for bases		$\ell \leq 3$
$Y_{\ell m}$ for potential		$\ell \leq 4$
k point for convergence	65 point in reduced zone	24 point in reduced zone
electronic configuration	K $(3p)^6(4s)^1$ Cu $(3d)^{10}(4s)^1$ F $(2s)^2(2p)^5$	

4.3.2 Results of FLAPW calculations

Calculational parameters used in our FLAPW band calculations are shown in Table 4.6. First we discuss the results of calculations for the fictitious structure. The density of state (DOS) and the partial density of state (PDOS) for each angular momentum of each atom are shown in Fig. 4.10. The states in the energy region shown in Fig. 4.10 consist mainly of $3d$ states of Cu and $2p$ states of F, and especially the main component near the Fermi energy E_F is $3d$ states of Cu. The PDOS for each component of cubic harmonics of Cu $3d$ states is shown in Fig. 4.11. It is clearly seen that the main component near E_F is not $3d\epsilon$, but $3d\gamma$. This result guarantees the validity of our model in the preceding section in which we take account of only $3d\gamma$ states of Cu. Figure 4.12 shows the energy dispersion curves along the symmetry lines in BZ. We can see in this figure that holes exist around the X point in BZ. The charge density maps of the 26th and the 27th bands at the X point are shown in Fig. 4.13. We clearly find that the ground state and the excited state for hole consist dominantly of $3d_{x^2-y^2}$ and $3d_{3z^2-r^2}$, respectively. But it is noted that

more holes exist in $3d_{3z^2-r^2}$ than $3d_{x^2-y^2}$, since an octahedron of F surrounding Cu has one-axis type anisotropy along the shortened z -axis.

Next, the results of calculations for the realistic structure at ambient pressure are presented. Figures 4.14 and 4.15 show DOS and PDOS. When the direction of Jahn-Teller distortion changes, orbital energies keep the same value but the transfer energies are affected considerably. It causes significant changes of the shape of DOS with the center of each band being unchanged. This indicates that we have to take into account the exact structure of distortion in order to discuss the physical properties of this system in a realistic way. Fig. 4.16 represents the energy dispersion, from which we see two bands crossing E_F . The main component of these bands is also $3d\gamma$ states of Cu. Figure 4.17 shows the energy dispersion calculated by Eyert *et al* [67] for K_2CuF_4 at ambient pressure, which is very different with our result. This discrepancy is considered to be coming from the difference in the potential used in respective calculation. Calculations of Eyert *et al* have been done by the ASW method with use of the muffin-tin potential whereas our calculations have been performed by the LAPW method with use of the full-potential. We believe that the results of FLAPW calculations will be reliable in estimating the energy difference between $d_{x^2-z^2}$ and $d_{3y^2-r^2}$.

DOS's calculated for the three possible structures under $p=4.2\text{GPa}$ are shown in Fig. 4.18. Their shapes are basically similar to that at ambient pressure. Especially, they have almost the same band structure near E_F . But it is seen that the band width is widened by applying pressure due to enhancement of interatomic transfer energies. In DOS of the case (2), the energy gap below E_F is narrower than the other two cases, which may be caused by decrease of the difference of orbital energy between $3d_{x^2-z^2}$ and $3d_{3y^2-r^2}$ due to shortening of the longest axis of the octahedron.

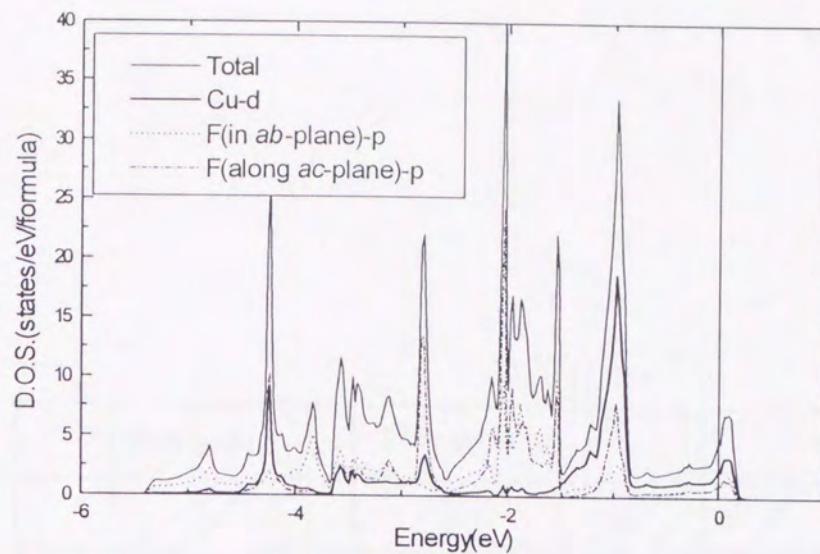


Figure 4.10: Density of state and partial density of state calculated for fictitious structure. Origin of energy represents Fermi energy.

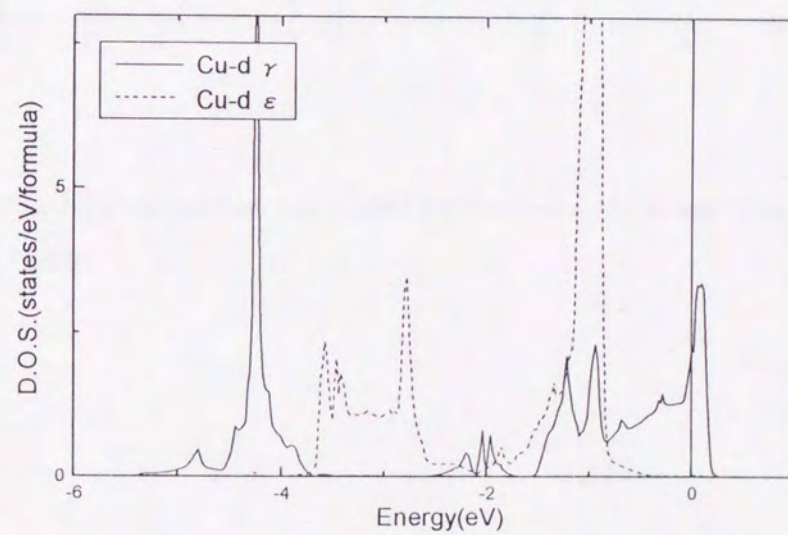


Figure 4.11: Partial DOS of cubic harmonics of Cu 3d state calculated for fictitious structure. Origin of energy represents Fermi energy.

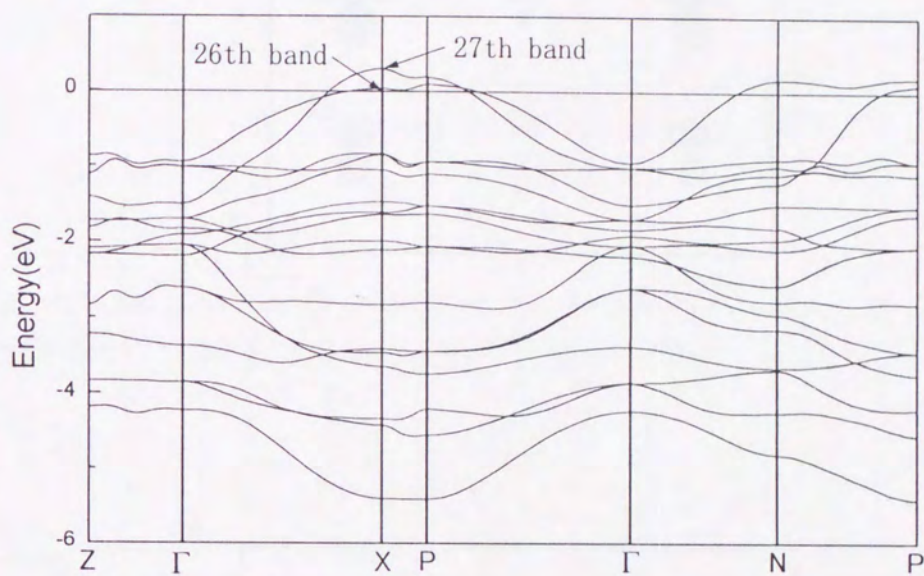


Figure 4.12: Energy dispersion calculated for fictitious structure. Origin of energy represents Fermi energy.

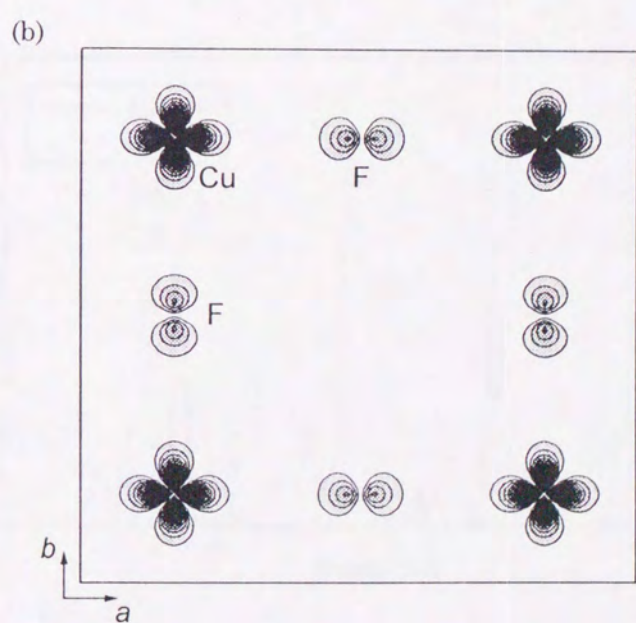
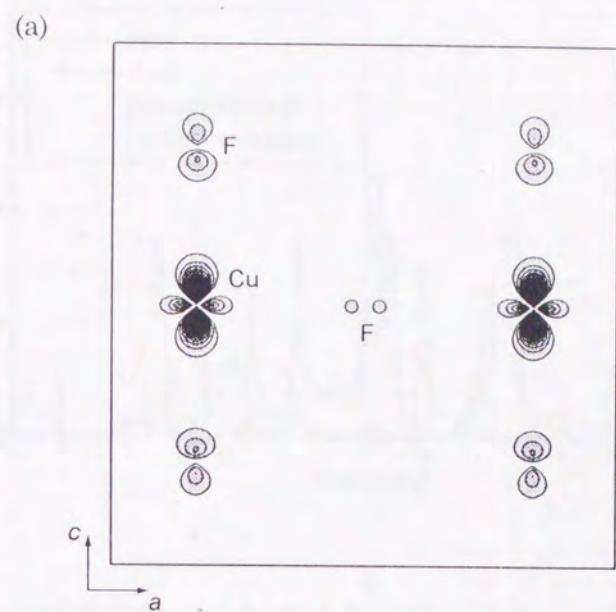


Figure 4.13: Density map calculated for fictitious structure. (a) 26th band of X point. (b) 27th band of X point.

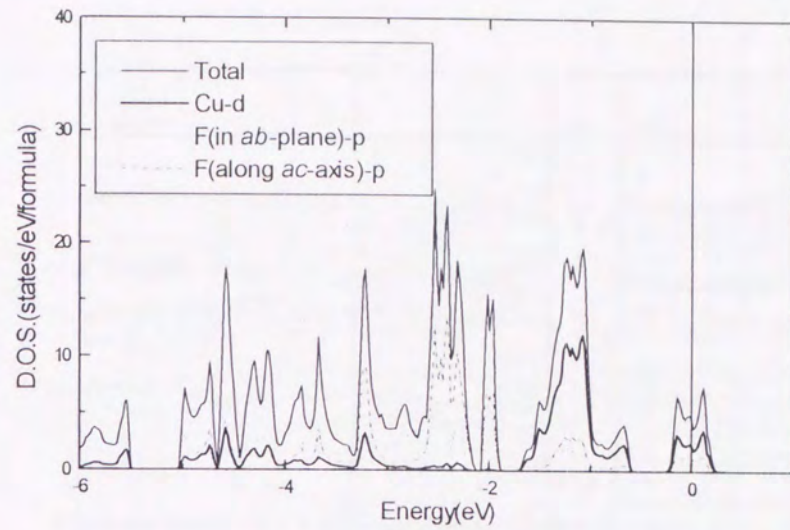


Figure 4.14: Density of state and partial density of state calculated for realistic structure under ambient pressure. Origin of energy represents Fermi energy.

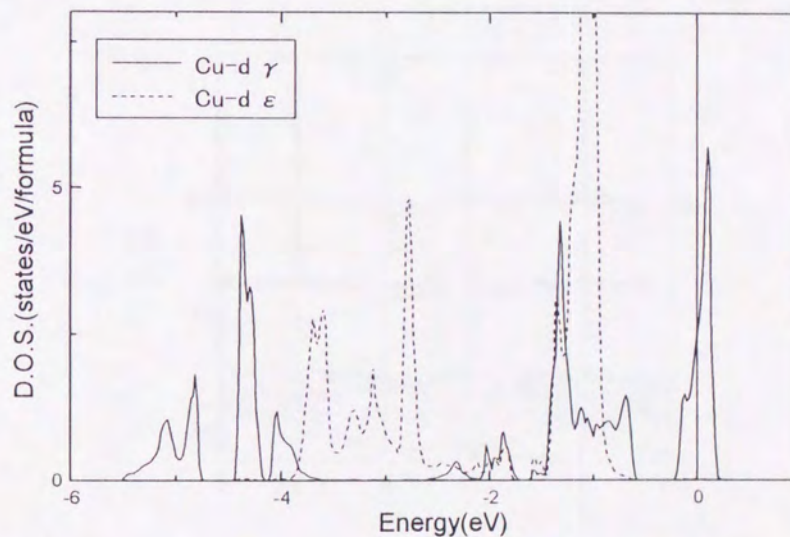


Figure 4.15: Partial DOS of cubic harmonics of Cu 3d state calculated for realistic structure under ambient pressure. Origin of energy represents Fermi energy.

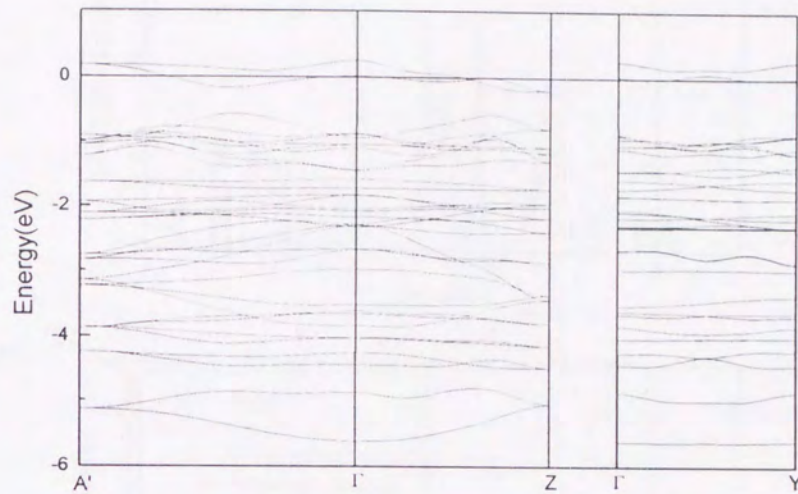


Figure 4.16: Energy dispersion calculated for realistic structure under ambient pressure. Origin of energy represents Fermi energy.

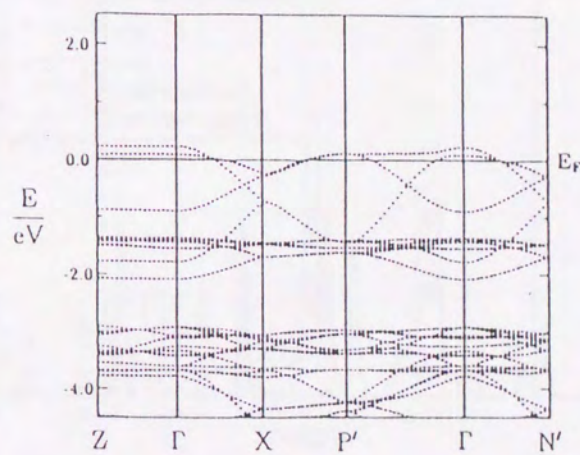


Figure 4.17: Energy dispersion calculated for realistic structure under ambient pressure by Eyert *et al* with ASW method.

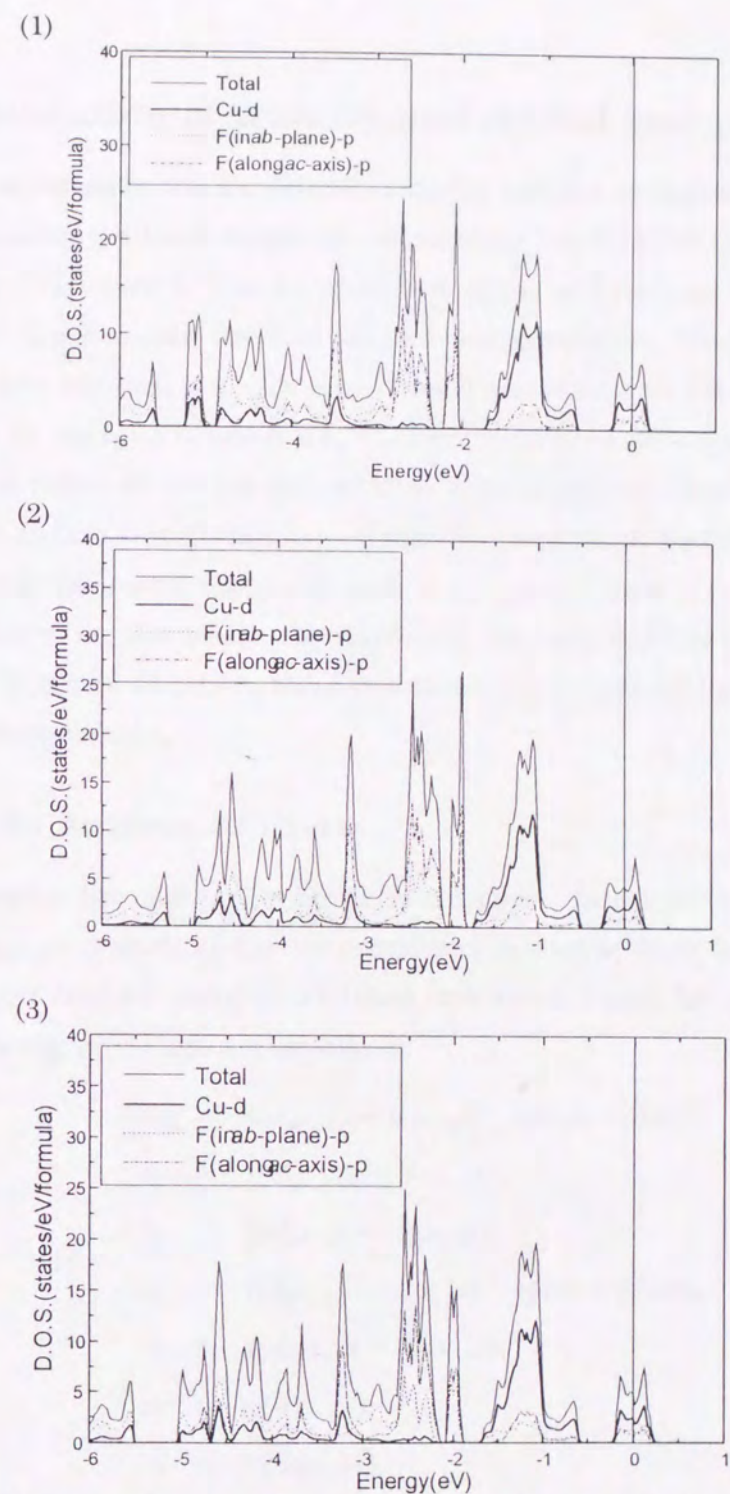


Figure 4.18: Density of state and partial density of state calculated for some structures with $p=4.2\text{GPa}$. Ochtahedron is shrunk (1) with keeping uni axial anisotropy and ratio of axis. (2) with keeping one-axis anisotropy but long axis is more shortened. (3) with keeping inner parameters under ambient pressure.

4.3.3 Estimation of transfer and orbital energies

Here we try to estimate the interatomic transfer and the orbital energies of $d\gamma$ states of Cu by reproducing the band structures obtained by the FLAPW method with use of the tight binding (TB) method. The $d\gamma$ -orbitals of copper and the p -orbitals of halogens which play a role of transfer path between Cu ions are anisotropic. Consequently interatomic transfer energies between n.n. Cu ions depend sensitively on the kind of orbital pairs. Possible transfer energies between n.n. Cu ions in AFD phase are schematically depicted in Fig. 4.20, in which we use the hole picture. Sign changing of transfer should be kept in mind in particle-hole transformation. When the octahedron surrounding a Cu cation is elongated along the y -axis, the stable state is $d_{x^2-z^2}$ and the excited state is $d_{3y^2-r^2}$, and when elongated along the x -axis, the stable and the excited states are $d_{y^2-z^2}$ and $d_{3x^2-r^2}$, respectively. In actual situation, these two states are hybridized because octahedrons are distorted orthorhombically.

Estimation for fictitious structure

First, we consider the case of the fictitious structure. In adopting the TB method only $d_{x^2-y^2}$ and $d_{3z^2-r^2}$ orbitals of Cu are considered as atomic basis functions. Intra-planer and inter-planer transfer energies are taken into account only for n.n. sites. Parameters used in the fitting procedure are as follows:

$$\begin{aligned}
 t_1 &= t(d_{x^2-y^2} - d_{x^2-y^2}) \quad \text{intra-plane}, \\
 t_2 &= t(d_{3z^2-r^2} - d_{3z^2-r^2}), \\
 t_3 &= t(d_{x^2-y^2} - d_{3z^2-r^2}), \\
 t_4 &= t(d_{x^2-y^2} - d_{x^2-y^2}) \quad \text{inter-plane}, \\
 t_5 &= t(d_{3z^2-r^2} - d_{3z^2-r^2}), \\
 v_1 &= v(d_{x^2-y^2}), \\
 v_2 &= v(d_{3z^2-r^2}).
 \end{aligned} \tag{4.2}$$

Matrix representation of the Hamiltonian for each \mathbf{k} is represented as

$$H^{\text{TB:fict}} = \begin{pmatrix} H_{11} & H_{12} \\ H_{12} & H_{22} \end{pmatrix}, \tag{4.3}$$

$$\begin{aligned}
 H_{11} &= -2t_1(\cos k_x + \cos k_y) - 8t_4 \cos \frac{1}{2}k_x \cos \frac{1}{2}k_y \cos \frac{1}{2}k_z + v_1, \\
 H_{22} &= -2t_2(\cos k_x + \cos k_y) - 8t_5 \cos \frac{1}{2}k_x \cos \frac{1}{2}k_y \cos \frac{1}{2}k_z + v_2, \\
 H_{12} &= -2t_3(\cos k_x - \cos k_y).
 \end{aligned}$$

We have found that a set of parameters shown in Table 4.7 can reproduce the band structure calculated by the FLAPW method. Figure. 4.19 shows the comparison of the energy dispersions calculated by the FLAPW and the TB method. It is seen that band structures near E_F are reproduced quite faithfully by the TB method. Inter-planer transfer energy is only about 0.01 times as large as intra-planer transfer energy, and hence this system can be regarded as good two-dimensional system, which is consistent with experimental results. Furthermore we note that each value of the transfer energy is consistent with the magnitude of the overlap between the two wave functions.

Table 4.7: A set of parameters which can reproduce the band structure calculated by the FLAPW method most faithfully (in unit of eV).

t_1	t_2	t_3	t_4	t_5	v_1-v_2
0.212	0.122	0.170	0.00	0.003	0.220

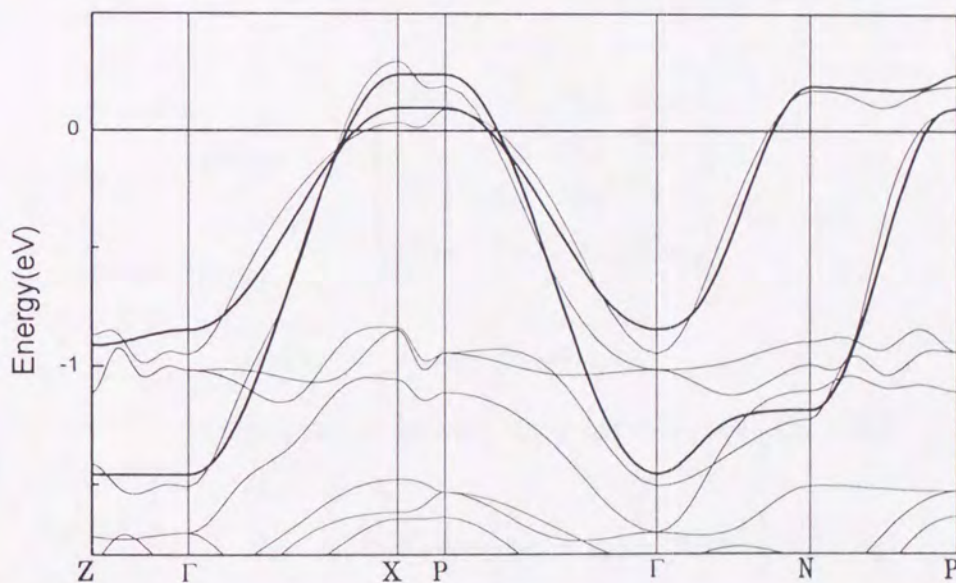


Figure 4.19: the comparison of energy dispersion calculated for fictitious structure with FLAPW method and tight binding method.

Table 4.8: Parameters used in the TB fitting for the cases of the realistic structures.

t_g	$: t(d_{3x^2-r^2}-d_{3y^2-r^2})$
t_e	$: t(d_{y^2-z^2}-d_{x^2-z^2})$
t_l	$: t(d_{3x^2-r^2}-d_{x^2-z^2})$
t_s	$: t(d_{3z^2-r^2}-d_{3z^2-r^2})$
v_g	$: v(d_{3x^2-r^2})$
v_e	$: v(d_{y^2-z^2})$

Estimation for realistic structure

Next, similar approach is applied to the realistic AFD structure. Four functions are considered as the atomic bases for the TB calculation since this system includes two Cu cations in the unit cell. For simplicity, only intraplaner transfer is considered, and we attempt to reproduce only the $k_z=0$ part of the band structures calculated by the FLAPW method.

Table 4.8 shows the transfer and the orbital energies used in the TB fitting procedure (see also Fig. 4.20).

Now, the Hamiltonian matrix in the TB method is described as

$$H^{\text{TB:real}} = \begin{pmatrix} H_{11} & 0 & H_{13} & H_{14} \\ 0 & H_{22} & H_{23} & H_{24} \\ H_{13} & H_{23} & H_{33} & 0 \\ H_{14} & H_{24} & 0 & H_{44} \end{pmatrix}, \quad (4.4)$$

$$\begin{aligned} H_{11} &= v_g, \\ H_{13} &= -4t_e \cos \frac{1}{2}k_x \cos \frac{1}{2}k_y, \\ H_{14} &= -2t_l \cos \frac{1}{2}(k_x + k_y) - 2t_s \cos \frac{1}{2}(k_x - k_y), \\ H_{22} &= v_e, \\ H_{23} &= -2t_s \cos \frac{1}{2}(k_x + k_y) - 2t_l \cos \frac{1}{2}(k_x - k_y), \\ H_{24} &= -4t_g \cos \frac{1}{2}k_x \cos \frac{1}{2}k_y, \\ H_{33} &= v_g, \\ H_{44} &= v_e. \end{aligned}$$

Table 4.9: A set of parameters which can reproduce the band structure calculated by FLAPW method most faithfully(in unit of eV)

	$v_e - v_g$	t_l	t_g	t_e	t_s
ambient	0.55	-0.28	-0.01	0.10	0.00
$p=4.2\text{GPa}$	(1)	0.58	-0.31	-0.03	0.15
	(2)	0.45	-0.29	-0.05	0.18
	(3)	0.56	-0.30	-0.03	0.16
fictitious		-0.31	-0.04	0.12	0.02

We have found that a set of parameters shown in Table 4.9 can reproduce the band structures calculated by the FLAPW method faithfully for each structure. The parameters for the fictitious structure have been derived from t_1 , t_2 and t_3 given in Table 4.7 by making use of the following relations:

$$d_{y^2-z^2} = -\frac{1}{2}d_{x^2-y^2} - \frac{\sqrt{3}}{2}d_{3z^2-r^2} \quad (4.5)$$

$$d_{x^2-z^2} = \frac{1}{2}d_{x^2-y^2} - \frac{\sqrt{3}}{2}d_{3z^2-r^2} \quad (4.6)$$

$$d_{3x^2-r^2} = \frac{\sqrt{3}}{2}d_{x^2-y^2} - \frac{1}{2}d_{3z^2-r^2} \quad (4.7)$$

$$d_{3y^2-r^2} = -\frac{\sqrt{3}}{2}d_{x^2-y^2} - \frac{1}{2}d_{3z^2-r^2} \quad (4.8)$$

It is noted here that the parameter values given in Table 4.9 should not be taken seriously because we have done TB calculations with use of limited number of atomic orbitals. Nevertheless, we believe that Table 4.9 give us important and interesting information about the pressure effects on the transfer and the orbital energies. First, the energy difference between the upper and the lower orbitals is enhanced with adding pressure except for the case (2). The decrease of the orbital energy difference in the case (2) is considered to be caused by shortening of the longest axis of the octahedron. On the other hand, the enhancement in other cases is due to the reduction of the octahedron volume, which makes the tetragonal-type crystal field larger. Secondly, all of the transfer parameters show a tendency to be enhanced by adding pressure. The degree of enhancement of t_l which has the largest value is rather small, and hence it is expected that the change of t_l due to pressure may not cause a drastic change of the magnetic properties. On the other

hand, t_g and t_s whose value is nearly 0 at ambient pressure is much enhanced by adding pressure. These two transfer energies should vanish if we consider only two octahedron clusters with AFD order. Therefore the enhancement of these transfers may be caused by increasing of the orthorhombic-type crystal field due to other CuX_2 planes, change of octahedron from AFD and hybridization in adding pressure.

Finally, we compare the results for the fictitious structure with those for the realistic structure. We find that all the parameters are enlarged in the fictitious structure. t_l and t_e may be enhanced by the shift of halogen anions toward the center of n.n. Cu cations. Increase of t_g and t_s seem to be natural because AFD order does not exist in the fictitious structure.

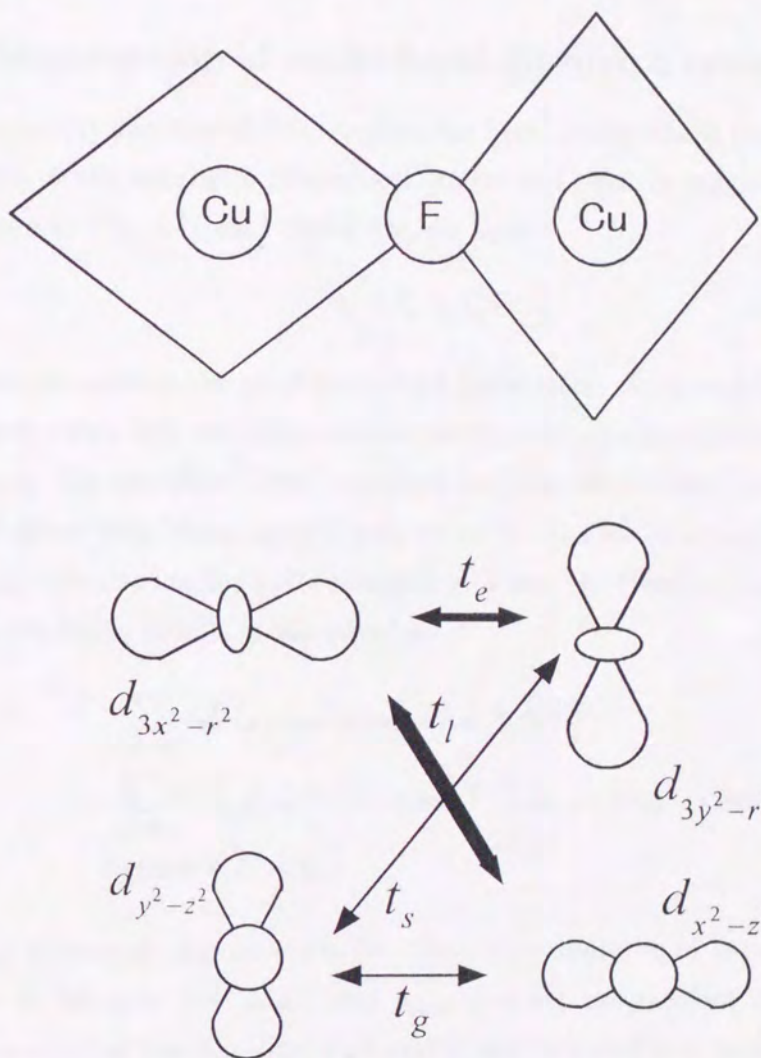


Figure 4.20: Shape of $d\gamma$ wave functions of Cu and transfer structure between a pair of nearest coppers. Thickness of arrow indicates the magnitude of each transfer.

4.4 Perturbational approach for CuX₂ plane

We have estimated the values of interatomic transfer and orbital energies for the realistic structure of K₂CuF₄ under both ambient and high pressure. With use of these values we try to make the magnetic phase diagram for CuX₂ planes in order to investigate pressure effects on orbital ordering systems. The perturbational treatment will be adopted for the interatomic transfer because we found that holes in Cu *d*_γ-orbitals keep a localized character near the ferromagnetic region.

4.4.1 Construction of multi-band Hubbard model Hamiltonian

In order to simplify the model Hamiltonian we first clarify which parameters give significant influence to the magnetic properties. As for the relative magnitudes of the transfer energies shown in Fig. 4.20 and Table 4.9, we have

$$t_l > t_e > t_g \sim t_s$$

Among these parameters the most important parameters are t_l and t_g because the former has the largest value and the latter means the transfer energy between the ground states in hole picture. On the other hand, t_e means the transfer between the excited states, and hence it will affect little the magnetic properties in the case of a quarter-filling. Therefore we neglect t_e . We also neglect t_s for simplicity. Then, the Hamiltonian for the interatomic transfers in the CuX₂ planes is described as

$$\begin{aligned} H_1 &= \sum_{xy\sigma\delta\delta'} t_g (c_{(x,y)2a\sigma}^\dagger c_{(x+\delta,y+\delta')1a\sigma} + h.c.) \\ &+ \sum_{xy\sigma\delta} t_l (c_{(x,y)1a\sigma}^\dagger c_{(x-\delta,y-\delta)2b\sigma} + c_{(x+\delta,y+1-\delta)1a\sigma}^\dagger c_{(x,y)2b\sigma} + h.c.), \end{aligned} \quad (4.9)$$

where $\delta, \delta' = 0, 1$

$c_{xy\ell\mu\sigma}^\dagger (c_{xy\ell\mu\sigma})$ represents the creation (annihilation) operator of μ -orbital with σ -spin at the ℓ -th Cu in the unit cell (x, y) , and $n_{i\ell\mu\sigma}$ denotes the number operator of the same state. It is noted that two Cu ions, $\ell=1$ and 2, are included in a unit cell, which is shown in Fig. 4.21. From now on, the terms other than H_1 , i.e. the Coulomb interaction parts in the total Hamiltonian will be denoted by H_0 .

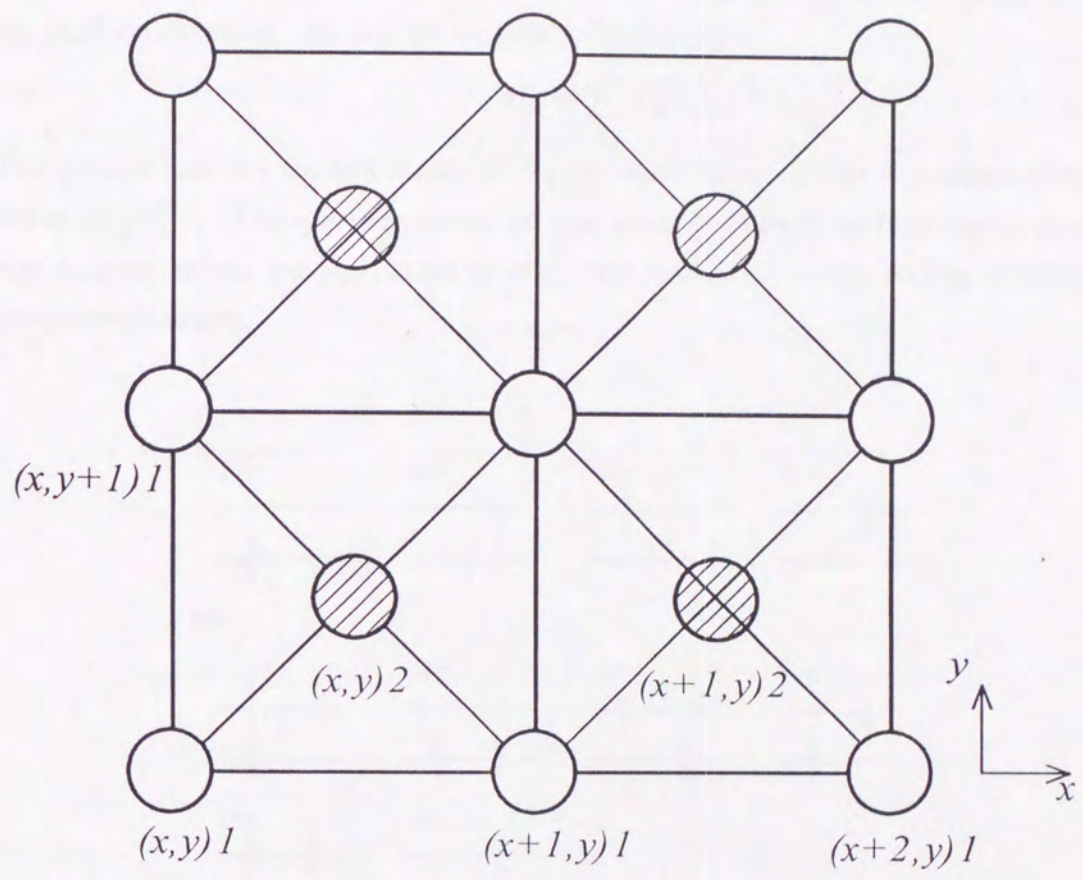


Figure 4.21: The structure of two-dimensional multi-band Hubbard model for CuX_2 plane. Thick line represents the boundary of unit cell.

4.4.2 Transformation to Heisenberg Model

It is well known that the single band Hubbard model can be transformed into a Heisenberg model with interatomic exchange energy $J_1 = -\frac{4t^2}{U}$ by perturbational approach if $U \gg t$. Similar discussion can be applied to our present model systems.

Before performing perturbational calculations, the ground and the excited states of H_0 must be obtained. H_0 can be written following form,

$$H_0 = \sum_i H_0^{(i)}. \quad (4.10)$$

The ground and the excited states of H_0 are represented as direct product of the eigenstates of $\{H_0^{(i)}\}$. One-particle states on one atom is limited by four states as shown in Fig. 4.22(a), which are eigenstate of $H_0^{(i)}$. Six states, $|1\rangle \sim |6\rangle$, in Fig. 4.24(b) are the two-particle states.

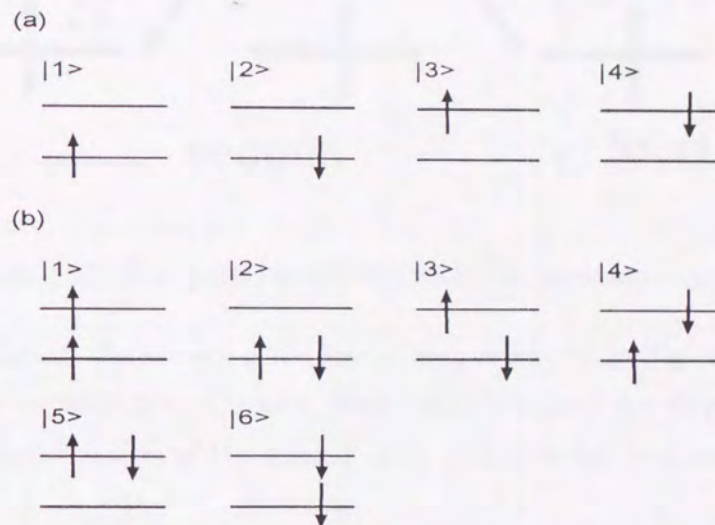


Figure 4.22: (a) many-body bases for one-site with one electron. (b) with two electrons.

In the subspace of $S_z^{\text{tot}} = 0$, the eigenstates of $H_0^{(i)}$ must be generated from $|2\rangle \sim |5\rangle$. Matrix representation of $H_0^{(i)}$ in the space of $S_z^{\text{tot}} = 0$ of the two-particle state is given by

$$H_0^{(i)} = \begin{pmatrix} U & 0 & 0 & 0 \\ 0 & U + V & -J & 0 \\ 0 & -J & U + V & 0 \\ 0 & 0 & 0 & U + 2V \end{pmatrix}. \quad (4.11)$$

In obtaining the above expression, the sign arising from anticommutation relation of fermions should be correctly taken into account. The eigenvalues and the corresponding eigenfunctions are obtained as

$$\begin{aligned} |\alpha\rangle &= |2\rangle & E = U, \\ |\beta\rangle &= \frac{1}{\sqrt{2}}(|3\rangle + |4\rangle) & E = U + V - J, \\ |\gamma\rangle &= \frac{1}{\sqrt{2}}(|3\rangle - |4\rangle) & E = U + V + J, \\ |\delta\rangle &= |5\rangle & E = U + 2V. \end{aligned} \quad (4.12)$$

Now we carry out the perturbational calculations. We perform the calculations up to the fourth order in t_l and up to the second order in t_g . Figure 4.23 represents the charge transfer paths in perturbational calculation with respect to t_l .

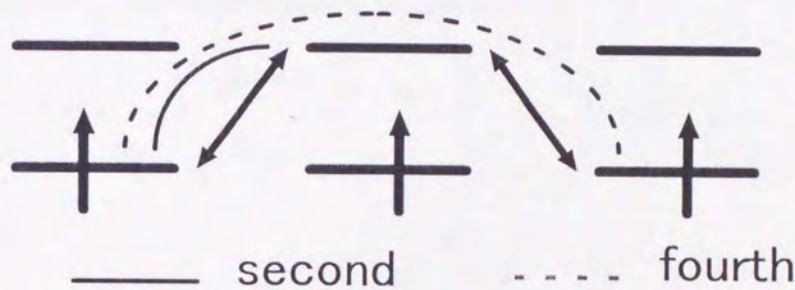


Figure 4.23: The path considered with perturbational approach for t_l

First we discuss the second order terms in t_g as shown in Fig. 4.24(a) which produces an interaction between n.n. Cu ions. Four basis functions are shown in Fig. 4.24(b) and the matrix representation of the second order perturbation is given by

$$H_1^{(t_l:2nd)} = \begin{pmatrix} -\frac{t_g^2}{U+V-J} & 0 & 0 & 0 \\ 0 & -\frac{t_l^2}{2} \left(\frac{1}{U+V-J} + \frac{1}{U+V+J} \right) & -\frac{t_l^2}{2} \left(\frac{1}{U+V-J} - \frac{1}{U+V+J} \right) & 0 \\ 0 & -\frac{t_l^2}{2} \left(\frac{1}{U+V-J} - \frac{1}{U+V+J} \right) & -\frac{t_l^2}{2} \left(\frac{1}{U+V-J} + \frac{1}{U+V+J} \right) & 0 \\ 0 & 0 & 0 & -\frac{t_l^2}{U+V-J} \end{pmatrix}. \quad (4.13)$$

Then, perturbational energies of the triplet and the singlet states are obtained as follows:

$$E_{\text{triplet}}^{(t_l:2nd)} = -\frac{t_l^2}{U+V-J} \quad (4.14)$$

$$E_{\text{singlet}}^{(t_l:2nd)} = -\frac{t_l^2}{U+V+J}. \quad (4.15)$$

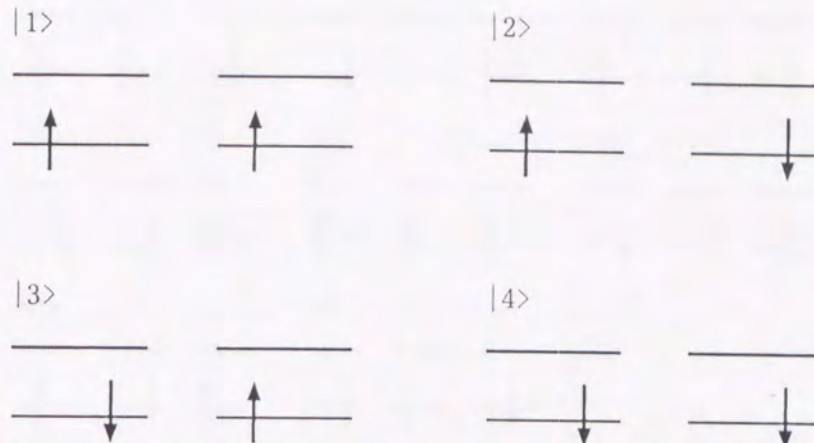


Figure 4.24: Four many-body basis functions considered in second order perturbational calculation for t_1 .

Consequently, exchange coupling is expressed as

$$J_1^{(t_1:2\text{nd})} = \frac{t_l^2}{U + V - J} - \frac{t_l^2}{U + V + J} \quad (4.16)$$

$$= \frac{2t_l^2 J}{(U + V)^2 - J^2} \quad (4.17)$$

$$\sim \frac{2t_l^2 J}{(U + V)^2} \left\{ 1 + \left(\frac{J}{U + V} \right)^2 \right\}. \quad (4.18)$$

The last expression was derived by making an expansion up to the fifth order in J and t with the assumption that J is as small as t_l .

Next we discuss the fourth order terms in t_l . The most important term of the fourth order is the interaction between the third neighbors. We shall calculate the energies of the triplet and the singlet states constituted by both edge of three spins shown in Fig. 4.25(a). Eight functions (1)~(8) shown in Fig. 4.25(b) are necessary basis functions. However, matrix elements connected with (5)~(8) are 0 from Pauli principle. Furthermore, a set of (1) and (2) has no hybridization with a set of (3) and (4), and they have the symmetric relations due to the space inversion. Consequently, we need only to solve the 2×2 secular determinant obtained from the bases (1) and (2). In this subspace, the matrix representation of the fourth order perturbation is written as

$$H_1^{(t_1:4\text{th})} = \begin{pmatrix} H_{11} & H_{12} \\ H_{12} & H_{11} \end{pmatrix} \quad (4.19)$$

$$H_{11} = -\frac{t_l^4}{U + J} \left\{ \frac{1}{(E - J)^2} + \frac{1}{4} \left(\frac{1}{E + J} + \frac{1}{E - J} \right)^2 \right\} \quad (4.20)$$

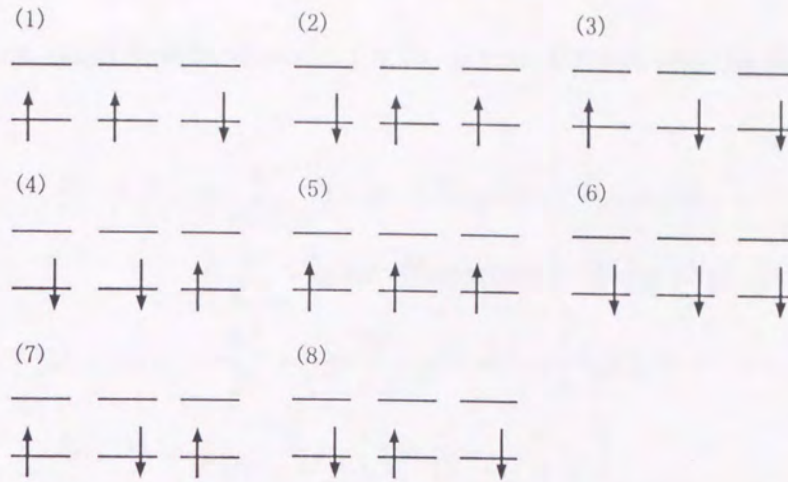


Figure 4.25: Eight many-body basis functions considered in the fourth order perturbational calculation for t_1 .

$$H_{12} = \frac{t_l^4}{U+J} \left\{ \frac{1}{E-J} \left(\frac{1}{E+J} + \frac{1}{E-J} \right) \right\}, \quad (4.21)$$

where $E = U + V$.

Further, we make an expansion up to the fifth order in J and t as done for $E^{(t_1:2nd)}$:

$$H_1^{(t_1:4th)} = \begin{pmatrix} H_{11} & -H_{11} \\ -H_{11} & H_{11} \end{pmatrix}. \quad (4.22)$$

$$H_{11} = \frac{-2t_l^4}{U(U+V)^2} \left(1 + \frac{J}{U} + \frac{J}{U+V} \right) \quad (4.23)$$

Then, energies of the triplet and the singlet states are calculated as follows:

$$E_{triplet}^{(t_1:4th)} = 0 \quad (4.24)$$

$$E_{singlet}^{(t_1:4th)} = \frac{-4t_l^4}{U(U+V)^2} \left(1 + \frac{J}{U} + \frac{J}{U+V} \right). \quad (4.25)$$

Exchange coupling between the third neighbors are represented as

$$J_2^{(t_1:4th)} = \frac{-4t_l^4}{U(U+V)^2} \left(1 + \frac{J}{U} + \frac{J}{U+V} \right). \quad (4.26)$$

Exchange coupling derived from the second order perturbation of t_g is obtained in the same way as for the single-band Hubbard model:

$$J_1^{(t_g:2nd)} = -\frac{4t_g^2}{U}. \quad (4.27)$$

Now the multi-band Hubbard model (4.10) is transformed into the following Heisenberg model:

$$H = - J_1 \sum_{\delta=-1,0} S_{(x,y)1} \cdot (S_{(x,y+\delta)2} + S_{(x+\delta,y)2}) \quad (4.28)$$

$$- J_2 \sum_{\delta=\pm 1} S_{(x,y)1} \cdot S_{(x+\delta,y+\delta)1} + S_{(x,y)2} \cdot S_{(x+\delta,y-\delta)2}, \quad (4.29)$$

$$J_1 = -\frac{4t_g^2}{U} + \frac{2t_l^2}{(U+V)^2} \left\{ 1 + \left(\frac{J}{U+J} \right)^2 \right\}, \quad (4.30)$$

$$J_2 = \frac{-4t_l^4}{U(U+V)^2} \left(1 + \frac{J}{U} + \frac{J}{U+V} \right). \quad (4.31)$$

Structure of exchange coupling is shown in Fig. 4.23.

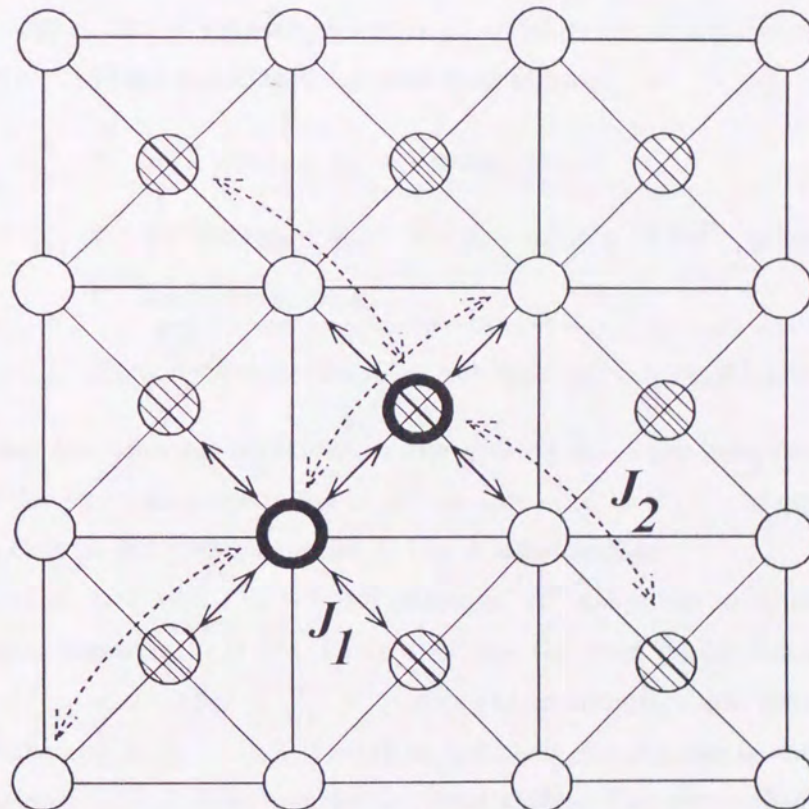


Figure 4.26: The structure of two-dimensional Heisenberg model for CuX₂ plane derived as the transformation from multi-band Hubbard model with perturbational approach

4.4.3 Phase diagram

The multi-band Hubbard model has been transformed into a Heisenberg model, for which there is a general method to determine the magnetic phase diagram if we treat the spins classically. Its basic procedure is searching the maximum eigenvalue of the matrix of Fourier-transformed exchange coupling $\hat{J}(\mathbf{q})$ (\hat{O} represents matrix).

$\hat{J}(\mathbf{q})$ is written as

$$\hat{J}(\mathbf{q}) = \begin{pmatrix} 2J_2 \cos(q_x + q_y)a & 4J_1 \cos \frac{1}{2}q_x a \cos \frac{1}{2}q_y a \\ 4J_1 \cos \frac{1}{2}q_x a \cos \frac{1}{2}q_y a & 2J_2 \cos(q_x - q_y)a \end{pmatrix} \quad (4.32)$$

$$= 2J_1 \begin{pmatrix} J \cos(q_x + q_y)a & 2 \cos \frac{1}{2}q_x a \cos \frac{1}{2}q_y a \\ 2 \cos \frac{1}{2}q_x a \cos \frac{1}{2}q_y a & J \cos(q_x - q_y)a \end{pmatrix}, \quad (4.33)$$

where $J \equiv J_2/J_1$ and a represents length of unit vector of superlattice structure. The eigenvalues of $\hat{J}(\mathbf{q})$ are calculated for each \mathbf{q} as follows:

$$\begin{aligned} E^\pm &= J_1 \{ J \cos(q_x + q_y) + J \cos(q_x - q_y) \\ &\pm \sqrt{J^2(\cos(q_x + q_y) - \cos(q_x - q_y))^2 + 16 \cos^2 \frac{1}{2}q_x \cos^2 \frac{1}{2}q_y} \}. \end{aligned} \quad (4.34)$$

$$\begin{aligned} &= 2J_1 \{ J \cos q_x \cos q_y \\ &\pm \sqrt{\frac{J^2}{4}(1 - \cos 2q_x)(1 - \cos 2q_y) + (1 + \cos q_x)(1 + \cos q_y)} \} \end{aligned} \quad (4.35)$$

To determine the spin arrangement of the ground state we have to calculate also the eigenvector for the maximum value of E^+ in case of $J_1 > 0$ (E^- in case of $J_1 < 0$). It is noted here that in the present model J_2 has a negative sign.

In case of $J_1 > 0$ and $J < -\frac{1}{2}$, for example, E^+ takes the maximum value at $(q_x = q_y = 0)$, whose eigenvector is $\frac{1}{2}(1, 1)$. In this case the most stable state is ferromagnetic.

In case of $J_1 < 0$ and $J < \frac{1}{\sqrt{2}}$, E^- takes the maximum value also at $(q_x = q_y = 0)$, but its eigenvector is $\frac{1}{\sqrt{2}}(1, -1)$. Therefore the most stable state is antiferromagnetic. In other situations, helical state may be the most stable. The phase diagram of the ground state for the effective Heisenberg model is shown in Fig. 4.27.

With use of the relations (4.30) and (4.31) and the phase diagram determined above, we can obtain the magnetic phase diagram in the plane of transfer energies t_l and t_g for the multi-band Hubbard Hamiltonian. The boundary between the helical state and

the ferromagnetic state (or the antiferromagnetic state) is given as the solution of the following equation:

$$\frac{\left(t_l^2 - \frac{b}{c}\right)^2}{\left(\frac{b}{c}\right)^2} + \frac{t_g^2}{\frac{b^2}{ac}} = 1 \quad \text{for ferro-helical} \quad (4.36)$$

$$\frac{\left(t_l^2 + \frac{b}{c}\right)^2}{\left(\frac{b}{c}\right)^2} - \frac{t_g^2}{\frac{b^2}{ac}} = 1 \quad \text{for antiferro-helical}, \quad (4.37)$$

where

$$a = \frac{4}{U}, \quad (4.38)$$

$$b = \frac{2}{(U+V)^2} \left\{ 1 + \left(\frac{J}{U+V} \right)^2 \right\}, \quad (4.39)$$

$$c = \frac{4}{U(U+V)^2} \left(1 - \frac{J}{U} + \frac{J}{U+V} \right). \quad (4.40)$$

The phase diagram in the t_l - t_g plane for K_2CuF_4 is shown in Fig. 4.28. Difference of orbital energies estimated with FLAPW calculations are used. $U=10\text{eV}$ and $J=0.8\text{eV}$ are respectively used, which are estimated experimentally for copper oxides [71, 72, 73, 74] because these values cannot be estimated with band calculations. We can see that it is similar to Fig. 4.8 which is determined for one-dimensional model. It is noted that the topological shape of diagram does not depend on given parameters. Namely, the phase diagram does not change qualitatively for different values of U, V and J .

In this figure the value of transfer estimated at ambient pressure and under 4.2GPa is shown as open and closed circles, respectively. It is found that phase transition from ferromagnetic to helical state will be impossible because t_l is too small even under high pressure. On the other hand, antiferromagnetic state may become stable under high pressure due to the enhancement of t_g . The above results indicate a possibility that layered perovskite-type orbital ordering ferromagnets shows instability against antiferromagnetic phase without structural transition by applying pressure.

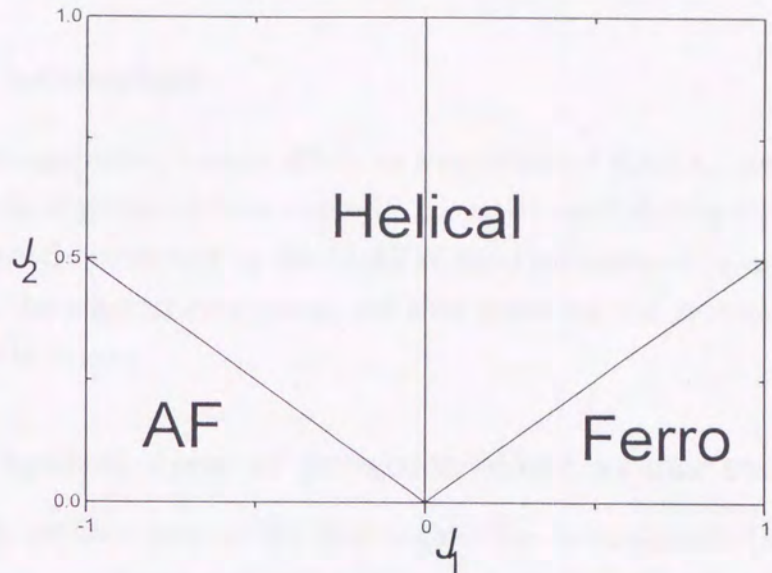


Figure 4.27: Magnetic phase diagram of Heisenberg model for CuX_2 plane with classical spin approximation.

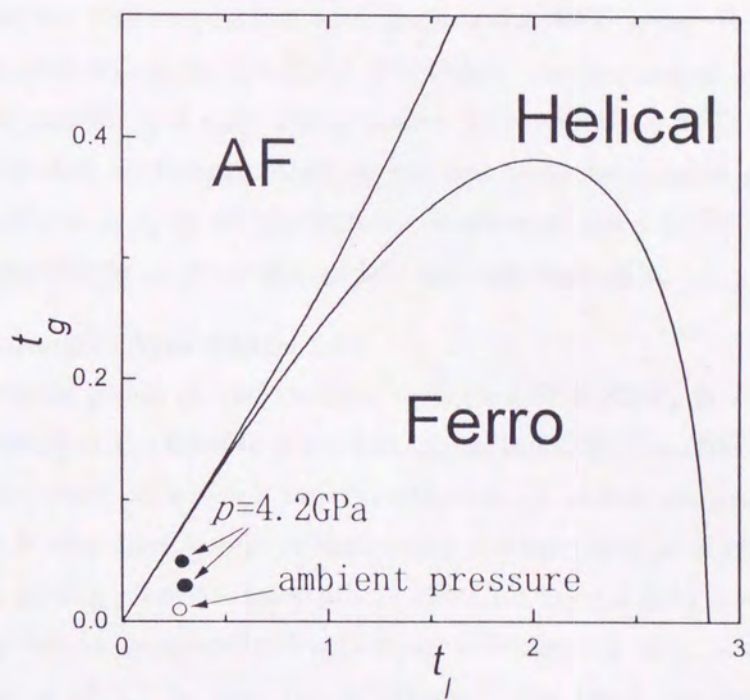


Figure 4.28: Magnetic phase diagram of two-dimensional multi-band Hubbard model derived from Fig. 4.27 with $U=10$, $J=0.8$, and $V=0.55\text{eV}$. For K_2CuF_4 , the value of U and J is assumed and V is estimated with FLAPW method.

4.5 Discussion

We have proposed that pressure effects on magnetism of K_2CuF_4 can be explained within the framework of perturbational approach for multi-band Hubbard Hamiltonian with use of the parameters estimated by the FLAPW band calculations. Here we first discuss our results from the physical view point, and then point out the problems which are open to question in the future.

4.5.1 Physical view of pressure effect in our study

In this work, we have pointed out that besides the ferromagnetic (F) state two kinds of low spin states (antiferromagnetic (AF) and helical (HI) states) can be the most stable in some parameter regions even when AFD order is realized. Judging from the pressure dependence of the transfer energies estimated from the FLAPW band calculations, pressure-induced F-HI transition seems to be impossible in K_2CuF_4 , but pressure-induced F-AF transition may be possible with keeping the AFD order. It is the increase of t_g due to pressure that will drive the F-AF transition. As mentioned in the preceding section, t_g is almost vanishing if only CuX_2 planes with complete AFD order is considered. In fact, t_g estimated for the structure at ambient pressure is quite small. But, we can find the enhancement of t_g in all the structures assumed for 4.2GPa. We here point out the following two effects as the origin of this enhancement of t_g :

- Orthorhombic-type crystal field

The space group of the realistic structure of K_2CuF_4 is D_{2h}^{18} , and hence the true symmetry at the Cu site is not tetragonal but orthorhombic. Figure. 4.29 represents a CuF_2 plane on which F ions on adjacent KF planes are projected. It is found that these F ions have a role of destroying tetragonal-type crystal field at the Cu site. With adding pressure, inter-planer effect for crystal field is enhanced. As the result, $d_{x^2-z^2}$ orbital is hybridized with other orbitals, *e.g.* $d_{3y^2-r^2}$ and d_{xz} , which increases the value of t_g . In fact, the difference of the band energies near E_F between the k -points which are equivalent in the tetragonal structure, *e.g.* (1,0,0) and (0,1,0), is 0.010 eV at ambient pressure whereas it is 0.018, 0.019 and 0.022 eV for the three types of structures under high pressure, respectively.

Table 4.10: Interatomic exchange energy between n.n. Cu ions, J_1 , and between third n.n. Cu ions, J_2 (in unit of K).

	ambient	4.2GPa(1)	4.2GPa(2)	4.2GPa(3)
J_1	12.7	11.9	2.77	10.9
J_2	-0.25	-0.38	-0.30	-0.34

- Distortion of octahedron of F ions

In the presence of AFD order, the octahedron of F ions does not have complete one axis-type anisotropy. Even at ambient pressure, the lengths of the two shorter axes are different a little. The crystal field which octahedron feels under high pressure may accelerate the distortion from the tetragonal-type structure. As the result, $d_{x^2-z^2}$ and $d_{3y^2-r^2}$ are hybridized, which makes t_g larger. Unfortunately, we can not find such a tendency from the results of the FLAPW calculations in this thesis. However, it is expected to be detectable if the accuracy of band calculations is increased.

Next, we discuss the change of interatomic exchange interaction with adding pressure. Table 4.10 shows the value of J_1 and J_2 evaluated with use of $U=10\text{eV}$, $J=0.8\text{eV}$ and the transfer and orbital energies estimated with the FLAPW calculations. J_1 at ambient pressure is consistent with the experimental value, 11.2 K [68]. It is noted, however, that this agreement should not be taken seriously because the value of J_1 depends rather sensitively on U and J and we have used simply typical values of U and J .

From Table 4.9 we find almost the same pressure dependence for $t_l(p) - t_l(0)$ and $t_g(p) - t_g(0)$ where $t_i(p)$ and $t_i(0)$ ($i = l, g$) represent the transfer energy at pressure p and at ambient pressure, respectively. By assuming $t_l(p) - t_l(0) = t_g(p) - t_g(0)$ we have calculated J_1 as a function of $t_l(p) - t_l(0)$. The results are shown in Figure 4.30. From this figure we recognize that J_1 is less dependent on pressure in a low-pressure region but drastically suppressed in a high-pressure region. This tendency of the pressure dependence of J_1 is consistent with the pressure dependence of the observed T_C of K_2CuF_4 , that is, T_C is almost constant at first with increasing pressure, but it rapidly decreases above 6 GPa. The observed small pressure dependence of T_C will be understood with this mechanism even if the origin of the pressure-induced F-AF transition is not the increase of t_g .

4.5.2 Problems

There are three problems which remain open to question.

- Calculational error

In the present study FLAPW band calculations with LDA and TB calculations have been applied to estimation of transfer and orbital energies. The first problem is the validity of the LDA band calculations for K_2CuF_4 which may be regarded as Mott (or charge transfer) insulator. Our opinion for this question is that the LDA band calculations make some sense in evaluating the one-particle energy such as the transfer energy even for strongly correlated electron systems. The second problem is the calculational errors inherent in our band calculations. Since we have adopted rather simplified TB picture we expect the maximum errors will be a few hundredth eV. In order to give more quantitative discussion it will be necessary to take account of the halogen p -orbitals as well as the Cu $d\epsilon$ in the TB band calculations.

- Reinvestigation of interplaner interaction

In this thesis, interplaner interaction is considered only in FLAPW band calculations, and the discussion about the magnetism is confined to the two-dimensional CuF_2 plane. It is reported that interplaner magnetic interaction is much depend on small change of the alignment of interplaner atoms [75]. Since the interplaner interaction is very small, it will be quite difficult to make quantitative discussion on it. But, investigation of the interplaner interaction is inevitable to discuss bulk three-dimensional magnetic behaviors.

- Magnetic properties of K_2NiF_4 -type orbital-ordering magnets other than K_2CuF_4

The results derived in this thesis are consistent with the pressure effects observed in K_2CuF_4 . On the other hand, enhancement of interatomic exchange interaction due to pressure reported for $(p\text{-cyanoanilinium})_2CuCl_4$ cannot be explained within our present study. Extension of our theory will be necessary to cover the other K_2NiF_4 -type orbital-ordering magnets.

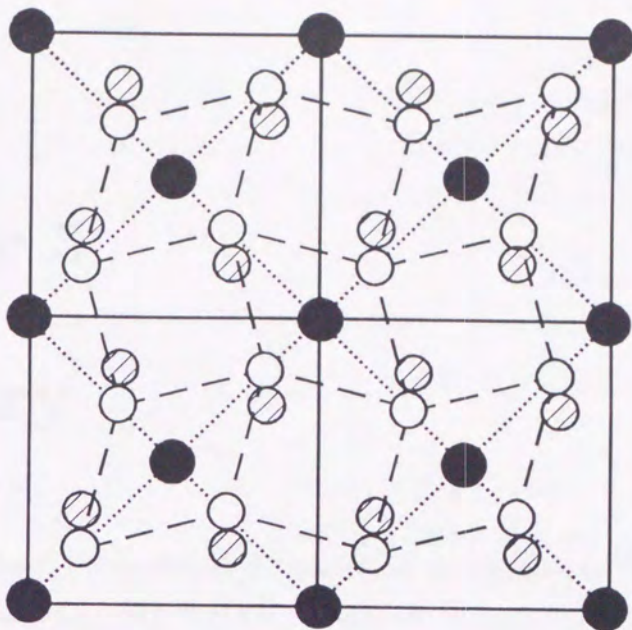


Figure 4.29: *ab*-plane of K_2CuF_4 with projecting halogen ion on other planes. square represents projected halogens, which produce the orthorhombic-type crystal field at coppers' position.

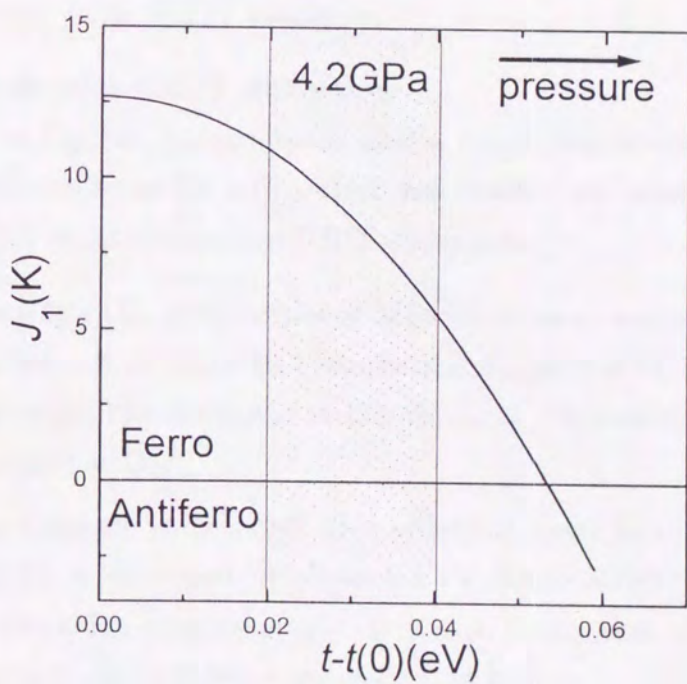


Figure 4.30: J_1 versus enhancement of transfer by pressure with assuming that pressure dependence of t_l and t_g are equal.

Chapter 5

Summary

In this thesis we have made detailed theoretical study on two kinds of orbital ordering ferromagnets: TDAE-C₆₀ and K₂CuF₄. Here we summarize the main results obtained from the present study.

The origin of ferromagnetism of TDAE-C₆₀

We suggest that the origin of ferromagnetism TDAE-C₆₀ is the orbital ordering due to intramolecular charge transfer induced Jahn-Teller (CTJT) distortion and intermolecular cooperative Jahn-Teller (CJT) distortion.

1. Intramolecular CTJT distortion

LUMO of C₆₀ has t_{1u} symmetry and is triply degenerate. Therefore Jahn-Teller distortion can occur for a C₆₀⁻ which has received one-charge from other molecules. It is called as intramolecular CTJT distortion.

- For single C₆₀⁻, semi-empirical MO calculations and structure optimization are carried out in order to evaluate the magnitude of Jahn-Teller as well as to determine the electronic structure of C₆₀⁻. Symmetry of the distorted C₆₀⁻ is assumed as D_{2h}.
- C₆₀ molecule is distorted from spherical shape into rugby ball-like structure. LUMO is separated by about 0.1 eV above SOMO although the magnitude of distortion is quite small. It is also found that the charge density of the unpaired electron has a shape like the belt.

2. Intermolecular CJT distortion

Since intermolecular transfer interaction between two orthogonal LUMO's is vanish-

ing, the magnetic interaction depends sensitively on the relative orientation of the molecular axis of the two C_{60}^- anions. Ferromagnetic ordering can be possible in C_{60}^- crystals if C_{60}^- anions are arranged so that appropriate orbital ordering is realized, which is called CJT distortion.

- In order to examine the actual possibility of the ferromagnetic order in C_{60}^- systems the magnetic phase diagram for one-dimensional multi-band Hubbard model relevant to a C_{60}^- chain is constructed with exact diagonalization procedure.
- The values of Hamiltonian parameters are evaluated semi-quantitatively from semi-empirical MO calculation and CI interaction calculation for C_{60}^- . It is found that the high spin state (ferromagnetic state) can be certainly the ground state for the parameters derived C_{60}^- .
- We have proposed possible three-dimensional arrangements of distorted C_{60}^- ions which can give rise to three-dimensional ferromagnetic order.

We also propose the following experimental approaches which might be able to confirm our suggestion.

1. Measurement of spin density map by neutron diffraction
2. Detection of molecular distortion by X-ray diffraction
3. Analysis of crystal and molecular symmetry by Raman scattering

Pressure effect of Perovskite-type orbital ordering ferromagnets

We have studied the pressure effects on Perovskite-type orbital ordering ferromagnets such as K_2CuF_4 on the basis of multi-band Hubbard model. The transfer and orbital energies in the model Hamiltonian are estimated from FLAPW band calculations for K_2CuF_4 .

1. Phase diagram of one-dimensional multi-band Hubbard Hamiltonian

We first constructed the magnetic phase diagram of simple one-dimensional multi-band Hubbard Hamiltonian with exact diagonalization procedure. The parameters in the model Hamiltonian are chosen in keeping in mind the CuF_2 plane in an orbital ordering ferromagnet K_2CuF_4 . As the result, we found that antiferromagnetic (AF) and helical (HI) states can be stable with increasing interatomic transfer energy.

2. Estimation of transfer and orbital energy of K_2CuF_4

In order to make realistic discussion for K_2CuF_4 the transfer and the orbital energies of this system have been estimated from band calculations. At first first-principle FLAPW band calculations were carried out for the structure at ambient pressure and that under high pressure, and then the parameters are estimated by reproducing the band structure of FLAPW calculation on the basis of the tight binding method with considering only the $d\gamma$ orbital of Cu ions. We found pressure dependence of t_l (transfer between the upper and the lower orbitals) and that of t_g (transfer between the lower orbitals) are almost the same.

3. Magnetic phase diagram of two-dimensional system

Two dimensional multi-band Hubbard Hamiltonian representing the CuF_2 plane which play a important role of ferromagnetism of K_2CuF_4 are constructed and converted into the Heisenberg Hamiltonian with perturbational procedure. Magnetic phase diagram for the Heisenberg Hamiltonian is derived with classical approach. As in the one-dimensional system AF and HI states can be the most stable when appropriate transfer parameters are chosen. Stability of the AF and the HI states depend on the magnitude of t_g and t_l . We point out a possibility that the pressure -induced F-AF transition may be realized in K_2CuF_4 without structural transition from AFD to FD phase. Further we can explain qualitatively the pressure dependence of T_C of K_2CuF_4 .

As discussed in this thesis, lattice distortion often has much to do with the properties in multi-band systems. For both materials, TDAE-C₆₀ and K_2CuF_4 , we have obtained new information about the relation between the ferromagnetism and lattice distortion. In order to confirm our proposal and prediction further experimental studies are desired.

Bibliography

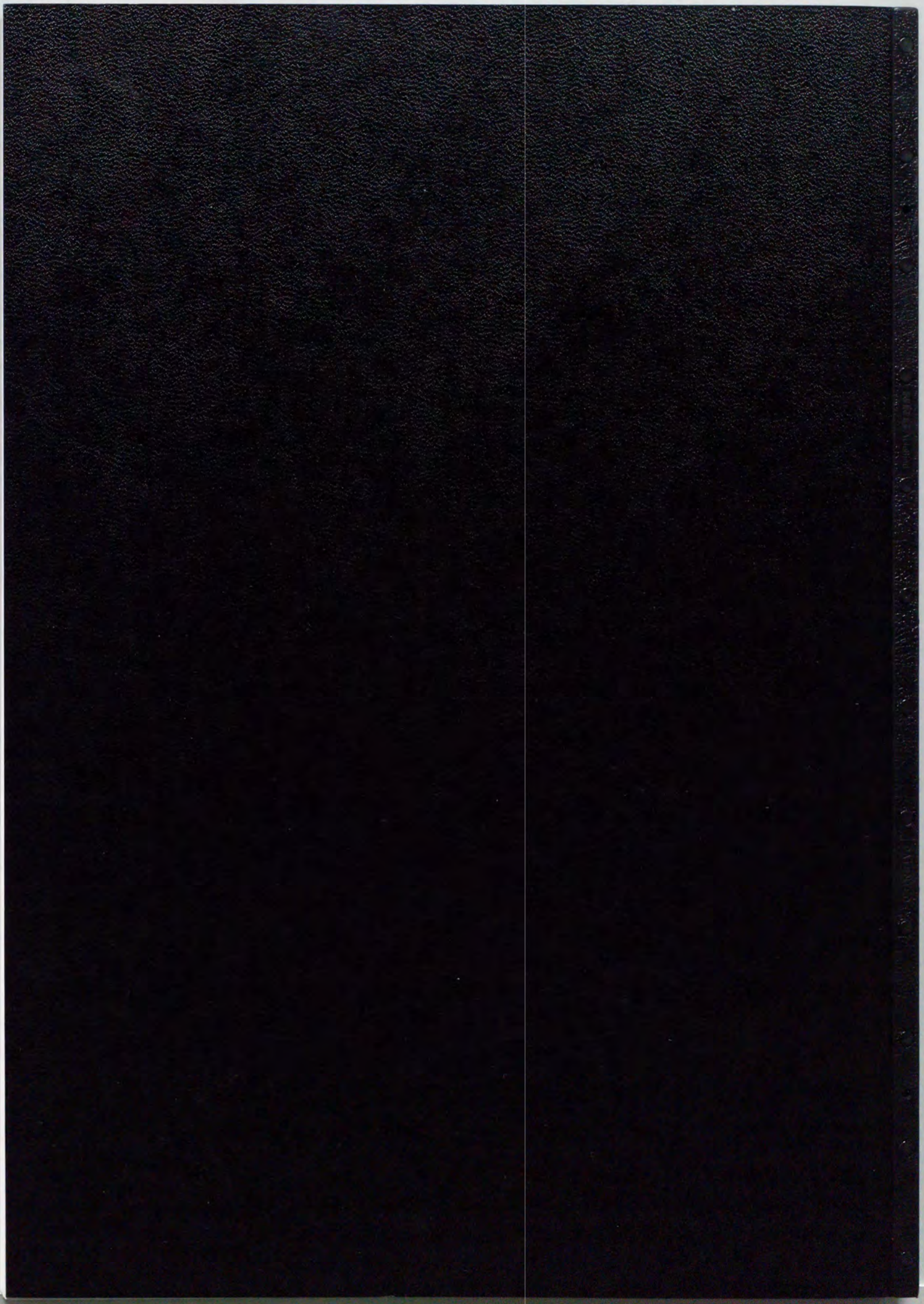
- [1] M. Kinoshita, P. Turek, M. Tamura, K. Nozawa, D. Shimoi, M. Nakazawa, M. Ishikawa, M. Takahashi, K. Awaga, T. Inabe and Y. Maruyama, *Chem. Phys. Lett.* **1225**(1991)
- [2] R. C. Haddon, A. F. Hebard, M. J. Rosseinsky, D. W. Murphy, S. J. Duclos, K. B. Lyons, B. Mileer, J. M. Rosamilla, R. M. Fleming, A. R. Kortan, S. H. Glarum, A. V. Makhija, A. J. Muller, R. H. Eick, S. M. Zahurak, R. Tycko, G. Dabbagh and F. A. Tiel, *Nature*, **350** 320 (1991)
- [3] Q. Zhu, D. E. Cox and J. E. Fischer, *Phys. Rev.* **B51** 3966 (1995)
- [4] G. Oslanyi, G. Bortel, G. Faigel, M. Tegze, L. Granasy, S. Pekker, P. W. Stephens, G. Bendele, R. Dinnebier, G. Mihaly, A. Janossy, O. Chauvet and L. Forro, *Phys. Rev.* **B51** 12228 (1995)
- [5] P. -M. Allemand, K. C. Koch, F. Wudl, K. Holczer, S. Denovan, G. Gruner & J. D. Thompson, *Science* **253** 301 (1991)
- [6] C. Zener, *Phys. Rev.* **82** 403 (1951)
- [7] P. W. Anderson and H. Hasegawa, *Phys. Rev.* **100** 675 (1955)
- [8] P. -G. de Gennes, *Phys. Rev.* **118** 141 (1960)
- [9] A. J. Millis, P. B. Littlewood and B. I. Shraiman, *Phys. Rev. Lett.* **74** 5144 (1995)
- [10] Y. Tomioka, A. Asamitu, Y. Moritomo, H. Kuwahara and Y. Tokura, *Phys. Rev. Lett.* **74** 5108 (1995)
- [11] M. Ishizuka, I. Yamada, K. Amaya and S. Endo J. Phys. Soc. Jpn **65** 1927 (1996)
- [12] Y. Moritomo and Y. Tokura, *J. Chem. Phys.* **101** 1763 (1994)

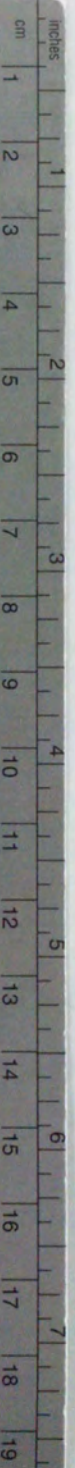
- [13] P.Hohenberg and W.Kohn,Phys.Rev.**136**(1964)B864
- [14] W.Kohn and L.J.Sham,Phys.Rev.**140**(1965)A1133
- [15] O.Gunnarsson and B.I.Lundqvist,Phys.Rev.B**13**(1976)4274
- [16] T. L. Loucks *Augmented Plane Wave Method*,W. A. Benjamin,inc., New York (1967)
- [17] T. Takeda and J. Kubler, *J. Phys.* **F9** 661 (1979)
- [18] M. Weinert, *J. Math. Phys.* **22** 2433 (1981)
- [19] E. Wimmer, H. Krakauer, M. Weinert and A. J. Freeman, *Phys. Rev.* **B24** 864 (1981)
- [20] M. Weinert, E. Wimmer and A. J. Freeman, *Phys. Rev.* **B26** 4571 (1982)
- [21] J. J. P. Stewart, *J. Comp. Chem.* **10** 221 (1989)
- [22] MOPAC Ver. 6.0 , J. J. Stewart, QCPE #455 ; Revised as Ver. 6.01 by K. Nishida, Fujitsu Corp., For Sun SPARC, JCPE P049; Revised as Ver. 6.02 by present author
- [23] J. Hubbard, *Proc. Roy. Soc.* **A276** 238 (1963)
- [24] J. Hubbard, *Proc. Roy. Soc.* **A281** 401 (1964)
- [25] M. C. Gutzwiller, *Phys. Rev.* **A134** 923 (1964)
- [26] L. M. Roth, *Phys. Rev.* **149** 306 (1966)
- [27] S. Inagaki and R. Kubo, *Int. J. Magn.* **4** 139 (1973)
- [28] K. Kusakabe and H. Aoki, *Physica* **B 194-196** 217 (1994)
- [29] A. Suzuki , T. Suzuki , R. J. Whitehead & Y. Maruyama , *Chem. Phys. Lett.* **223** 517 (1994)
- [30] K. Tanaka, A. A. Zakhidov, K. Yoshizawa, K. Okahara, T. Yamabe, K. Yakushi, K. Kikuchi, H. Suzuki, I. Ikemoto & Y. Achiba, *Phys. Rev.* **B47** 7554 (1993)
- [31] R. Blinc, J. Dolinsek, D. Arcon, D. Mihailovic & P. Venturini, *Solid State Commun.* **89** 487 (1994)

- [32] P. Venturini, D. Mihailovic, R. Blinc, P. Cevc, J. Dolinsek, D. Abramic, B. Zalar, H. Oshio, P.-M. Allemand, A. Hirsch & F. Wudl, *Int. J. Mod. Phys* **B6** 3947 (1992)
- [33] R. Blinc, P. Cevc, D. Arcon, D. Mihailovic and P. Venturini, *Phys. Rev.* **B50** 13051 (1994)
- [34] M. Tokumoto and Y. S. Song *Solid State Commun.* **97** 349 (1996)
- [35] A. Lappas, K. Prassides, K. Vavekis, D. Arcon, R. Blinc, P. Cevc, A. Amato, R. Feyerherm, F.N. Gygax & A. Schenck, *Science* **267** 1799 (1995)
- [36] D. Mihailovic, D. Arcon, P. Venturini, R. Blinc, A. Omerzu & P. Cevc, *Science* **268** 400 (1995)
- [37] V. N. Denisov, A. A. Zakhidov, G. Ruani, R. Zamponi, C. Taliani, K. Tanaka, K. Yoshizawa, T. Okahara, T. Yamabe & Y. Achiba, *Synth. Met.* **55-57** 3050 (1993)
- [38] A. Schilder, H. Klos, I. Rystau, W. Schütz & B. Gotschy, *Phys. Rev. Lett.* **73** 1299 (1994)
- [39] F. Bommeli , L. Degiorgi , P. Wachter , D. Mihailovic, A. Hassanien, P. Venturini, M. Schreiber & F. Diederich, *Phys. Rev.* **B51** 1366 (1995)
- [40] P. Cevc, R. Blinc, V. Eržen, D. Arčon, B. Zalar, D. Mihailovič & P. Venturini, *Solid State Commun.* **90** 543 (1994)
- [41] B. Gotschy, *Phys. Rev.* **B52** 7378 (1995)
- [42] W. E. Pickett, *Solid State Phys.* **48** 225 (1994)
- [43] C.M. Loeber and Z. Zhang *Solid State Phys.* **48** 349 (1994)
- [44] E. Osawa, *Kagaku* **25** 854 (1970) (*in Japanese*)
- [45] H. W. Kroto, J. R. Heath, S. C. O'Brien, R. F. Curl and R. E. Smalley, *Nature* **318** 162 (1985)
- [46] W. Kratschmer, L. D. Lamb, K. Fostiropoulos and D. R. Huffman, *Nature* **347** 354 (1990)
- [47] R. Saito, G. Dresselhaus and M. S. Dresselhaus, *Chem. Phys. Lett.* **210** 159 (1993)

- [48] N. Koga & K. Morokuma, *Chem. Phys. Lett.* **196** 191 (1992)
- [49] P. W. Stephens, D. Cox, J. W. Lauher, L. Mihaly, J. B. Wiley, P.-M. Allemand, A. Hirsch, K. Holczer, Q. Li, J. D. Thompson & F. Wudl, *Nature* **355** 331 (1992)
- [50] R. Blinc, K. Pokhodnia, P. Cevc, D. Arčon, A. Omerzu, D. Mihailović, P. Venturini, L. Golič, Z. Trontelj, J. Lužnik, Z. Jegličič & J. Pirnat, *Phys. Rev. Lett.* **76** 523 (1996)
- [51] H. Sekine, H. Maeda, M. Kosuge, Y. Tanaka and M. Tokumoto, *Synth. Met.* **55-57** 3068 (1993)
- [52] A. Suzuki, T. Suzuki and Y. Maruyama, *Solid State Commun.* **96** 253 (1995)
- [53] O. Chauvet, G. Oszlányi and L. Forro, *Phys. Rev. Lett.* **72** 2721 (1994)
- [54] S. Saito and S. Oshiyama, *Phys. Rev. Lett.* **66** 2637 (1991)
- [55] D. Arcon, J. Dolinsek, R. Blinc, K. Pokhodnia, A. Omerzu, D. Mihailovic and P. Venturini, *Phys. Rev. B* **53** 14028 (1996)
- [56] K. I. Kugel and D. I. Khomskii, *Sov. Phys. -JETP* **37** 725 (1973)
- [57] D. I. Khomskii and K. I. Kugel, *Solid State Commun.* **13** 763 (1973)
- [58] Y. Ito and J. Akimitsu, *J. Phys. Soc. Jpn* **40** 1333 (1976)
- [59] M. Hidaka, K. Inoue, I. Yamada and P. J. Walker, *Physica* **121B** 343 (1983)
- [60] L. J. de Jongh and A. R. Miedema, *Adv. Phys.* **23** 1 (1974)
- [61] M. Kaneko, G. Kuwabara and A. Misu, *Solid State Commun.* **18** 1085 (1976)
- [62] D. Khoi and P. Veillet, *Phys. Rev. B* **11** 4128 (1975)
- [63] T. Kitazawa *master thesis* (in Japanese)
- [64] M. Terai : *unpublished*
- [65] M. Ishizuka : *private communication*
- [66] T. Sekine, T. Okuno & K. Awaga, *Chem. Phys. Lett.* **249** 201 (1996)

- [67] V. Eyert and K. -H. Hock, *J. Phys.: Condens. Matter* **5** 2987 (1993)
- [68] K. Hirakawa, H. Yoshizawa, J. D. Axe and G. Shirane, *J. Phys. Soc. Jpn.* **52** 4220 (1983)
- [69] I. Yamada, *J. Phys. Soc. Jpn.* **33** 979 (1972)
- [70] S. Sasaki, N. Narita and I. Yamada, *J. Phys. Soc. Jpn.* **64** 2701 (1995)
- [71] E. B. Stechel and D. R. Jennison, *Phys. Rev.* **B38** 4632 (1988)
- [72] A. K. McMahan, R. M. Martin and S. Satpathy, *Phys. Rev.* **B38** 6650 (1988)
- [73] M. S. Hybertsen, M. Schluter and N. E. Christensen, *Phys. Rev.* **B39** 9028 (1989)
- [74] T. Mizokawa and A. Fujimori, *Phys. Rev.* **B54** 5368 (1996)
- [75] S. Feldkemper, W. Weber, J. Schulenburg and J. Richter *Phys. Rev.* **B52** 313 (1995)





Kodak Color Control Patches

Blue Cyan Green Yellow Red Magenta White 3/Color Black

© Kodak, 2007 TM. Kodak

C Y M

© Kodak, 2007 TM. Kodak

Kodak Gray Scale

A 1 2 3 4 5 6 M 8 9 10 11 12 13 14 15 B 17 18 19